

2018

Characterization and Reconstitution of S-Palmitoylated IFITM3 Antiviral Activity

Avital Percher

Follow this and additional works at: https://digitalcommons.rockefeller.edu/student_theses_and_dissertations

 Part of the [Life Sciences Commons](#)



**CHARACTERIZATION AND RECONSTITUTION OF
S-PALMITOYLATED IFITM3 ANTIVIRAL ACTIVITY**

A Thesis Presented to the Faculty of

The Rockefeller University

in Partial Fulfillment of the Requirements for

the degree of Doctor of Philosophy

by

Avital Percher

June 2018

CHARACTERIZATION AND RECONSTITUTION OF S-PALMITOYLATED IFITM3 ANTIVIRAL ACTIVITY

Avital Percher, Ph.D.

The Rockefeller University 2018

To rapidly detect early stage infections the innate immune system maintains an assortment of pathogen recognition mechanisms interspersed throughout both the extracellular and intracellular environments. These sensors recognize key components of viral, bacterial and fungal pathogens, and stimulate an inflammatory response which leads to the expression of an extensive network of host defense proteins. One such canonical network is regulated by type I interferon. This pathway responds to viral infections by upregulating hundreds of interferon stimulated genes (ISG) critical for host immunity.

One of the more pivotal proteins for viral control is interferon-induced transmembrane protein 3 (IFITM3). IFITM3 is a host protein known to play a key role in inhibiting numerous virus infections, including influenza, Dengue, West Nile, HIV and Ebola. It is active in the early stages of infection and interferes with viral fusion and content delivery to the cell cytoplasm. Despite this broad antiviral activity, the exact mechanism of IFITM3 viral fusion interference, and whether it directly interacts with the fusion environment remains unknown.

To better understand the physiological conditions of IFITM3 antiviral activity, we required an improved understanding of the endogenous levels of S-fatty acylation. While earlier work in our lab has shown this post-translational modification to be critical

for IFITM3 activity, it was previously impossible to distinguish between different modified populations. I therefore developed the acyl PEG exchange (APE) assay. Utilizing cysteine selective mass tags, APE detects different levels of fatty acylated cysteines within a protein population, which allows us to probe the lipidated states of endogenous proteins for the first time. Using this assay, I have shown that the majority of endogenous human IFITM3 is dually S-fatty acylated.

To investigate the mechanism of IFITM3 antiviral activity, I generated recombinant, native, synthetically lipidated protein for structural and fusion-based studies. We applied an in vitro viral fusion model that detects the lipid mixing of viral envelopes with liposomes. We demonstrate that viral fusion is mitigated with the inclusion of recombinant IFITM3 liposomes. Furthermore, when IFITM3 is modified with maleimide palmitate to mimic fatty-acylation at cysteine 105, lipid mixing is inhibited more than the unmodified IFITM3.

Overall, our recombinant model of viral fusion provides an in vitro approach to investigate IFITM3 function. The assay provides the first evidence that IFITM3 directly alters the membrane fusion environment, and that cysteine palmitoylation enhances protein function as well. In the future, these studies will be complemented with more accurate in vitro assays to further elucidate its critical mechanism.

ACKNOWLEDGEMENTS

Like any modern achievement, this work has been made possible thanks to a village. I am indebted to several individuals and groups, who throughout the years have been pillars of support to either my spirit or my lab supplies. A heartfelt thank you to:

My thesis advisor Dr. Howard Hang, for years of invaluable input and feedback, and always having an open door.

My thesis committee members, Dr. Sanford Simon and Dr. Charles Rice, for providing an annual reality check and reassurance that I'm on the right track.

The Hang lab for being there to help whenever needed.

The Dean's Office for their support, and handling my frequent and frantic questions.

The National Science Foundation for their backing through the Graduate Research Fellowship Program.

TABLE OF CONTENTS

Chapter 1: Introduction to IFITM3 and S-fatty-acylation	1
Chapter 2: Mass-tag labeling reveals site-specific and endogenous levels of protein S-fatty-acylation	13
Chapter 3: Characterization of endogenous IFITM3 S-fatty-acylation.	31
Chapter 4: Generation of recombinant IFITM3 and lipidated isoforms.	38
Chapter 5: Production and anti-viral activity of IFITM3 proteoliposomes.	50
Chapter 6: Future Directions.	74
Discussion	82
References	86

LIST OF FIGURES

Figure 1	Type I interferon activation pathway	2
Figure 2	IFITM family evolution and IFITM1-3 sequence alignment	3
Figure 3	Membrane Topology of IFITM3	4
Figure 4	Possible mechanisms of IFITM3 inhibition.	7
Figure 5	Proposed mechanism for IFITM3 disruption of cholesterol homeostasis.	8
Figure 6	Proposed mechanism for IFITM3 arrest of viral hemifusion.	10
Figure 7	Posttranslational modifications of IFITM3.	12
Figure 8	Protein lipidation varies in chain length, saturation and site of attachment.	14
Figure 9	Schematic for S-fatty acylation detection and analysis	16
Figure 10	APE enables the detection of S-fatty acylation levels.	18
Figure 11	Optimization of APE.	20
Figure 12	APE and metabolic labeling of HA-HRas.	21
Figure 13	APE can be applied to proteins with varied topologies, molecular weights, and S-fatty acylation events.	22
Figure 14	mPEG-Mal concentration optimization of IFITM3.	32
Figure 15	Murine IFITM3 APE PEGylation levels and antiviral activity.	33
Figure 16	APE of endogenous murine IFITM3.	34
Figure 17	APE and antiviral activity of human IFITM3.	37
Figure 18	Purification of recombinant IFITM3	39
Figure 19	Mimicking S-fatty acylation of rIFITM3 with maleimide-palmitate.	41

Figure 20	Mal-palm labeling of rIFITM3 S-fatty acylation isoforms.	42
Figure 21	Mal-palm labeling optimization and mass-spec confirmation.	44
Figure 22	Rapid dilution of detergent solubilized lipid-protein leads to formation of unilamellar proteoliposomes.	52
Figure 23	Protein incorporation into the proteoliposome.	54
Figure 24	Calculation of IFITM3 concentration per LUV and lipid bilayer leaflet.	55
Figure 25	VDID labeled IAV enables detection of envelope lipid mixing.	56
Figure 26	Fusion comparison of LUV lipid compositions.	58
Figure 27	Temperature of IAV fusion affects rate, and signal saturation	60
Figure 28	Viral fusion with LUV is pH, HA dependent.	61
Figure 29	Titration of VAMP2 and apoIFITM3 confirms dynamic range of proteoliposome fusion assay.	63
Figure 30	ApoIFITM3 inhibits viral lipid mixing to a greater degree than VAMP2.	64
Figure 31	All constructs of IFITM3 inhibit viral lipid mixing.	65
Figure 32	Cys specific lipidation of IFITM3 alters inhibition of DiD dequenching.	66
Figure 33	Residual mal-palm, chymotrypsin treatment does not alter proteoliposome fusion properties.	68
Figure 34	Labeling of IAV with BCN-NHS-Ester enables fluorescent detection of IAV capsid proteins by SDS-PAGE	77
Figure 35	Lipid composition of late endosome, and proposed model composition.	79
Figure 36	Single particle measurements for improved characterization of viral fusion.	81
Figure 37	IFITMs' interference with viral fusion and entry is a unique antiviral mechanism.	82

LIST OF TABLES

Table 1	Antiviral activity of IFITM family	5
Table 2	Sizes and formation techniques for unilamellar liposomes.	50

Chapter 1: Introduction

IFN-Induced Innate Immunity

The interplay and kinetics of pathogenic infections necessitates persistent, basal level cell surveillance and rapid early response capabilities. The broadly conserved first line of defense, the innate immune system, is a non-adaptive response triggered by commonly conserved, pan-pathogen motifs (pathogen-associated molecular patterns, PAMP). These bind to pathogen recognition receptors (PRRs) to activate the secretion of inflammatory cytokines¹, which in turn upregulate a broad range of defense proteins in immune and non-immune cells alike that disrupt pathogenicity and infection. The innate inflammatory response is critical for orchestrating changes in gene expression² that provide a crucial line of defense for early stage infection, and facilitates the development of the adaptive immune response as well³. Despite adaptive immunity being critical for late stage infection and clearance intracellular defense mechanisms contain no adaptive capabilities, rendering the innate response the key means of disrupting intracellular pathogen infection.

One of the canonical inflammatory pathways is that of the interferon (IFN) cytokines, which play a critical role in innate defense⁴. Mediated through the JAK/STAT pathway (Fig.1), activation results in the upregulation of hundreds of interferon-stimulated genes (ISG) that alter the cellular and tissue environment as well as detect and combat viral replication, entry, and cell-to-cell dissemination⁵. IFNs are classified into three different types – type I IFN (IFN α and IFN β)⁴ type II (IFN γ)⁶, and type III (IFN λ)⁷. While type I activation is considered the primary pathway for ISG activation, increasing evidence is emerging for type III activation in a tissue-specific manner⁷,

suggesting a more tightly regulated and temporally controlled expression of ISG antiviral activity.

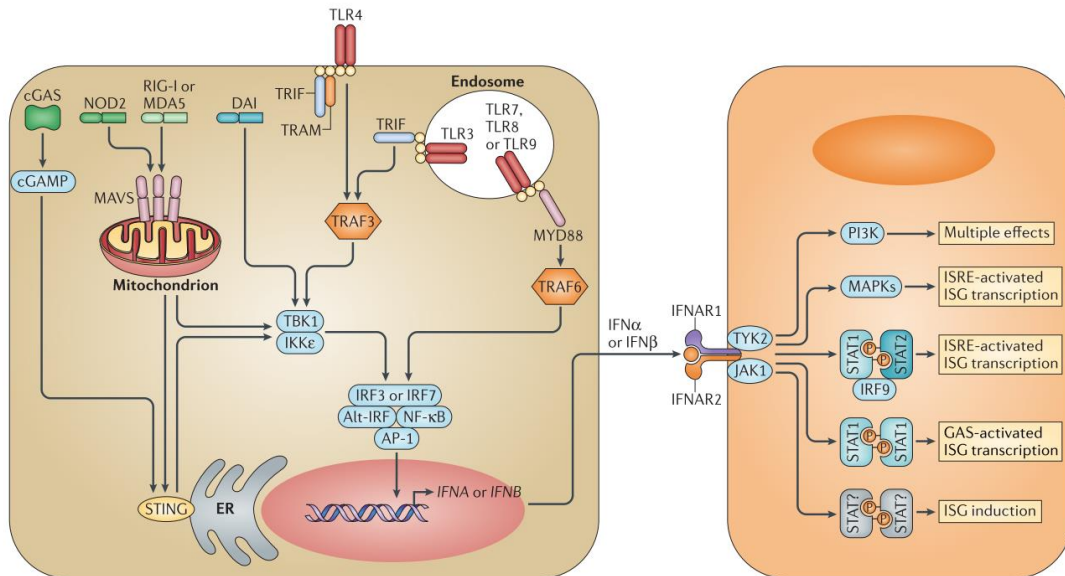


Figure 1. Type I interferon activation pathway. From McNab et al. Nat Rev Immunol. (2015)⁴. IFN expression is activated with the detection of PAMPs by a variety of PRRs located in the cytoplasm, at the plasma membrane, and the endosomal lumen. Binding of secreted IFN with receptors results in the upregulation of hundreds of different ISGs, priming nearby cells to express antiviral proteins.

Interferon-Induced Transmembrane Protein 3:

Within the broad group of interferon-stimulated genes (ISG), members of the interferon-induced transmembrane protein (IFITM) family have emerged as potent restrictors of viral infection. Detected as an antiviral protein from a siRNA genomic screen searching for host factors critical for influenza A virus (IAV) infection⁸, IFITM3 is an essential host factor for viral innate defense, restricting a panoply of viruses⁹ entering through the endosomal pathway, in particular IAV¹⁰. As the IFITM family is the first ISG known to interfere with viral infection during fusion and content entry, considerable interest has emerged in understanding their characterization and mechanism.

IFITM orthologues are widely conserved among vertebrates¹¹, with the human IFITM family having emerged during primate evolution¹². Human IFITMs include IFITM 1, 2, 3, 5, and 10, though only IFITM1, 2, and 3 exhibit antiviral activity. IFITM10 has a yet unknown function. IFITM3 predates the divergence of IFITM1, and IFITM2, which is only found in gorillas, chimpanzees, and humans. Sequencing alignment of IFITM1, 2, 3 shows similar size and domain conservation, except for IFITM1 which has lost its N-terminal domain (Fig. 2). Both our lab and others^{13,14} have shown IFITM2 and 3 to contain an N-terminal YEML sorting motif that results in IFITM2 and 3 trafficking via the plasma membrane into the endosomal pathway. IFITM1, which has lost this motif in its N-terminus, is thought to localize to the plasma membrane.

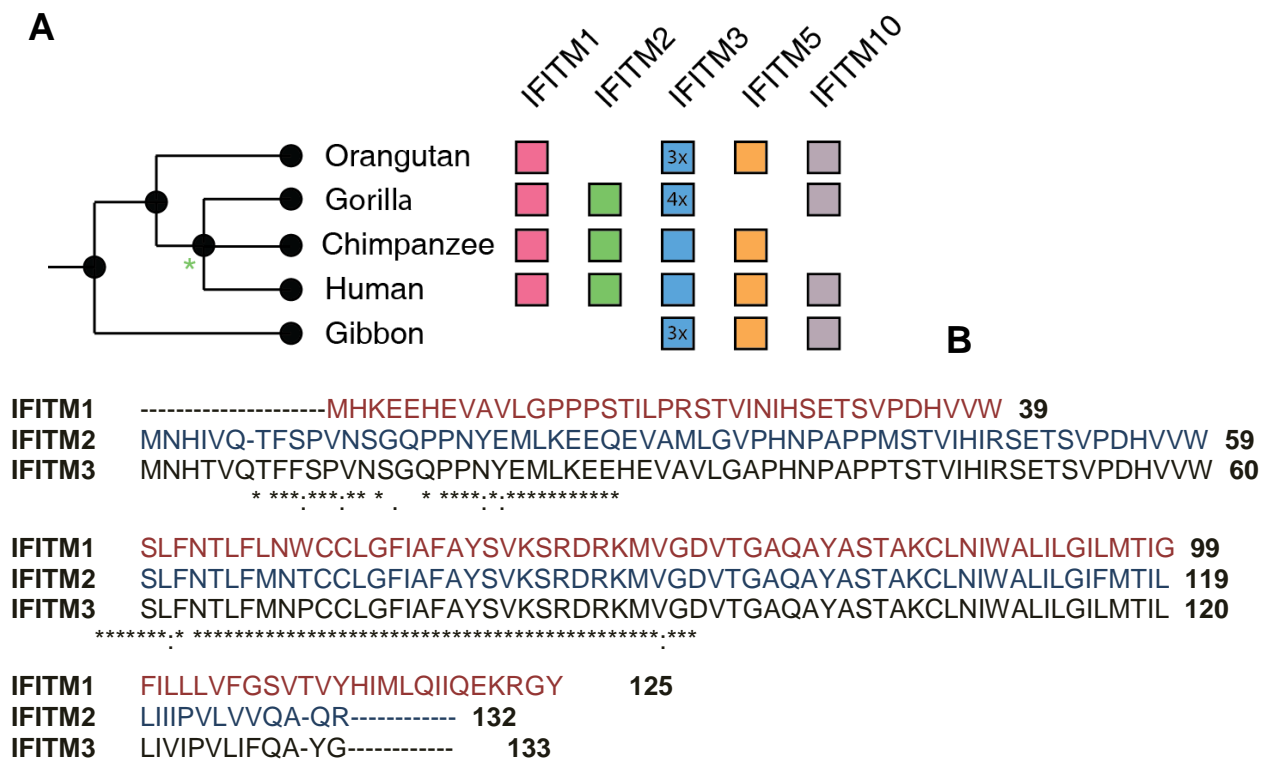


Figure 2. IFITM family evolution and IFITM1-3 sequence alignment. (A) Modified gain/loss phylogenetic tree from Compton et al. EMBO reports (2016)¹². Asterisk marks evolutionary appearance of IFITM2. (B) Sequence alignment of human IFITM1, 2 and 3. Aligned using Clustal Omega.

IFITM3 membrane topology is a critical factor in exploring possible interactions and mechanisms of interference. Earlier work in our lab using cytoplasmic lipidation motif reporters¹⁵, and work by others showing the association of IFITM3 with μ 2 AP-2 proteins¹⁴ and flow cytometry-based surface labeling¹⁶ provide strong evidence that the N-terminal domain is cytoplasmic facing. In contrast, conflicting reports of the C-terminal topology leave it unclear whether it contains a transmembrane, or amphipathic domain^{13,16}. Recent EPR and NMR data of recombinant protein indicates IFITM3 contains one transmembrane domain (therefore a type II membrane protein)¹⁷, though this data was obtained with DPC micelles (not a lipid bilayer), and with protein that was denatured during purification(Fig. 3). While promising, additional studies will be necessary to confirm the exact topology in the appropriate environment.

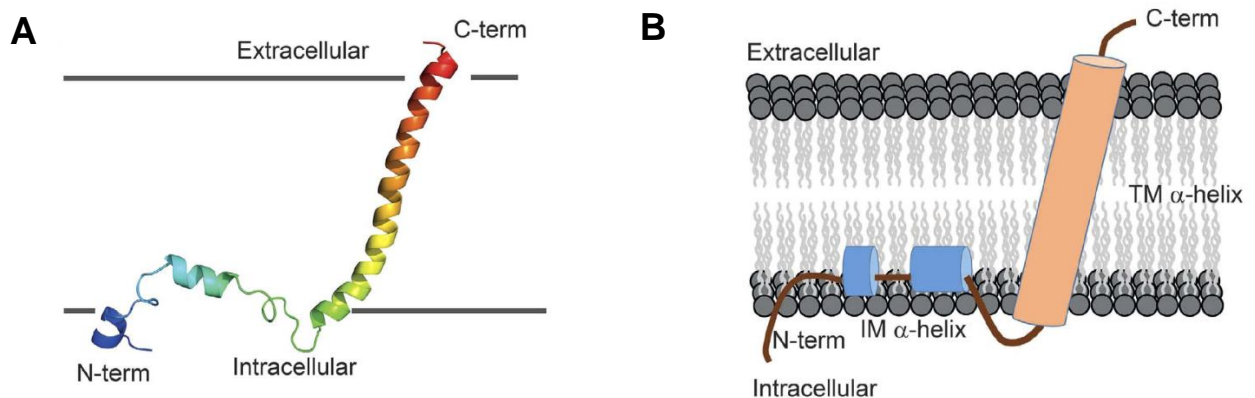


Figure 3. Membrane topology of IFITM3. (A) NMR/EPR predicted topology and (B) respective model of IFITM3, proposed by Ling et al. *Science Reports*, 2016¹⁷.

Broad antiviral activity makes IFITM3 a critical first line of innate immune defense.

Since the first reports on IFITM3 antiviral activity against IAV and Dengue⁸, a considerable body of work has emerged elucidating the range of viruses susceptible to inhibition. This research has shown IFITM3 to be active against most clinically relevant viral pathogens (Table 1). It has also established the importance of IFITM3 in different tissues such as the lung¹⁸, liver¹⁹ and spleen²⁰, and diverse cell types, including epithelial cells¹⁸, fibroblasts²¹, dendritic cells²², and CD8⁺ T cells²³.

Table 1. Antiviral activity of IFITM family. Updated table from Smith et al. ⁹: ‘X’, viral entry fusion independent. ϕ , viral entry requires lysosomal cathepsins for priming and entry.

Family	Virus	Fusion pH Conditions	Restricted by IFITMs	Active IFITM	Reference
<i>Orthomyxoviridae</i>	Influenza A virus	< pH 6	✓	2,3	8, 28,61
	Influenza B virus	<pH 6	✓	1-3	74
<i>Flaviviridae</i>	West Nile virus	pH >6	✓	1-3	8, 21
	Zika Virus	<pH 6	✓	3	24
	Dengue virus	<pH 6	✓	1-3	8
	Hepatitis C virus	pH >6	✓	1-3	8, 19,25
<i>Rhabdoviridae</i>	Vesicular stomatitis virus	pH >6	✓	1–3	26,27
	Rabies virus	<pH 6	✓	2–3	24
	Lagos bat virus	<pH 6	✓	2–3	24
<i>Filoviridae</i>	Marburg virus	ϕ	✓	1–3	28
	Ebola virus	ϕ	✓	1–3	29

Family	Virus	Fusion pH Conditions	Restricted by IFITMs	Active IFITM	Reference
<i>Herpesviridae</i>	Cytomegalovirus	Cell type specific	Cytokine Driven	3	20
<i>Coronaviridae</i>	Coronavirus	φ	✓	1–3	29
<i>Retroviridae</i>	Human immunodeficiency virus	Varies	Pathway dependent	1-3	30-33
	Jaagsiekte sheep retrovirus	pH >6	✓	1 best	34
	Moloney leukemia virus	X	X	No	8, 29
<i>Arenaviridae</i>	Lassa virus	pH >6	X	No	8
	Machupo virus	pH >6	X	No	8
	Lymphocytic choriomeningitis virus	pH >6	X	No	8
<i>Togaviridae</i>	Semliki forest virus	pH >6	✓	1 and 3	34
	Chikungunya	<pH 6	✓	3	35
<i>Bunyaviridae</i>	La Crosse virus	<pH 6	✓	1-3	36
	Hantaan virus	<pH 6	✓	1-3	37
	Andes virus	<pH 6	✓	1-3	37
	Rift Valley fever virus	<pH 6	✓	2 and 3	37
	Crimean–Congo haemorrhagic fever virus	<pH 6	X	No	37
<i>Reoviridae</i>	Reovirus	<pH 6	✓	3	37

Proposed mechanisms of IFITM3 anti-viral activity.

IFITM3 restriction of viral infection occurs at the stage of viral fusion and content delivery³⁸, focusing proposed models for IFITM3's mechanism of antiviral activity on alternations to the environment in which viral fusion often occurs—the late endosome. An unbiased conjecture of possible mechanisms include (1) an indirect mechanism whereby IFITM3 recruits a yet unknown protein/cofactor responsible for the alternation of the fusion environment, either by changing membrane properties, or by altering the maturation pathway of the endosomal vesicle. (2) A direct mechanism, in which IFITM3 alters the endosomal membrane's biophysical properties such as membrane fluidity or curvature capacity, or (3) the maturation of the endosomal vesicle, directing the viral particle to an incompatible environment. (4) IFITM3 directly interacts with the viral particle, interfering with the completion of fusion (Fig. 4).

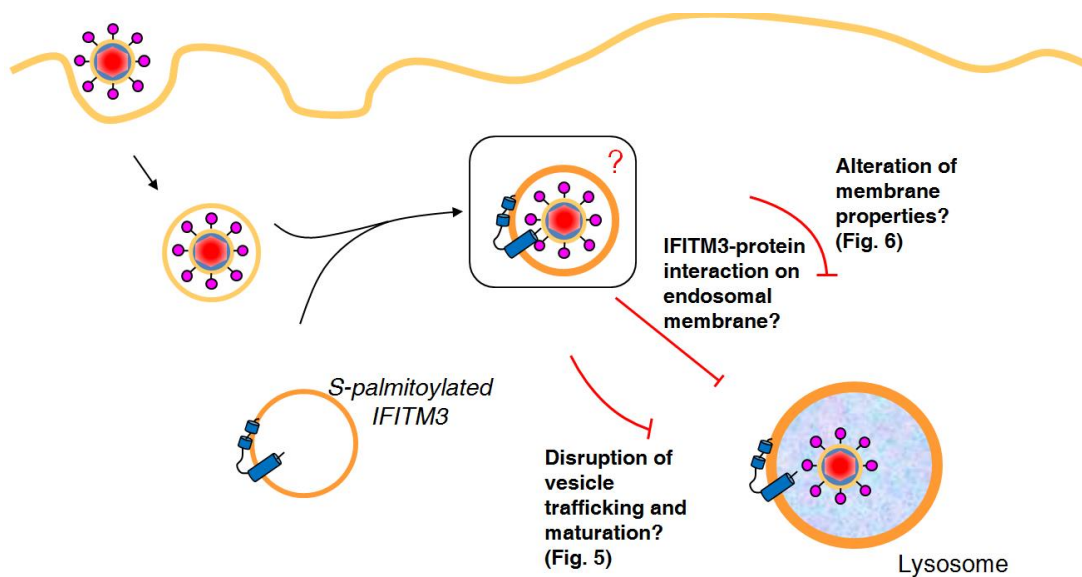


Figure 4. Possible mechanisms of IFITM3 inhibition. IFITM3 inhibits viral fusion and content delivery via a yet unknown mechanism. This interaction either acts indirectly, recruiting an unknown protein/cofactor, or directly by disrupting the membrane fusion environment.

There are currently two models for IFITM3's antiviral restriction, each suggesting distinctly different mechanisms: In 2013, Amini-Bavil-Olyaei *et al.* proposed that IFITM3 interferes with viral entry by disrupting cholesterol export from the late endosome³⁹. They showed that IFITM3 co-immunoprecipitates with vesicle associated membrane protein-A (VAP-A), that is part of the cholesterol export pathway mediated by NPC-2/1 and ORP family proteins⁴⁰. As the antiviral activity of IFITM3 is impaired with the overexpression of VAP-A, they posit that IFITM3 inhibits VAP-A, and that this interaction is overridden by sufficiently saturating the system with VAP-A protein. As they additionally show an increase in late endosome cholesterol in cells overexpressing IFITM3, they propose that the interaction between IFITM3 and VAP-A interferes with ORP-mediated cholesterol export, resulting in greater rigidity of the membrane, thus impeding fusion and retaining the viral particle until it is degraded in the lysosome (Fig. 5).

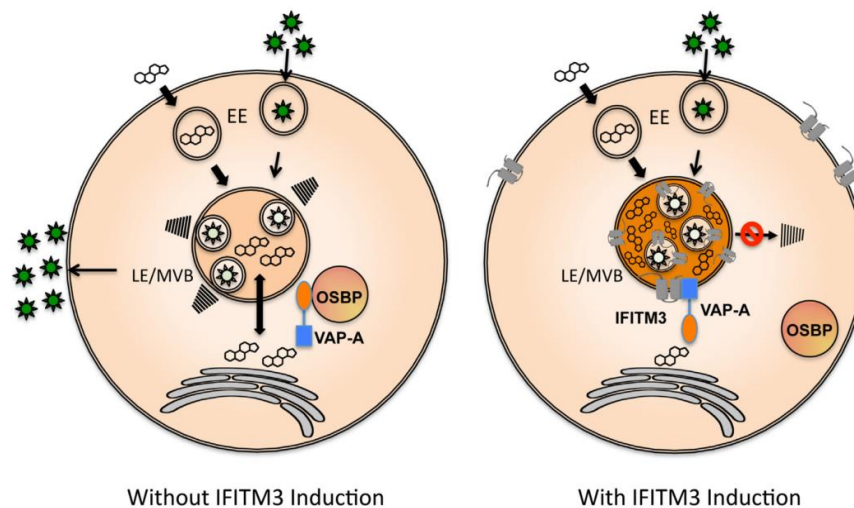


Figure 5. Proposed mechanism for IFITM3 disruption of cholesterol homeostasis. Fig. 7 from Amini-Bavil-Olyaei *et al.*³⁹. *Left:* under basal level conditions, cholesterol is trafficked out of the late endosome through NPC1/2 to ORPs and ER-bound VAP-A. *Right:* IFITM3 was proposed to interact with VAP-A, disrupting its interaction with ORP and increasing cholesterol levels and membrane rigidity within the late endosome.

In contrast, in 2014, Desai et al.²⁷ proposed that as an alternative to cholesterol homeostasis, IFITM3 interferes with fusion pore formation, arresting late stage virus entry at the point of hemifusion (in which the outer membrane leaflet of the viral envelope mixes with the endosomal membrane, but the inner leaflet remains intact)(Fig. 6). Using a panel of membrane-binding fluorophores, and fluorescent nucleocapsid proteins, they demonstrated that with the overexpression of IFITM3, similar or heightened levels of envelope-lipid mixing occurs, reflecting either hemifusion, or complete fusion. Combined with a significant IFITM3-driven decrease in viral content delivery, these two data sets indicate that the viral particles initiate membrane fusion, but are obstructed from completing the fusion process, retaining the hemi-fused virus within the endosome and targeting it for degradation. Critically, they additionally show that this mechanism is independent of cholesterol levels, and that induced accumulation of cholesterol does not alter fusion and binding properties in A549 lung epithelial cells.

While this model presents an alternative IFITM3 function, they were unable to confirm a precise molecular mechanism. This renews the question of direct vs. indirect interactions, though additional publications have shown IFITM3 interfered with cell-cell fusion in two separate models^{26,34}. Considering the extensive differences between the plasma and endosomal membrane both in lipid and protein composition, these experiments reinforce the hypothesis that the mechanism is through a direct interaction of IFITM3 with the membrane that alters the lipid properties in some manner so as to inhibit fusion.

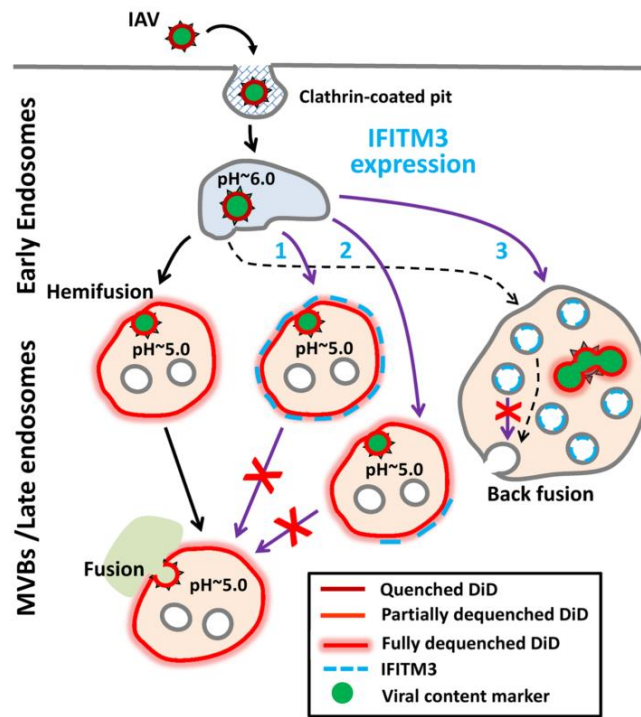


Figure 6. Proposed mechanism for IFITM3 arrest of viral hemifusion. Figure 8 from Desai et al.²⁷. Instead of altering cholesterol homeostasis, IFITM3 was proposed to arrest viral hemifusion. As the paper was unsuccessful in detecting colocalization between the viral particles and IFITM3, it is still unclear whether it is a direct interaction.

Though IFITM3's inhibition of viral fusion and entry has been a primary research focus, additional IFITM3 functionalities have been reported, suggesting a more complex role in host defense: Though a host protein, IFITM proteins can be incorporated into budding viral particles^{32,41}, thus impairing their assembly and infectivity. IFITM3 also plays a role in supporting adaptive immunity and regulating inflammation–memory CD8⁺ T cells in the lung parenchyma express higher levels of IFITM3, increasing their resistance to secondary infections²³. Respiratory DC cells from IFITM3 KO mice showed increased susceptibility to influenza infection, leading to impaired trafficking to lymph nodes, and CD8⁺ activation²². Additionally, IFITM3 was shown to be critical for regulating IL-6 expression and lymphocyte survival in CMV infection²⁰, as well as down regulating IRF3-mediated IFN- β expression during viral infection⁴².

Posttranslational modifications regulate IFITM3 traffic and activity

IFITM3 is regulated by several post-translational modifications (PTMs) that alternately affect its antiviral activity (Fig. 7). Using metabolic labeling with the biorthogonal chemical reporter alkyne-palmitate (alk-16), our lab has shown that all three cysteines (Cys) in IFITM3 are S-fatty-acylated, and that mutagenesis of these residues to alanines (Ala) critically impairs its antiviral activity¹³. The trafficking of IFITM3 is also regulated by the phosphorylation of tyrosine 20, which leads to diffuse localization (in contrast to a punctuate morphology) and loss of antiviral activity^{43,44}. IFITM3 is further modified by the ubiquitination of lysines 24, 83, 88 and 104¹³, and the methylation of lysine 88⁴⁵, both of which have been shown to disrupt antiviral activity. The disruption of ubiquitination by mutation of the individual lysines reduced IFITM3 protein turnover and increased its anti-viral activity. Since our laboratory discovered IFITM3 S-fatty-acylation¹⁵, we have been especially interested in understanding how this dynamic modification quantitatively controls IFITM3 antiviral activity.

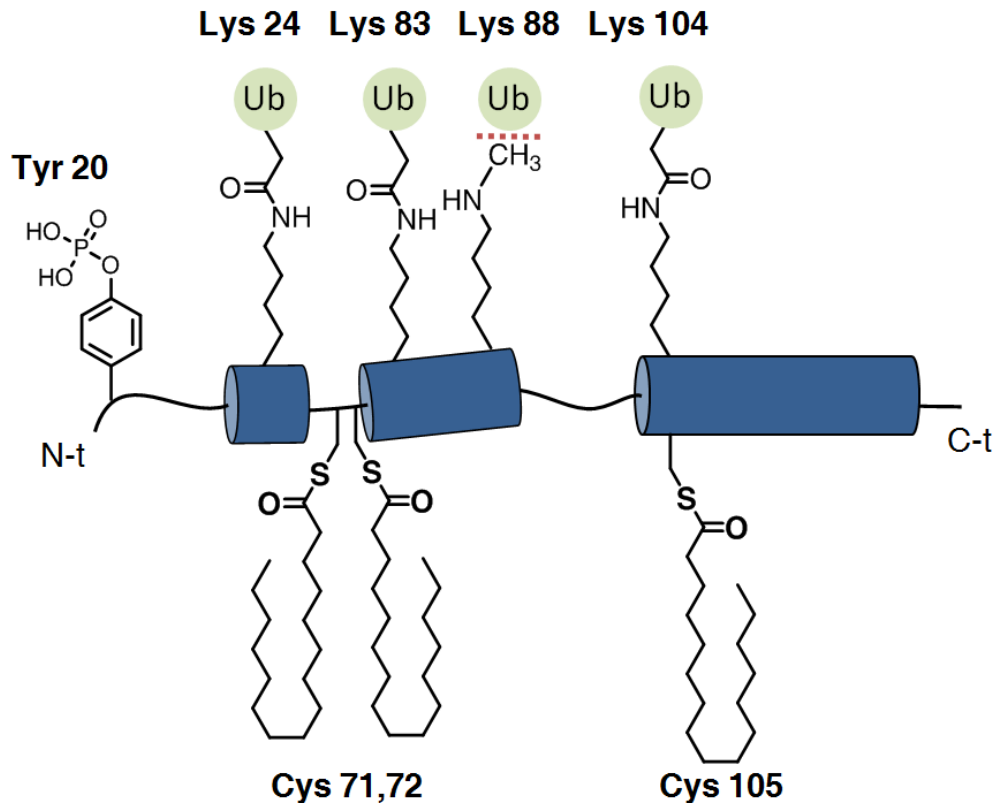


Figure 7. Posttranslational modifications of IFITM3. Schematic of IFITM3 PTMs: while Tyr20 phosphorylation, methylation at Lys 88 and ubiquitination (Ub) at Lys 24,83,88,104 interfere with IFITM3, Cys palmitoylation is essential for its antiviral activity.

Our understanding of IFITM3 physiology and scope of antiviral activity has been increasing over the past years. Nevertheless, these efforts have yielded mixed results in elucidating the molecular mechanism of IFITM3 activity, prompting the exploration of alternative experimental models. The following chapters describe our efforts towards characterizing the endogenous state of S-fatty-acylated IFITM3, generating recombinant protein, and its application to reconstituted liposomes for *in vitro* virus fusion assays.

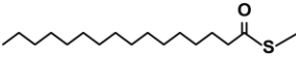
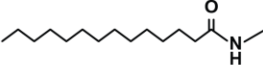
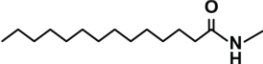
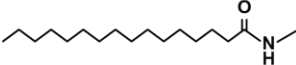
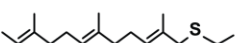

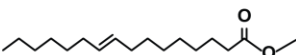
Chapter 2: Mass-tag labeling reveals site-specific and endogenous levels of protein S-fatty acylation

S-fatty acylation: a dynamic post-translational modification.

The covalent coupling of fatty acids and similar carbon chain homologues to proteins provides the cell with a spatiotemporal mechanism for controlling protein affinity for membranes. These modifications affect stability, function, trafficking, and membrane composition preferences⁴⁶. In eukaryotic cells, long chain fatty acid modifications primarily occur with lipids 12-18 carbons long, varying in saturation and attachment loci⁴⁷ (Fig 8A).

S-fatty acylation, which couples fatty acids to cysteines through a thioester bond, is primarily in the form of a saturated 16-carbon chain⁴⁸ and is the most common eukaryotic post lipid modification to be dynamically modified⁴⁷. S-fatty acids are coupled to proteins through protein acyl transferases (PATs), containing a DHHC catalytic domain⁴⁹. In humans, there are 23 different DHHC family proteins, though substrate redundancy has complicated our understanding of targets. The cleavage of S-fatty acids is mediated by acyl-protein thioesterase (APT)1/2⁵⁰, PPT1⁵¹ and ABHD17⁵² (Fig. 8B), though considering the broad profile of S-acylated proteins, more are likely to be discovered. As the immune system must self-regulate inflammation to avoid an excessive response and immunopathology^{53,54}, the dynamic nature of S-fatty acylation has prompted interest in understanding what role it potentially plays in innate and adaptive immunity.

A

	<u>Amino Acid</u>	<u>Lipid Species</u>	<u>Linkage</u>	<u>Lipid</u>	<u>Enzyme transferase / lipase</u>
Reversible	Cys	Palmitate	Thioester		zDHHC / APT, PPT, ABHD17
	Lys	Myristate	Amide		NMT / SIRT
Stable	H ₂ N-Gly	Myristate	Amide		NMT
	H ₂ N-Cys	Palmitate	Amide		Hhat
	Cys	Farnesyl	Thioether		FTase
	Cys	Geranylgeranyl	Thioether		GGTaseI, II
	Ser	Palmitoleate	Thioether		Thioether

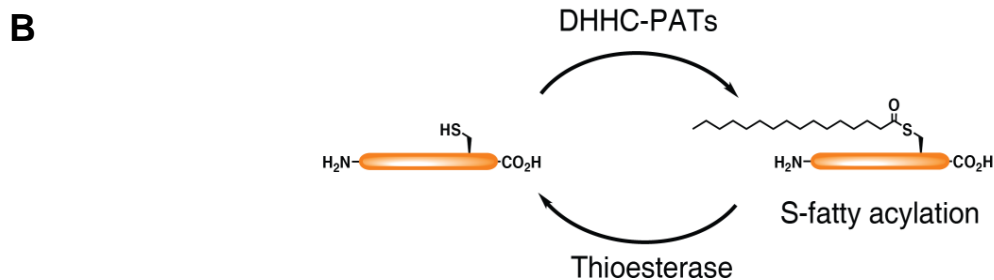


Figure 8. Protein lipidation varies in chain length, saturation and site of attachment. (A) Comparison of lipidation modifications varying in structure and site of attachment. Table from Chamberlain et al.⁴⁷, modified to include lysine deacylation by SIRT2⁵⁵. (B) S-palmitoylation is dynamically regulated, with the addition and cleavage of the fatty acid regulated by DHHC-PATs and thioesterases, respectively.

Our expanding knowledge of the role of S-fatty acylation in influencing numerous cellular activities has driven the field's continued investment in improved methods for S-fatty acylation detection, and understanding of dynamics and regulation⁵⁶. Proteome wide profiling has made considerable strides with the development of a variety of

enrichment techniques that can target either endogenous proteins, or proteins labeled by exogenous tags incorporated through the cellular machinery (metabolic labeling)⁵⁷. These tags – alkyne-modified fatty acid chemical reporters (Fig. 9A) – utilize bioorthogonal Cu(I)-catalyzed azide-alkyne cycloaddition (CuAAC)⁵⁸ to label proteins for analysis by polyacrylamide gel electrophoresis (PAGE), or enrich for characterization by mass spectrometry. This approach has been developed⁵⁷ and used by our lab^{15,59} to generate whole cell profiles that provide a first step towards discovering new modifications.

As an alternative to metabolic labeling, thioester specific cleavage of hydroxylamine (NH₂OH) has enabled the enrichment of endogenously labeled S-fatty acylated proteins by acyl-biotin exchange (ABE)⁶⁰, and the acyl-resin capture (acyl-RAC)⁶¹. These methods overcome technical limitations inherent with metabolic labeling, and can detect S-fatty acylated proteins under physiological conditions, including ex-vivo tissue samples inaccessible to chemical probes⁶². They have yielded invaluable profiles of endogenous lipo-proteomes, characterizing both cell types⁶³⁻⁶⁶ and tissues⁶⁷⁻⁶⁹. Recent advances in experimental design have also enabled Cys specific detection of site modification, streamlining initial detection and site validation into a single data set⁷⁰.

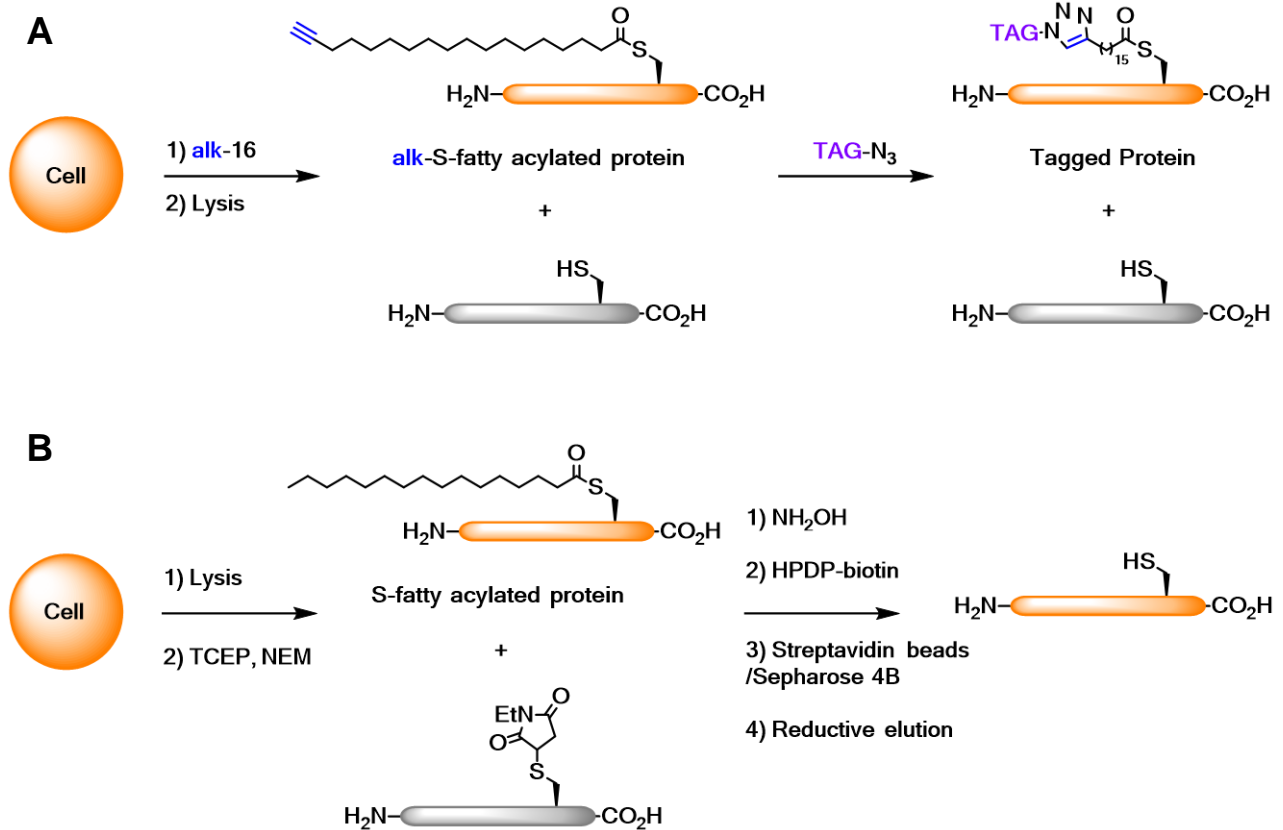


Figure 9. Schematic for S-fatty acylation detection and analysis. (A) For metabolic labeling, cells are incubated with alkyne-labeled palmitate (alk-16) for several hours prior to harvesting. Proteins are lysed, reacted with azide-functionalized reagents by CuAAC, and analyzed by in-gel fluorescence, or processed for proteomics⁵⁷. (B) With ABE or acyl-RAC, cell lysates are capped with NEM, and the thioesters cleaved with NH₂OH. The newly generated cysteines are reacted with HPDP-Biotin⁷¹. Following streptavidin bead enrichment, captured proteins are eluted with reducing agents and then analyzed by Western blot or processed for proteomics⁵⁹.

Albeit these advances and methodological iterations, several limitations have persisted in quantitatively characterizing S-fatty acylation with these assays; S-acylation levels (the number of fatty acids on a single protein) cannot be differentiated, nor could the ratio between S-fatty acylated, and non S-fatty acylated protein (apo) be detected within the same sample. Furthermore, metabolic labeling of a sample requires the

addition of exogenous source of chemical reporters, veering further away from physiological conditions. We therefore sought to develop a new method capable of detecting the different S-fatty acylation levels present in a protein population. This would advance the fields ability to understand how changes in S-fatty acylation levels alter downstream phenotypes such as localization and function.

To resolve a protein's levels of S-fatty acylation, we have developed acyl-PEG exchange (APE)⁷¹. This method utilizes the selective cleavage of thioesters by NH_2OH to cleave S-fatty acids, exposing nucleophilic thiols which are then labeled with tags of defined molecular weight. These coupled 'mass tags' of maleimide-functionalized polyethylene glycol (mPEG-Mal) result in a mobility shift when analyzed by gel electrophoresis, corresponding to the original number of S-fatty acylated cysteines. APE enables facile detection of multiple S-fatty acylation populations of proteins, without the drawback of affinity enrichment, or the interference of exogenous chemical reporters (Fig. 10A).

For APE, cell samples are lysed in denaturing buffer (4% SDS), and the free cysteines reduced with TCEP and capped with N-ethyl maleimide (NEM). After excess NEM is removed by protein precipitation, thioesters are cleaved by incubating the resuspended sample with NH_2OH . Excess NH_2OH is removed, and the exposed cysteines are labeled with mPEG-Mal, before analysis by SDS-PAGE and western blot. We first applied APE to the canonical S-palmitoylated protein HRas (Fig. 10B). A peripheral membrane GTPase involved in cell division, HRas contains two S-palmitoylation sites (Cys 181, 184), as well as one thioether coupled (and therefore NH_2OH insensitive) farnesyl group at Cys 186⁷². To compare our overexpressed HA-

tagged HRas with endogenous level proteins, we also blotted against endogenous calnexin, an ER chaperon protein with two known S-palmitoylation sites⁷³.

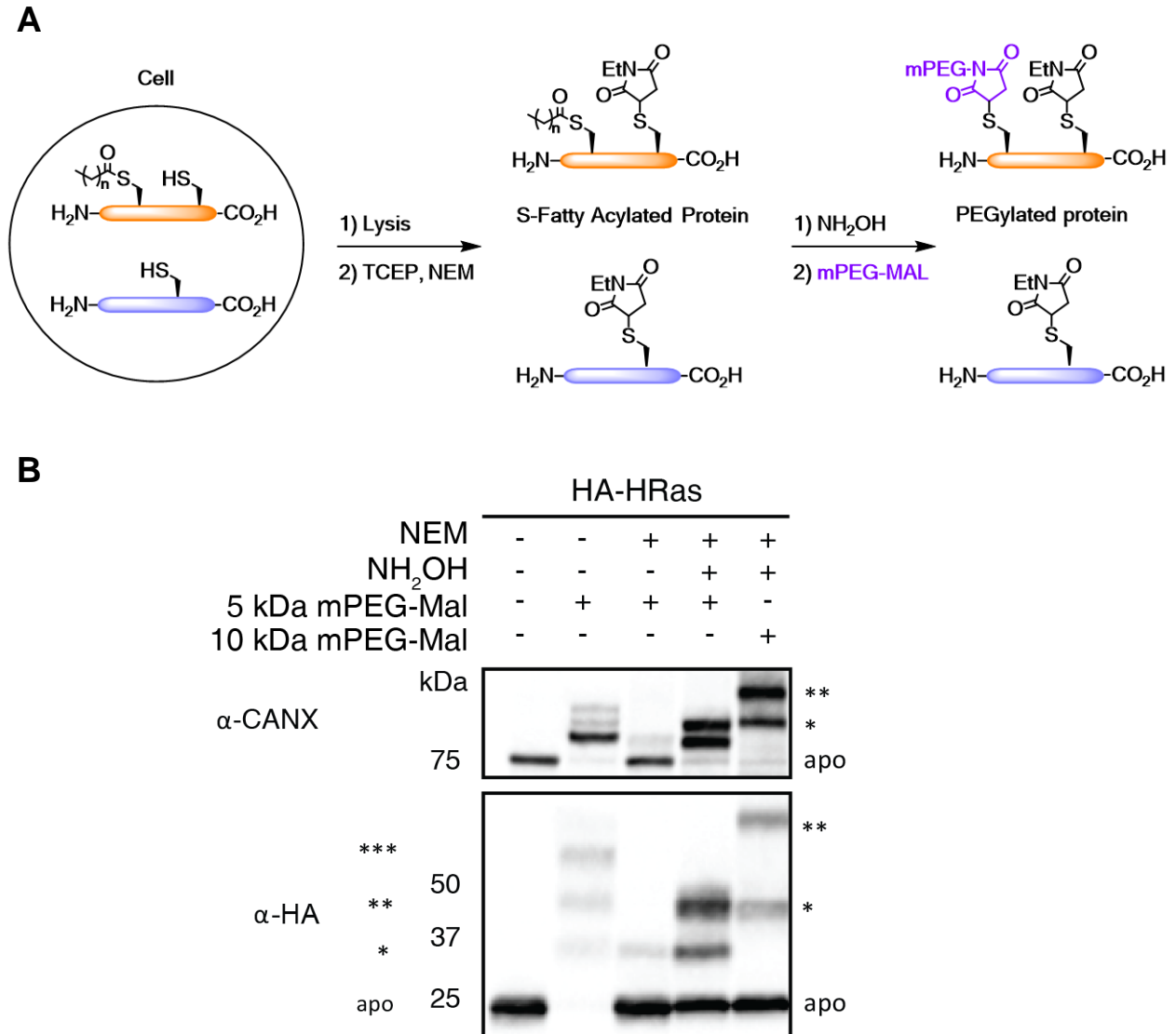


Figure 10. APE enables the detection of S-fatty acylation levels. (A) Schematic for APE protocol. Samples are lysed, reduced and capped with NEM. The thioesters are then cleaved with NH₂OH, labeled mPEG-mal, and analyzed by SDS-PAGE and Western blot. (B) HA-HRas was analyzed by APE with different controls. With the sequential addition of NEM, NH₂OH, and mPEG-mal, mass shifts reflecting different levels of S-fatty acylation are observed.

The incubation of HEK293T cell lysates with mPEG-Mal alone (lane 2) results in several mass shifts, corresponding with the varying availability of non-modified cysteines. With the addition of NEM prior to mass-tag labeling (lane 3), all cysteines are fully capped, resulting in no mass-shift. The addition of the NH_2OH (lane 4) exposes previously S-fatty acylated cysteines, which are successfully labeled with mPEG-mal. HRas displays two mass shifts, reflecting single (*) and doubly (**) labeled populations, corresponding with its dynamic spatial regulation through S-fatty acylation⁷². Additional shifts were not observed, suggesting successful NH_2OH resistance of non-thioester based modifications. Calnexin (CANX) exhibits two mass shifts as well, in agreement with the literature on the known S-fatty acylation sites. To show that our mass shifts are dependent on the size of our mass-tags, samples were additionally labeled 10 kDa mPEG-mal (lane 5). Indeed, the larger molecular weight mass tag exhibited a mass shift twice the size of the 5 kDa tag, confirming a tag-dependent shift.

Having demonstrated a proof-of-concept - that APE can label S-fatty acylated proteins, the protocol was optimized to ensure complete capping, cleavage and labeling. A titration of the amount of NH_2OH during a one hour incubation showed saturating levels were obtained at 0.75 M (Fig. 11A). Saturating levels for mPEG-mal varied depending on the molecular weight of the protein analyzed (Fig. 11B), though we discovered that some proteins, such as Rab7 present a mPEG-mal dependent mass shift even without NH_2OH . The presence of 0.1 % Triton X-100 (copied from the ABE protocol) did not end up affecting our results with our specific proteins (Fig. 11C) though a critical experimental component was shown to be the inclusion of EDTA during the cleavage of NH_2OH (Fig. 11D).

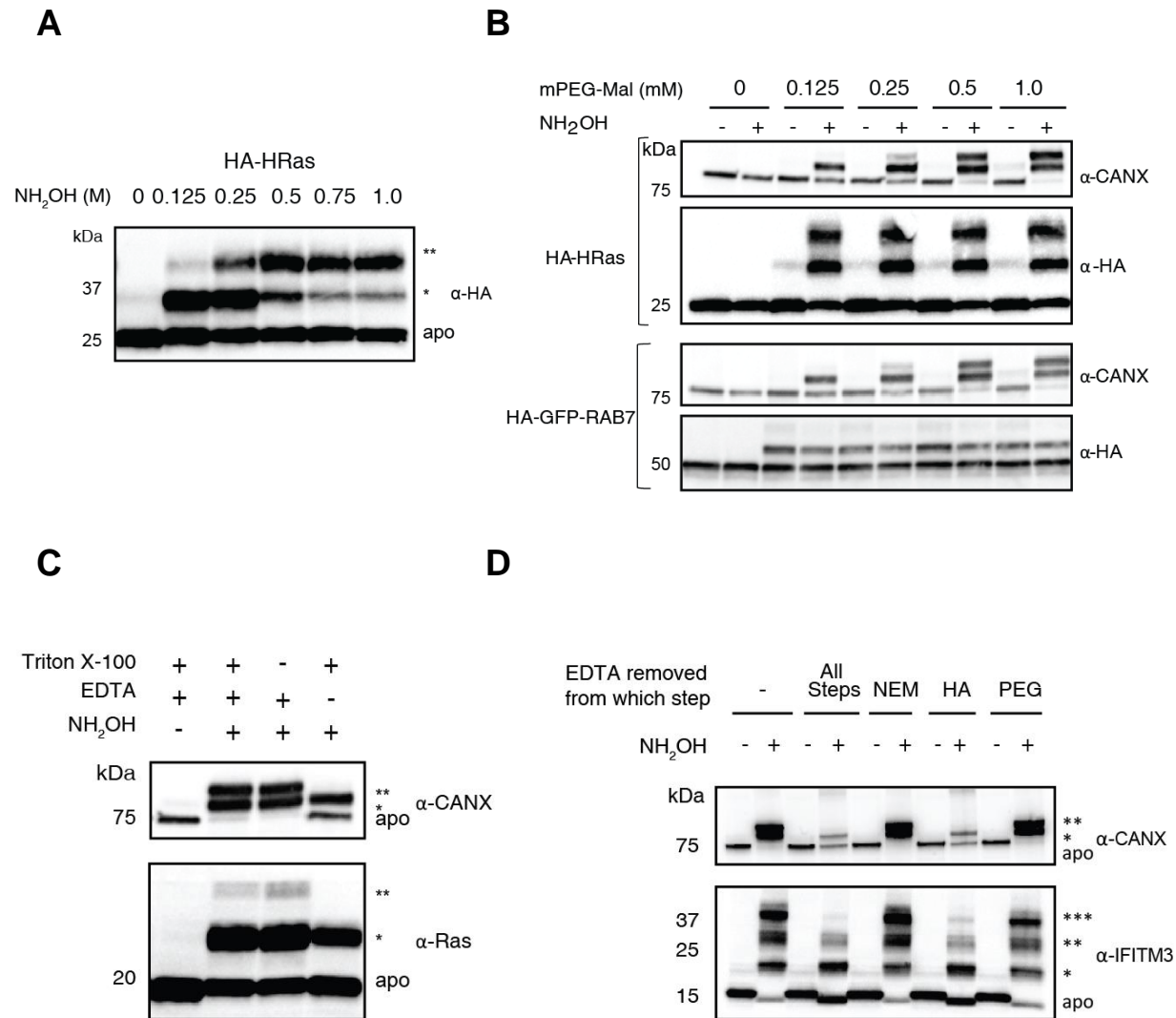


Figure 11. Optimization of APE. (A) APE does not require 0.2% Tx-100, though removal of EDTA impairs the completion of di-PEGylation for CANX and endogenous Ras. (B) The removal of EDTA from various stages of APE confirms it essential for NH₂OH cleavage. Titration of NH₂OH (C) and mPEG-mal (D) reveals that saturating conditions are protein specific. GFP-RAB7 exhibits an NH₂OH independent mass shift, stressing the importance of proper optimization before further assays.

To confirm the observed APE mass shifts are site specific, we compared HA-HRas constructs containing single and double cysteine to alanine mutations (Fig. 12A). These constructs were additionally analyzed by alk-16 metabolic labeling to observe

how the results compared between the two assays (Fig. 12B). HEK293T cells were transfected overnight with the HA-HRas constructs, and incubated with 50 μ M alk-16 probe two hours prior to lysis. By APE, the absence of either or both S-palmitoylated cysteines results in distinct mass shift patterns corresponding with the number of available sites; single (C181A, C184A) cysteine constructs exhibited only one shift, while double (C181,184A) cysteines did not shift at all. Alk-16 labeling exhibited similar trends in signal, reflecting total S-fatty acylation in the sample.

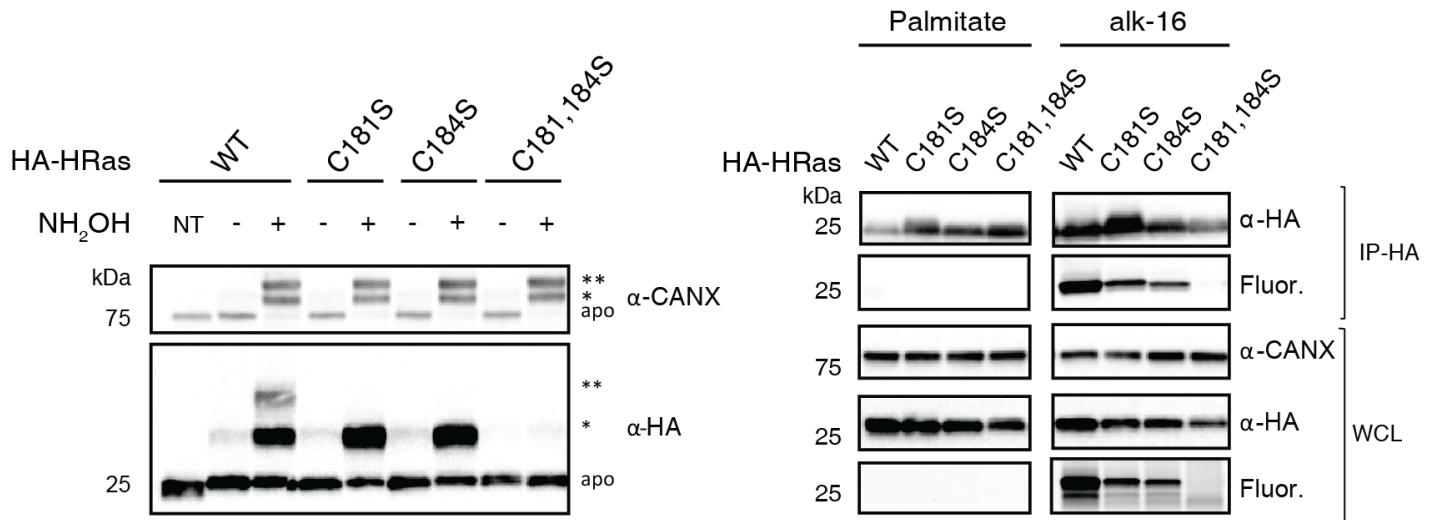


Figure 12. APE and metabolic labeling of HA-HRas. 293T cells transfected with HA-HRas constructs were incubated with 50 μ M alk-16 and split for analysis by APE (A) and metabolic labeling (B). APE displays mass shifts corresponding with the number of Cys present in the HRas construct. For metabolic labeling, samples were lysed, immunoprecipitated with anti-HA beads, and labeled with azido-rhodamine by CuAAC prior to SDS-PAGE.

To further demonstrate the applicability of APE, we analyzed several additional proteins that differ in topology, size and number S-fatty acylation sites (Fig. 13): CD9, a tetraspanin with 6 reported S-fatty acylation sites⁷⁴, showed 4 shifts. IFITM3, a single pass membrane protein with three known sites, showed three shifts, and IRGM1, a peripheral GTPase displayed a single shift. Additionally, pan-Ras antibodies were used

to observe endogenous Ras, which exhibited double and single mass shifts. The successful labeling of a variety of proteins provides strong evidence for the utility of APE. This assay equips us an accessible, novel analytical approach for S-fatty acylation, and demonstrates the potential in mass-tag labeling for investigating other post-translational modifications.

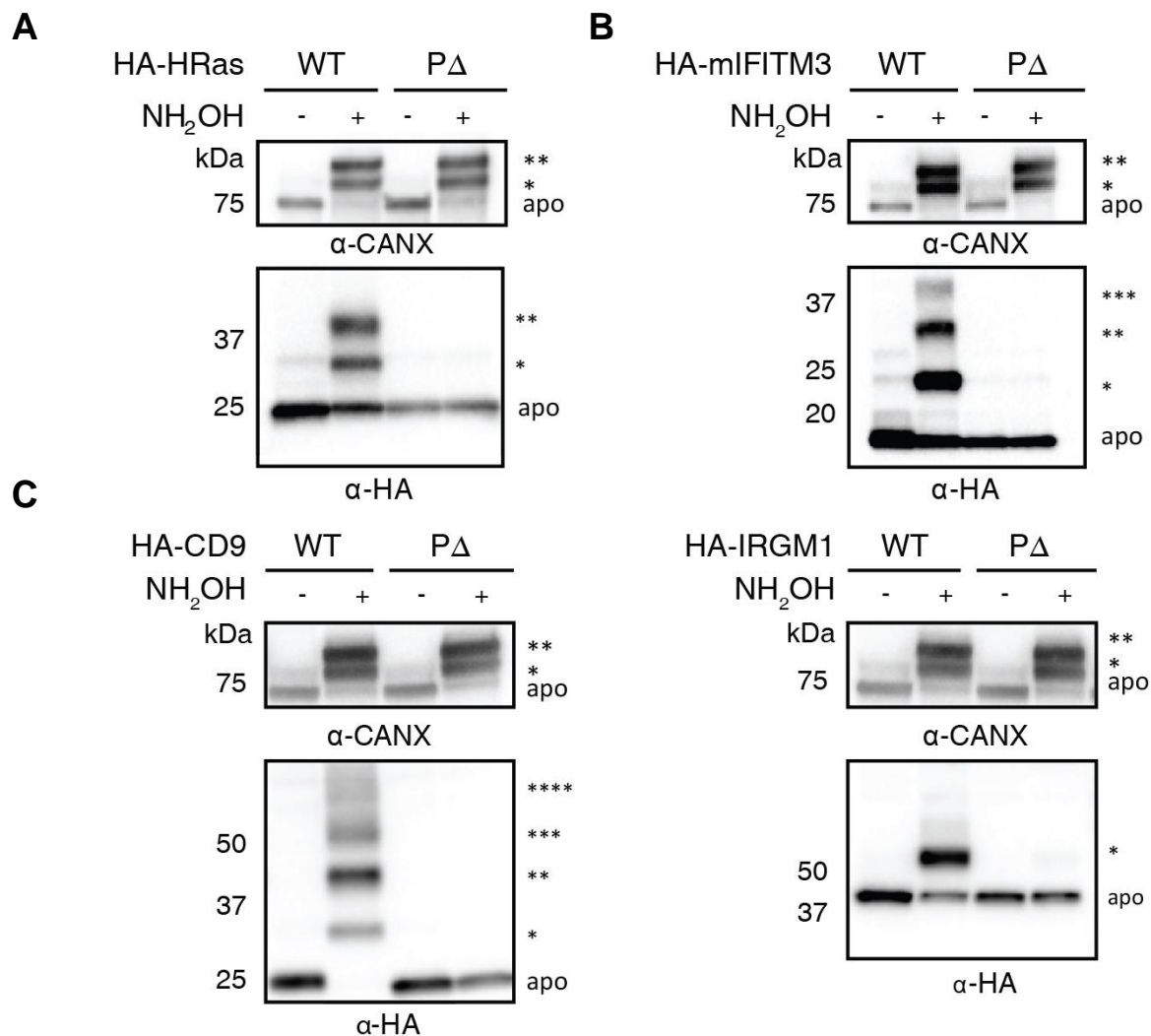


Figure 13. APE can be applied to proteins with varied topologies, molecular weights, and S-fatty acylation events. HEK293T cells were transfected with either WT or cysteine deficient (PΔ) constructs of HRas (A), IFITM3 (B), CD9 (C), IRGM1 (D) and analyzed by APE.

Chapter 2 methods (Published in Percher et al. PNAS 2016)

Acyl-PEG Exchange (APE)

Cell samples were lysed with 4% sodium dodecyl sulfate (SDS, Fischer) in TEA buffer (pH 7.3, 50 mM triethanolamine (TEA), 150 mM NaCl) containing 1x protease inhibitor cocktail (Roche), 5 mM PMSF (Sigma), 5 mM EDTA (Fischer) and 1500 units/mL benzonase (EMD). The protein concentration of the cell lysate was then measured using a BCA assay (Thermo), and adjusted to 2 mg/mL with lysis buffer. Typically, 200 μ g of total protein in 92.5 μ L of lysis buffer was treated with 5 μ L of 200 mM neutralized tris(2-carboxyethyl)phosphine (TCEP, Thermo) for final concentration of 10 mM TCEP for 30 minutes with nutation. N-ethylmaleimide (NEM, Sigma), 2.5 μ L from freshly made 1 M stock in ethanol, was added for a final concentration of 25 mM and incubated for 2 hours at room temperature. Reductive alkylation of the proteins was then terminated by methanol-chloroform-H₂O precipitation (4:1.5:3) with sequential addition of methanol (400 μ L), chloroform (150 μ L) and distilled H₂O (300 μ L) (all pre-chilled on ice). The reactions were then mixed by inversion and centrifuged (Centrifuge 5417R, Eppendorf) at 20,000 g for 5 minutes at 4° C. To pellet the precipitated proteins, the aqueous layer was removed, 1 mL of pre-chilled MeOH was added, the eppendorf tube inverted several times and centrifuged at 20,000 g for 3 minutes at 4° C. The supernatant was then decanted, and the protein pellet washed once more with 800 μ L of pre-chilled MeOH, centrifuged again and dried using a speed-vacuum (Centrivap Concentrator, Labconco) To ensure complete removal of NEM from the protein pellets, the samples were resuspended with 100 μ L of TEA buffer containing 4% SDS, warmed to 37° C for 10 minutes, briefly (~5 seconds) sonicated (Ultrasonic Cleaner, VWR) and

subjected to two additional rounds of methanol-chloroform-H₂O precipitations as described above.

For hydroxylamine (NH₂OH) cleavage and mPEG-maleimide alkylation, the protein pellet was resuspended in 30 µL TEA buffer containing 4% SDS, 4 mM EDTA and treated with 90 µL of 1 M neutralized NH₂OH (J.T. Baker) dissolved in TEA buffer pH 7.3, containing 0.2% Triton X-100 (Fisher) to obtain a final concentration of 0.75 M NH₂OH. Protease inhibitor cocktail or PMSF should be omitted, as these reagents can interfere with the NH₂OH reactivity. Control samples not treated with NH₂OH were diluted in 90 µL TEA buffer with 0.2% Triton X-100. Samples were incubated at room temperature for 1 hour with nutation. The samples were then subjected to methanol-chloroform-H₂O precipitation as described above and resuspended in 30 µL TEA buffer containing 4% SDS, 4 mM EDTA, warmed to 37° C for 10 minutes and briefly (~5 seconds) sonicated and treated with 90 µL TEA buffer with 0.2% Triton X-100 and 1.33 mM methoxypolyethylene glycol-maleimide (mPEG-Mal, 5 or 10 kDa, Sigma) for a final concentration of 1 mM mPEG-Mal. Samples were incubated for 2 hours at room temperature with nutation before a final methanol-chloroform-H₂O precipitation. Dried protein pellets were resuspended in 50 µL 1 X Laemmli buffer (BioRad) and then heated for 5 minutes at 95° C. Typically, 15 µL of the sample was loaded in 4-20% Criterion-TGX Stain Free polyacrylamide gels (Bio-Rad), separated by SDS-PAGE and analyzed by western blot. For western blots, primary antibodies used were anti-calnexin (1:2000 ab22595, Abcam), anti-Pan Ras (1:500, Ras10, Millipore), anti-mouse IFITM3 (1:1000, ab15592, Abcam) anti-FLAG (1:1000, F1804, Sigma) anti-HA (1:1000, ab9134, Abcam), and HRP-conjugated anti-HA (3F10, Roche). Secondary antibodies used were HRP-

conjugated goat anti-rabbit (DC03L, Calbiochem), and goat-anti-mouse (ab97023, Abcam). Protein detection was performed with ECL detection reagent (GE healthcare) on a BioRad ChemiDoc MP Imaging System

Cell Culture and Transfections

HEK293T, HeLa and RAW264.7 cells were obtained from ATCC. For transfection of HEK293T or HeLa cells, near confluent 6-well plates were transfected with 1 µg of plasmid DNA using 3 µL of Lipofectamine 2000 reagent (Life Technologies). After 24 hours, cells were collected by scraping, centrifuged at 500 g for 2 minutes, washed with 1X PBS, snap-frozen in dry ice/ethanol bath and stored at -80° C for future use. For NIH3T3 cells, near confluent 6-wells plates were transfected with 1 µg of plasmid DNA with 3 µL of Lipofectamine 3000 reagent (Life Technologies). After 6 hours, the media was replaced with fresh media to reduce toxicity of the Lipofectamine reagent. After 24 hours the cells were collected and stored for future use at -80° C. LPS (500 ng/mL, Enzo Life Sciences) and IFN-γ (100 U/mL IFN-γ, Thermo) activation of cells were performed as previously described¹³.

Acyl-Biotin Exchange (ABE)

The ABE protocol was performed as described⁶⁰. Following cell lysis, 400 µg of total cell lysate resubjected to reductive alkylation with TCEP and NEM as described above for the APE protocol. After the final methanol-chloroform-H₂O precipitation, the protein pellet was resuspended in 100 µL 4% SDS in 50 mM TEA, 150 mM NaCl pH 7.3, and 1 mM EDTA. The samples were split into two 50 µL aliquots and treated with 1M NH₂OH or control buffer (200 µg/condition). For the NH₂OH-treated sample, 150 µL NH₂OH-HPDP-biotin buffer (for 160 µL of buffer: 3.2 µL of HPDP-Biotin (50 mM stock in DMSO, Sigma), 36.8 µL of dimethylformamide (DMF, Fisher Scientific), 3.2 µL of 10% Triton X-100 in H₂O, 112 µL of 1 M NH₂OH in H₂O pH 7.3, 4.8 µL H₂O) was added to the sample for a final concentration of 0.75 M NH₂OH, 1% SDS (lysate:NH₂OH-HPDP-biotin buffer 1:3). For the NH₂OH-negative control, the samples were treated with 150 µL of HPDP-biotin buffer (for 160 µL of buffer: 3.2 µL of HPDP-Biotin (50 mM stock in DMSO), 36.8 µL of DMF, 3.2 µL of 10% Triton x-100 in H₂O, 16 µL of 500 mM TEA 1.5 M NaCl pH 7.3, 101.8 µL H₂O) was added to the negative control sample for a final concentration of 1% SDS (Lysate: Buffer 1:3). The mixture was incubated at room temperature with end-over-end rotation for 1 hour. Proteins were precipitated (methanol-chloroform-H₂O precipitation) and resuspended in 50 µL 4% SDS 50 mM TEA pH 7.3, 150 mM NaCl, 1mM EDTA (final concentration 4 mg/mL). 150 µL HPDP-biotin low concentration buffer (for 300 µL of buffer: 1.2 µL of HPDP-Biotin (50 mM), 13.8 µL of DMF, 6 µL of 10% Triton X-100 in H₂O, 30 µL of 500 mM TEA 1.5 M NaCl pH 7.3, 249 µL H₂O) was added to both samples (HPDP-biotin: lysate 3:1). The samples were incubated at room temperature with end-over-end rotation for 1 hour, subjected to

methanol-chloroform-H₂O precipitation as described above and resuspended in 100 μ L 0.2% SDS 0.2% Triton X-100 50 mM TEA, 150 mM NaCl, pH 7.3. High-affinity streptavidin-agarose beads (Thermo, 20 μ L of bead slurry/200 μ g of protein) were washed with 50 mM TEA, 150 mM NaCl, 0.2% Triton X-100, pH 7.3 (3x). The resuspended samples were then added to the beads and incubated at room temperature with end-over-end rotation for 90 minutes. The supernatant from the beads was decanted and boiled with 4x Laemmli sample buffer (LSB) (supernatant:LSB:BME 3:1:0.1) at 95° C for 5 min. The beads were washed with 1% SDS in PBS for 2 minutes, and centrifuged at 1700 g for 1 minute (2x). The beads were then washed in 4 M Urea (Sigma) in PBS (3x), PBS (3x). The beads were boiled at 95° C for 10 minutes with 1x Laemmli sample buffer (LSB:BME:4% SDS 50 mM TEA, 150 mM NaCl pH 7.3, 0.9:0.1:3), separated by SDS-PAGE and analyzed by western blot. Typically, 40 μ g of protein were loaded on the gel.

Acyl-Resin Assisted Capture (acyl-RAC).

Following reductive alkylation of total lysate (400 μ g) with TCEP and NEM as described above for the APE and ABE, the samples were resuspended in 50 μ L 4% SDS, 50 mM TEA, 150 mM, 150 mM NaCl, 1 mM EDTA, pH 7.3. The samples were split into two 25 μ L aliquots - or + NH₂OH (200 μ g/condition). For the NH₂OH-treated sample, 75 μ L NH₂OH 1 M, 0.2% Triton X-100, pH 7.3 in H₂O was added to the "+NH₂OH" sample for a final concentration of 0.75 M NH₂OH, 1% SDS (Lysate: NH₂OH solution 1:3). For the negative control not treated with NH₂OH, 75 μ L 50 mM TEA, 0.2% Triton X-100, 150 mM NaCl pH 7.3 was added to the samples ("-NH₂OH") for a final concentration of 1% SDS (Lysate:Buffer 1:3). To capture proteins with free thiols, thiol-

sepharose beads 6B (T8387, Sigma) were soaked in 1 mL H₂O for 30 minutes. Beads were washed three times with 0.5 mL of 50 mM TEA 150 mM NaCl, 0.2% Triton X-100, pH 7.3. Each sample (100 µL of +/- NH₂OH) was added to the thiol-sepharose beads (200 µg of proteins/6.25 mg thiol-sepharose beads) and incubated at room temperature for 3 hours with end-over-end rotation. The supernatants from the beads were decanted and boiled with 4x Laemmli sample buffer (LSB:BME:supernatant 0.9:0.1:3) for 5 min. The beads were washed with 1% SDS in PBS (3 x 2 min), 4 M Urea in PBS (3x), PBS (3x). Beads were boiled at 95° C for 10 minutes with 1x Laemmli sample buffer (LSB:BME:4% SDS 50 mM TEA, 150 mM NaCl pH 7.3, 0.9:0.1:3), separated by SDS-PAGE and analyzed by western blot. Typically, 40 µg of protein were loaded on the gel.

Metabolic labeling and in-gel fluorescence profiling

For metabolic labeling of cells with alkyne-palmitic acid reporter (t), HEK293T cells transfected with HA-HRas constructs or NIH3T3 cells transfected with HA-mIFITM3 constructs were incubated for two hours with 50 µM alk-16 (synthesized as previously reported) in DMEM containing 2% (v/v) charcoal-dextran stripped FBS (Lot: AZA180873, HyClone). Cells were harvested by trypsinization, washed once in PBS, pelleted and lysed in 1% (w/v) Brij 97 (Sigma) in 50 mM TEA 150 mM NaCl pH 7.3 with 5X concentration of EDTA-free protease inhibitor cocktail (Roche). Total protein concentration was measured by BCA assay (Life Tech). For immunoprecipitation, 200 µg of total protein was added to 20 µL of anti-HA antibody-conjugated agarose (Sigma) in a total volume of 250 µL and rocked at 4° C for 16 hours. Agarose beads were washed twice by resuspension in 1 mL of wash buffer (1% Triton X-100, 1% sodium deoxycholate (Sigma), 0.1% SDS in 50 mM TEA, 150 mM NaCl pH 7.3) and centrifuged

at 3500 g for 30 seconds. The beads were then resuspended in 20 μ L of 1% (w/v) Brij in 50 mM TEA 150 mM NaCl pH 7.3 and 5 μ L of CuAAC reactant solution (0.5 μ L of 5 mM azido-rhodamine (final concentration 200 μ M), 1 μ L of 50 mM freshly prepared CuSO₄·5H₂O in H₂O (final concentration 2 mM, Sigma), 1 μ L of 50 mM freshly prepared TCEP (final concentration 2 mM) and 2.5 μ L of 2 mM tris[(1-benzyl-1*H*-1,2,3-triazol-4-yl)methyl]amine (TBTA) (final concentration 200 μ M, synthesized as previously reported). Beads were rocked with the CuAAC reactant solution at room temperature for 1 hour and washed twice with wash buffer as described above. The proteins were eluted addition of 30 μ L 1X Laemmli sample buffer (LSB:BME: 4% SDS 50 mM TEA, 150 mM NaCl pH 7.3, 1:0.1:3), heated for 5 minutes at 95° C and separated by SDS-PAGE. In-gel fluorescence scanning was performed using a Typhoon 9400 imager (Amersham Biosciences). Western blots for HA-tagged proteins were performed using an anti-HA tag-HRP conjugated antibody (1/1,000 Roche).

Influenza virus infection

NIH3T3 cells were transfected with Lipofectamine 2000 (Thermo) overnight in 12-well plates using 1 μ g of plasmid per well. Media was removed and replaced with 400 μ L of media +/- influenza virus strain A/Puerto Rico/8/34 (H1N1, commonly referred to as PR8) at an multiplicity of infection (MOI) of 5 for each well. Infection was allowed to proceed for 18 hours. Cells were collected and fixed for 10 minutes with 4% paraformaldehyde. Fixed cells were then permeabilized with 0.1% Triton X-100 in PBS for 10 minutes and blocked with 2% FBS in PBS for 20 minutes. All antibody staining and washing was performed using the 0.1% Triton X-100 solution. Staining with anti-HA antibody (HA.11, Covance, 1:1000) was performed for 20 min at room temperature

followed by three washes and staining with anti-mouse secondary antibody conjugated to Alexafluor-488 (Life Technologies, 1:1000). After an additional three washes, cells were stained with anti-influenza NP antibody (ab20343, Abcam, 1:300) that was directly conjugated in-house to Alexafluor-647 using the 100 ug antibody labeling kit from Life Technologies. Samples were analyzed using a Becton Dickinson FACSCanto II flow cytometer and HA-positive cells were analyzed for the percentage of cells staining positive for influenza NP indicating cellular infection using Flowjo software as previously described.

Immunofluorescence analysis

For the analysis of mIFITM3 colocalization with endosomal/ lysosomal markers, 50,000 NIH3T3 cells/well were plated in a 24 well plate, and co-transfected the next day with 0.25 µg HA-IFITM3 and 0.25 µg of either GFP-Rab5, GFP-Rab7 (54244, addgene), or LAMP1-GFP (34831, addgene) with 1.5 µL Lipofectamine 3000 (Thermo) for four hours, then incubated with fresh media for an additional 12 hours. Cells were fixed for 15 min with 3.7% paraformaldehyde, washed 3x with PBS, permeabilized with 0.1% saponin in PBS for 10 minutes, and blocked for 60 minutes with 1% BSA in PBS. All antibody staining and washing was performed with 0.1% saponin in PBS. Cells were incubated with goat anti-HA antibody (1/1000, ab9134, Abcam) in 1% BSA for one hour at room temperature. After three, 5 minute washes, samples were incubated with donkey anti-goat antibody conjugated to Alexafluor-647 (1/1000, A-21447, Invitrogen) in 1% BSA. Cells were washed, and mounted using ProLong Gold antifade reagent (Invitrogen). Images were obtained from an Inverted Zeiss Axio Observer Z1 microscope, and processed with ImageJ. Pearson coefficient was calculated using Imaris 8 software.

Chapter 3: Characterization of endogenous IFITM3 S-fatty acylation.

Having confirmed with model proteins that APE can observe different levels of S-fatty-acylation by western blot, we further explored the S-fatty acylation of IFITM3. Previous work in our lab has shown by alk-16 metabolic labeling that IFITM3's three cysteines are S-fatty acylated, and that the mutation of all three to Ala disrupt anti-viral activity¹⁵. Additionally, the mutation of C72 alone was sufficient to disrupt anti-viral activity against IAV and Dengue virus¹⁰. While this suggests S-fatty acylation plays a role in IFITM3's function, it was still unclear how many sites were modified simultaneously. Understanding S-palmitoylation levels would further our understanding of the physiological state of IFITM3, and how it relates to its anti-viral activity.

S-fatty acylation levels of murine IFITM3

We first analyzed murine IFITM3 (mIFITM3), as doing so furthers our understanding of S-fatty acylation levels in a commonly used model for *in vitro*¹³ and *in vivo*^{21,75} experimental assays. Incubation times for mPEG-mal and NH₂OH were compared for background mass shifts and completion of cleavage respectively (Fig. 14). Both conditions showed complete labeling and cleavage under standard conditions used for other samples. To determine how specific Cys sites contribute to mIFITM3 S-fatty acylation levels, overexpressed HA-tagged constructs were analyzed by APE and alk-16 metabolic labeling. Similar to earlier reports in DC2.4 dendritic cells¹³, alk-16 incorporation onto mIFITM3 decreased in a cysteine dependent manner (Fig. 15A); C71A and C105A showed a similar loss of labeling, while C72A showed the greatest decrease.

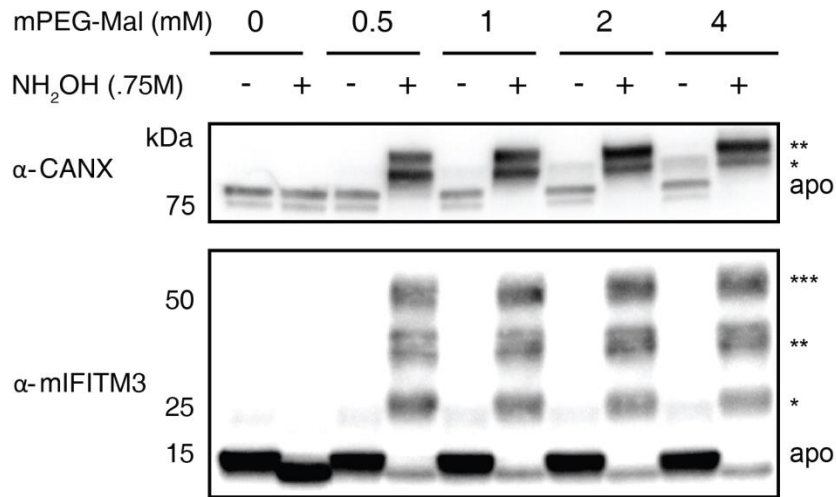


Figure 14. mPEG-Mal concentration optimization of IFITM3. NIH3T3 lysate was analyzed by APE with varying concentrations of mPEG-Mal. No change in ratios was observed at concentrations higher than 1 mM. The number of PEGylation events are indicated by asterisks (*).

With APE, overexpressed WT IFITM3 displayed four distinct bands, reflecting the presence of non-modified (apo), mono, di, and tri-PEGylated populations (Fig. 15B, 2nd lane). In comparison, the individual and dually-mutated cysteines show distinct PEGylation patterns: the mutation of either Cys 71 or Cys 105 to alanine, shows two mass shifts (mPEG-Mal, di-PEGylated) while the mutation of C72A shows only one (4th lane). To elucidate how Cys specific S-fatty acylation correlates with anti-viral activity, we next compared the differences in viral infectivity in cells transiently overexpressing the IFITM3 constructs (Fig 15C). C71A displayed similar infection levels to that of the WT, while the mutation of C72 or C105 interfered with viral inhibition. This data, combined with the metabolic labeling, indicate that S-fatty acylation levels of mIFITM3 alter the anti viral activity. While it is impossible to discern whether a specific S-acylated population is more active, the dually mutated constructs show that the presence of a single S-fatty acylation site at Cys 72 (C71,105A) is sufficient to restore a significant

portion of the anti-viral activity. Cys 72's contribution to protein function, together with the disruption of dual, and tri-PEGylated levels by APE suggests that its S-fatty acylation may play a key role in the anti-viral activity of the protein.

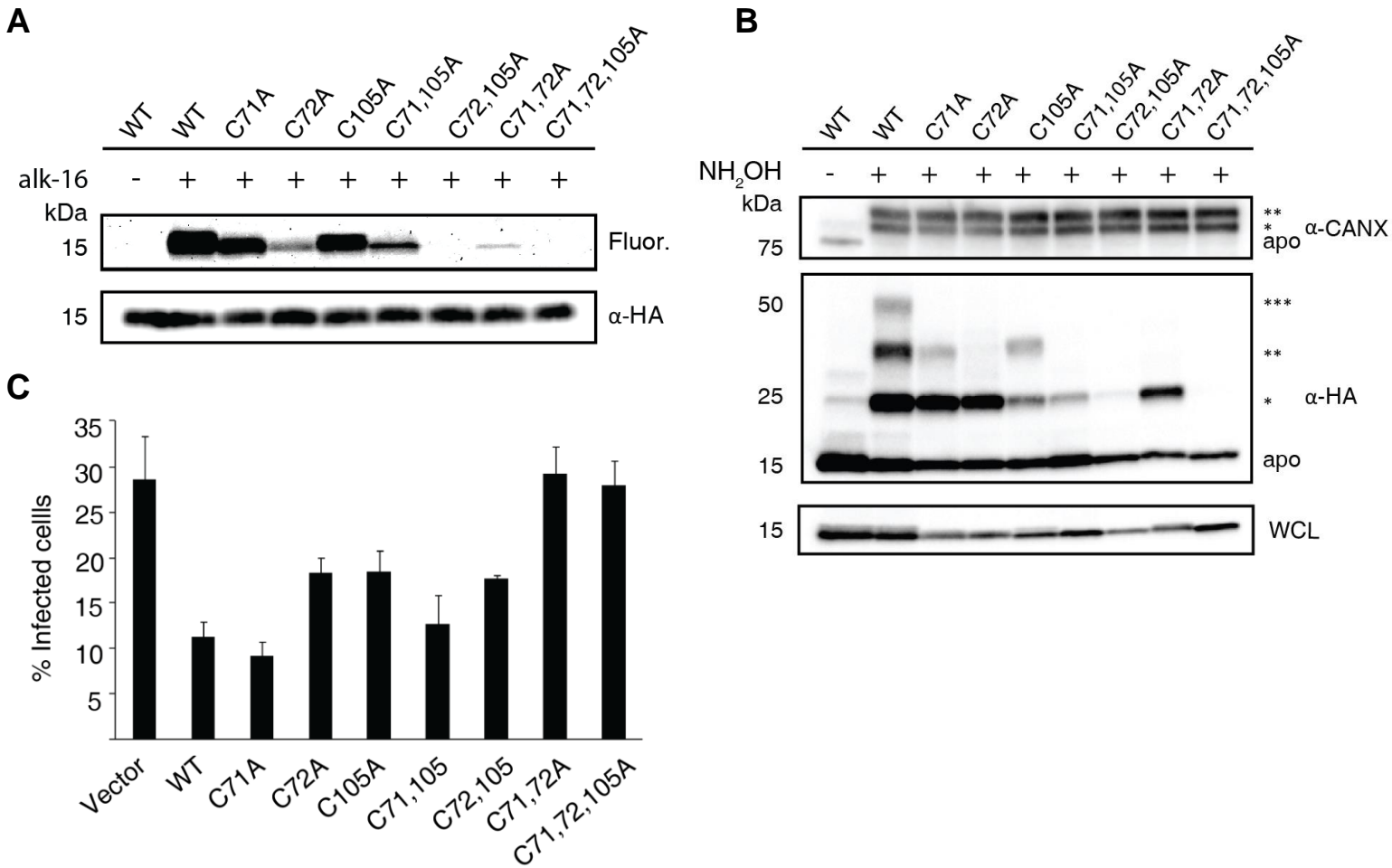


Figure 15. Murine IFITM3 APE PEGylation levels and antiviral activity. (A) NIH3T3 cells transfected with HA-mIFITM3 constructs were labeled for 2 hours with 50 μ M alk-16. Cell lysates were prepared with Brij-97, the HA constructs immunoprecipitated with anti-HA agarose-beads, reacted with azide-rhodamine by CuAAC, separated by SDS/PAGE, and visualized by fluorescence gel scanning. (B) NIH3T3 cells were transfected with similar HA-mIFITM3 constructs and analyzed by APE. The number of PEGylation events are demarcated by asterisks (*). (C) NIH3T3 cells were transfected with HA-mIFITM3 constructs, followed by infection with PR8 influenza virus at a multiplicity of infection of 5, for 18 hours. Cells were fixed, permeabilized, stained with anti-influenza NP antibody and analyzed by flow cytometry. Graph shows anti-influenza NP+ cells for each condition. Average of triplicate. Error bar represents SEM

Though the overexpressed constructs of IFITM3 are critical for understanding the role of Cys specific S-fatty acylation, our method of transient transfection results in non-homogenous transfection, at higher expression levels than endogenous IFITM3 (data not shown). Both can potentially distort the levels of S-fatty acylation. We therefore determined the endogenous levels of S-fatty acylation levels of mIFITM3 in mouse RAW 264.7 Macrophage, and NIH-3T3 fibroblast cell lines (Fig. 16). Both cell types exhibited three mass shifts, with minimal apo-protein, indicating that the majority of endogenous IFITM3 is S-fatty acylated at least once. This data indicates 7 possible combinations of S-fatty acylation are physiologically present in cells.

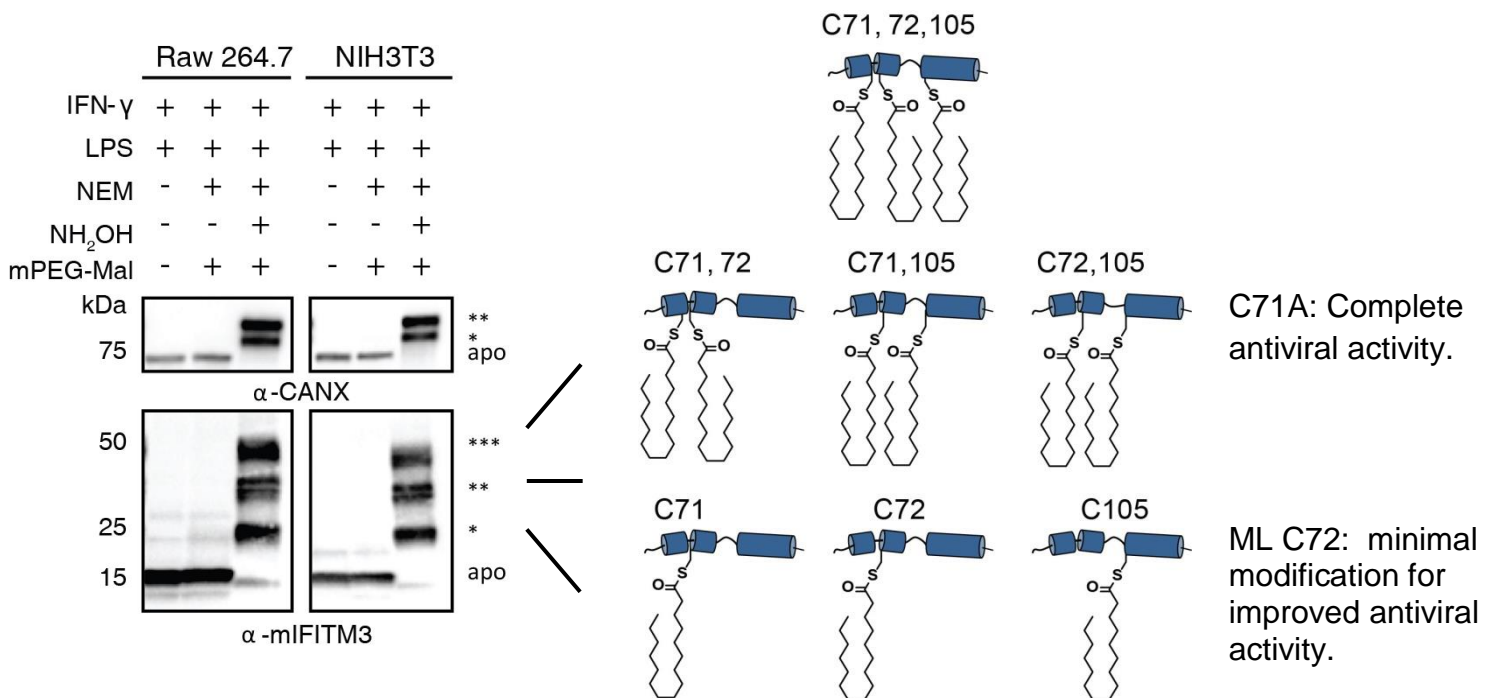


Figure 16. APE of endogenous murine IFITM3. *Left:* Possible S-fatty acylation isoforms observed by APE. Mouse macrophage (Raw 264.7) and fibroblast (NIH3T3) cell lines were incubated overnight with IFN- γ and LPS, and analyzed by APE. The number of PEGylation events is indicated by asterisks (*). *Right:* APE mass shifts cannot discern between different combinations of S-acylation. Possible S-fatty acylation isoforms are described that would reflect a corresponding mass shift.

APE analysis of S-fatty acylation levels of human IFITM3.

Similar to mIFITM3, overexpressed human IFITM3 (hIFITM3) in HEK293T cells show by APE three PEGylation levels for WT hIFITM3 (Fig. 17A). Both C71A, and C72A show primarily one PEGylation shift, of similar signal intensity, different slightly from the mIFITM3 constructs, where C71A contains two shifts. C105A shows two shifts, as observed in mIFITM3. For the double Cys mutants, the presence of Cys72 was sufficient to retain similar mono-PEGylated levels to the single Cys mutants. Interestingly, when containing only Cys 71, or Cys105 (C72,105A, C71,72A, respectively), a large decrease in signal was observed, suggesting an overall loss of S-fatty acylation.

We next compared the antiviral activity of the hIFITM3 Cys constructs (Fig. 17B). As with mIFITM3, C71A did not alter its activity, with similar levels of infected cells to that of WT. C72Ala had higher levels of infection, though less than the vector or triple mutant construct (C71,72,105A). With the double mutants, Cys71 alone (C72, 105A) resulted in a complete loss of function, while Cys72 alone (C71, 105A) retained partial levels of activity. Notably, distinct from mIFITM3, Cys105 alone (C71,72A) showed similar levels of antiviral activity to C71,105A. This indicates that a minimal S-acylation construct of Cys105 is sufficient to retain a similar level of anti-viral activity to that of Cys72. For endogenous hIFITM3 S-acylation, A549 cells were analyzed by APE after overnight activation with IFN- γ (Fig. 17C). A549, a human lung type II alveolar epithelial cell line ⁷⁶, is a clinically relevant tissue type for investigating IFITM3 expression. Interestingly, a notable difference in APE PEGylation levels are observed in comparison to endogenous mIFITM3; the majority of the protein is dually-PEGylated, and no tri-

PEGylated level is observed. This indicates that most of the protein is dually S-fatty acylated, and that six possible combinations are potentially present (Fig. 17D). As the disruption of Cys71 does not alter anti-viral activity, the likely S-acylated state of IFITM3 in A549 is the dually-S-acylated C72,105.

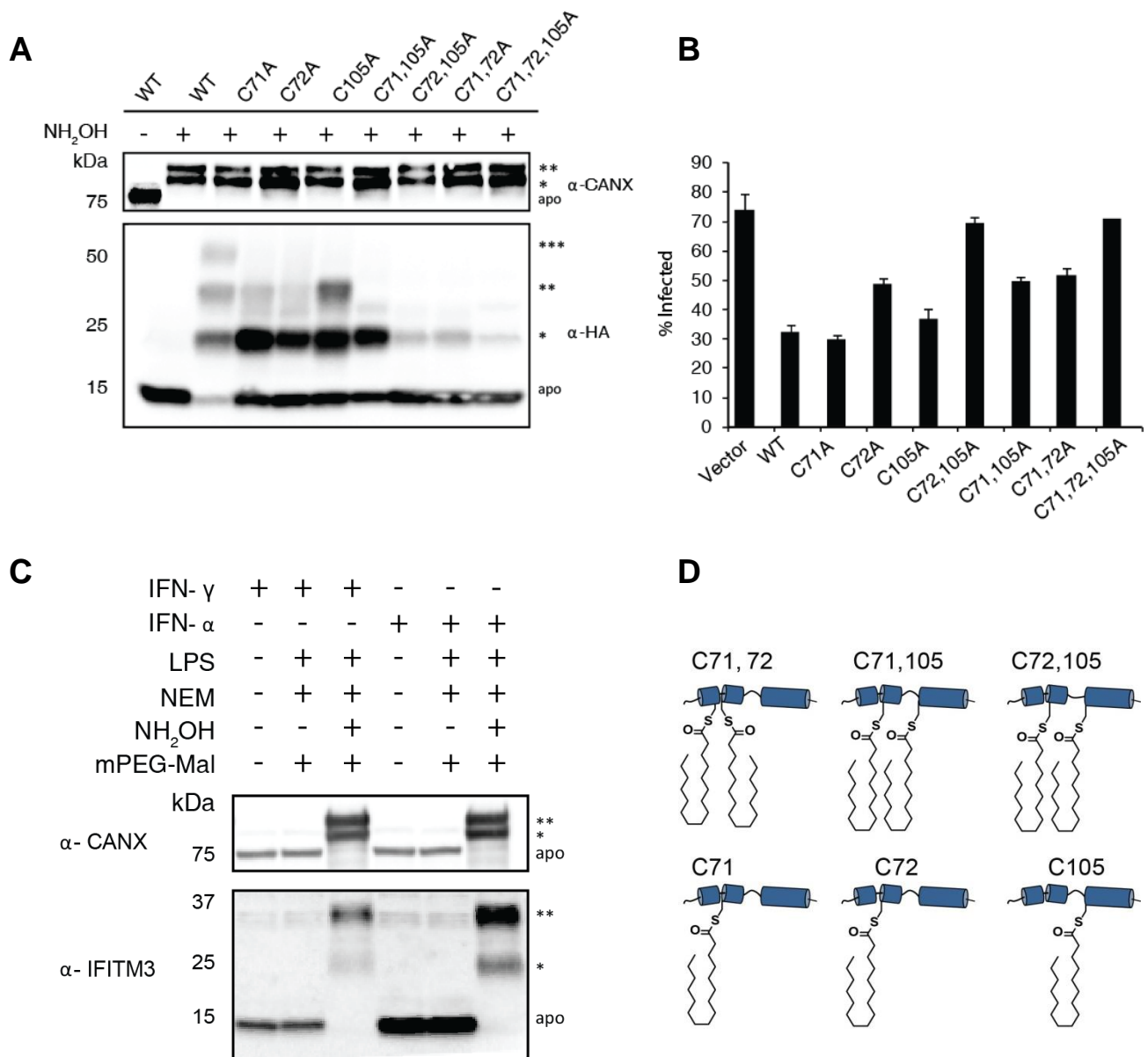


Figure 17. APE and antiviral activity of human IFITM3. (A) HA-hIFITM3 constructs were expressed in HEK293T cells and analyzed by APE. PEGylation events are indicated by asterisks (*). (B) HEK293T cells transfected with wild-type, and cysteine mutant constructs of HA-hIFITM3, were infected with PR8 influenza virus at an MOI of 5 for 18 h. Cells were fixed, permeabilized with 0.1% Triton X-100, and stained with anti-influenza NP antibodies. Graph of influenza-NP+ cells for each condition. Error bars represent SEM, N = 3. (C) IFN stimulated A549 cells were analyzed by APE. PEGylation events are indicated by asterisks (*). (D) Depiction of possible S-fatty acylation combinations in C.

Chapter 4: Generation of recombinant IFITM3 and lipidated isoforms.

Since the discovery of IFITM3 anti-viral activity³⁸, a considerable body of work has been published on its localization, post-translational modifications¹³ and range of antiviral activity (table 1). While it has previously been shown that the point of interference is viral content delivery^{27,38}, the mechanism of IFITM3 activity remains controversial. Conflicting reports make it unclear whether IFITM3 directly interacts with the virus, alters the late endosome membrane environment, or indirectly interacts with an unknown cofactor (Fig. 4). To eliminate the complexity of the cellular environment and selectively control potential key parameters of IFITM3's mechanism (membrane lipid composition, protein concentration etc.) we directed our efforts towards the generation of recombinant human IFITM3 (rIFITM3). This enables a minimalist model of reconstituted protein in liposomes (proteoliposomes) and supported bilayers for viral fusion assays, allowing us to address whether IFITM3 alone is capable of inhibiting viral fusion.

Generation of recombinant IFITM3.

To minimize interfering factors, we designed the purification of rIFITM3 in a manner that limited denaturation of the protein, or retained any tags used for enrichment and purification¹⁷. We therefore utilized the His-SUMO tag that both increases the solubility of membrane proteins, and is cleaved C-terminal to the SUMO dual-glycine motif, generating native IFITM3⁷⁷ (Fig. 18B). Building off the purification conditions for the similarly sized SNARE membrane proteins⁷⁸, we were able to enrich rIFITM3 at concentrations as high as 1 mg / mL, and isolate purified rIFITM3 through the use of size exclusion chromatography (SEC, Fig. 18C).

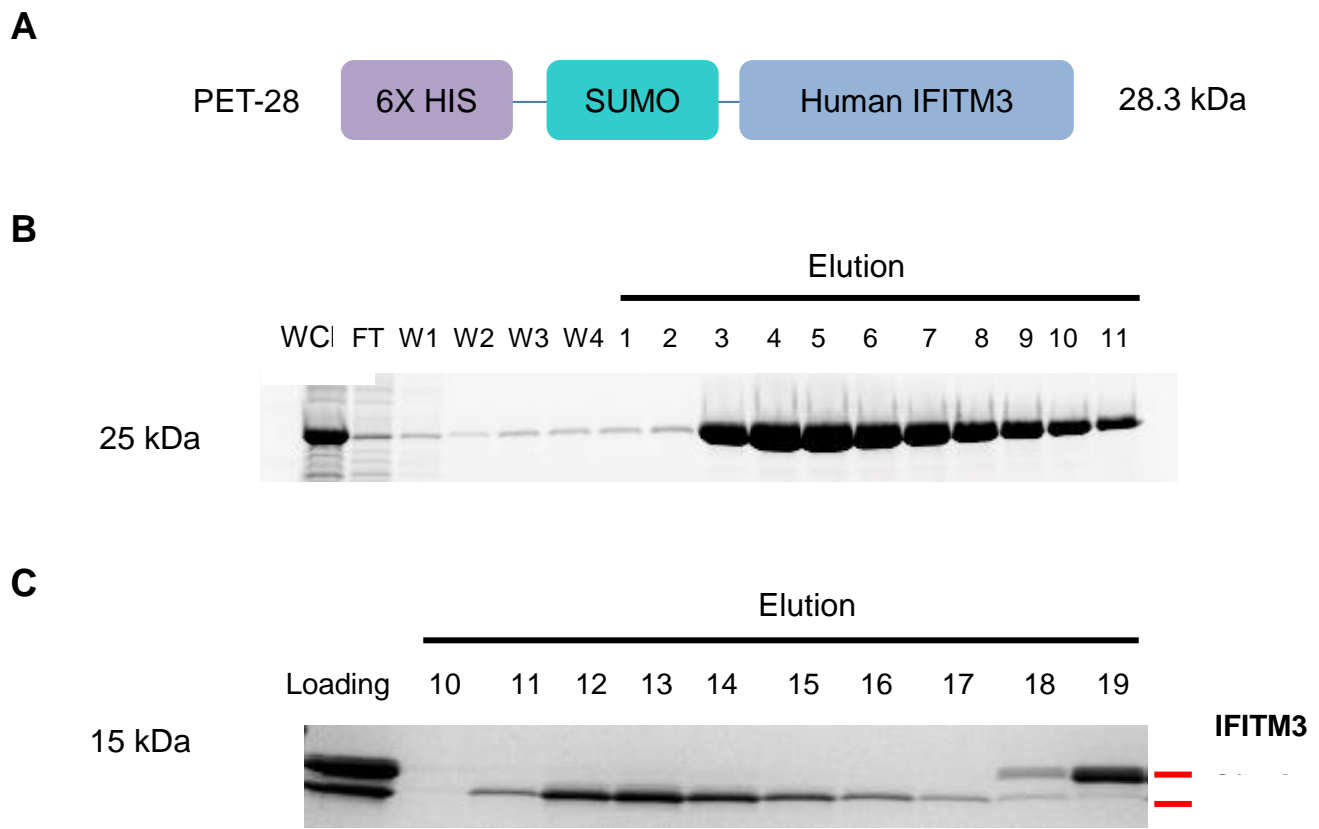


Figure 18. Purification of recombinant IFITM3. (A) Schematic of rIFITM3 construct containing HIS tag, cleavable SUMO domain, and codon-optimized hIFITM3. (B) Immobilized metal affinity chromatography (IMAC) is used to enrich and purify rIFITM3. WCL: Whole cell lysate. FT: Flow through. W: Wash. (C) SEC improves purity of rIFITM3 and isolates the sumo domain from the rest of the sample.

Lipidation of recombinant IFITM3.

A critical aspect of generating rIFITM3 is replicating the correct post-translational modifications. To emulate S-fatty acylation, rIFITM3 constructs containing one or two Cys were modified with a maleimide-palmitate (mal-palm) to introduce a covalent saturated 16 carbon chain analog (Fig. 19). We have previously used maleimide (chapter 2) to specifically modify cysteines under similar conditions.

To confirm that we can successfully label rIFITM3 with our mal-palm analog, we first tested and optimized the labeling of Cys72 on rIFITM3. Labeling with mal-palm resulted in a slower migration during analysis by SDS-PAGE. While the protein did not undergo complete labeling at 4 °C (Fig. 19B) , and precipitated at RT, we observed near complete labeling at 15 °C , in a Cys-specific manner, indicating the gel-shift was not due to background labeling. Labeling was further confirmed by MALDI-TOF mass spectrometry (Fig. 19C).

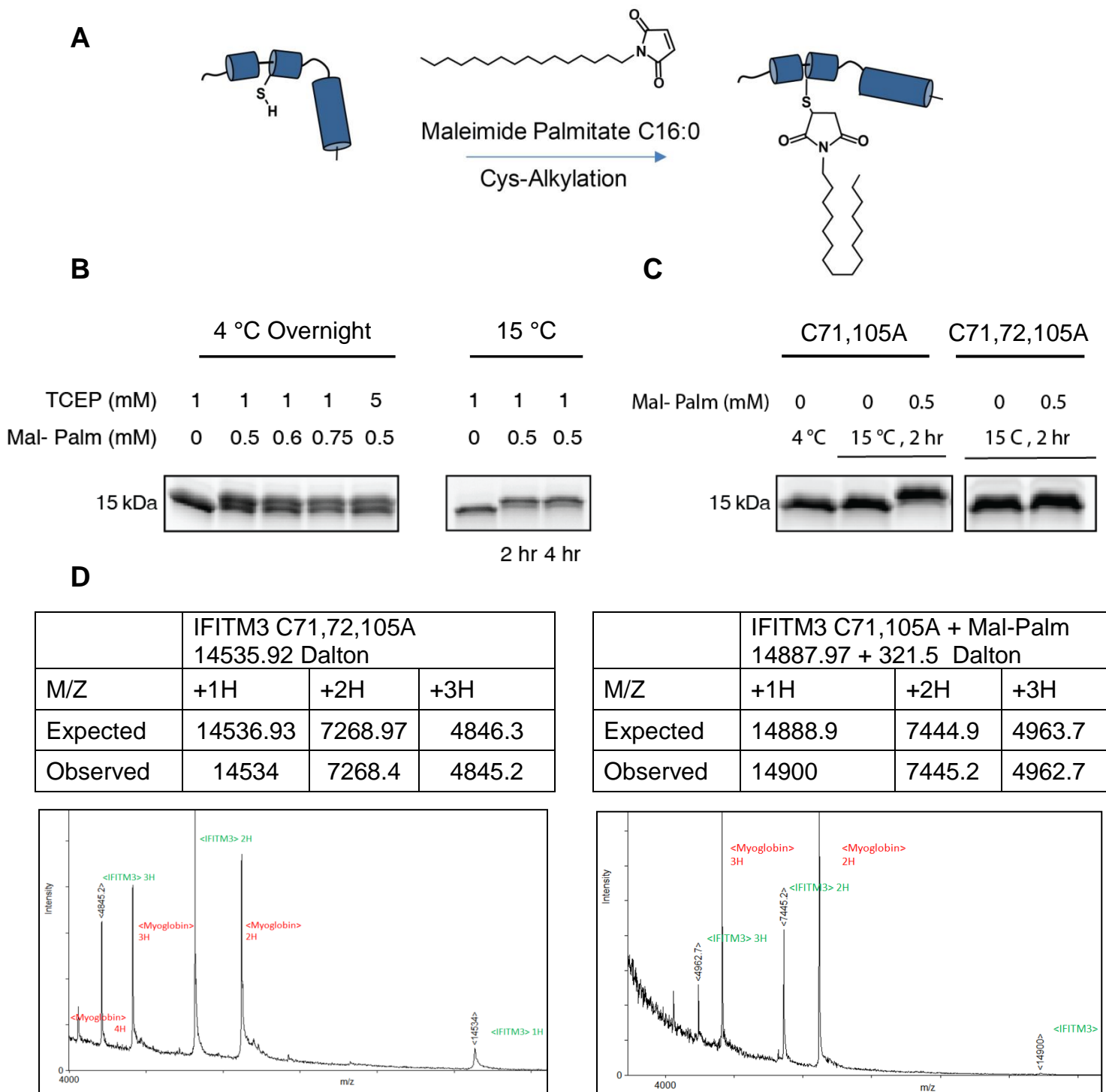


Figure 19. Mimicking S-fatty acylation of rIFITM3 with maleimide-palmitate. (A) Schematic of rIFITM3 labeling. Thiol-specific maleimide covalently labels rIFITM3, introducing a saturated 16 carbon chain. (B) Labeling optimization of Cys 72 rIFITM3. (C) Cysteine specificity of mal-palm. Cys 72 rIFITM3 (C71,105A) shows a Cys dependent mass shift when analyzed by SDS-PAGE. apoIFITM3 (containing no cysteines) under similar conditions does not shift. (D) MALDI-TOF confirmation of mal-palm labeling.

Having confirmed that we can specifically label rIFITM3 Cys72, we generated a panel of mal-palm labeled rIFITM3 isoforms to determine whether site-specific lipidation alters the efficiency of anti-viral activity. Analysis of A549 cells by APE showed the majority of endogenous IFITM3 displayed two mass-shifts, indicating that most of IFITM3 is likely dually S-fatty acylated (Fig. 20). This reduced the complexity of our panel of rIFITM3 isoforms, as it implies that the triple-S-fatty acylated state does not occur in our tested human cell lines. As C71A does not compromise the anti-viral activity of hIFITM3 and a significant portion of activity was restored in the presence of a mono-lipidated Cys72, or Cys105 (Fig. 17B), we first generated three different mal-palm constructs: mono-lipidated C72 (ML-C72), mono-lipidated C105 (ML-C105), and dually-lipidated C72,105 (DL-C72,105) (Fig 20).

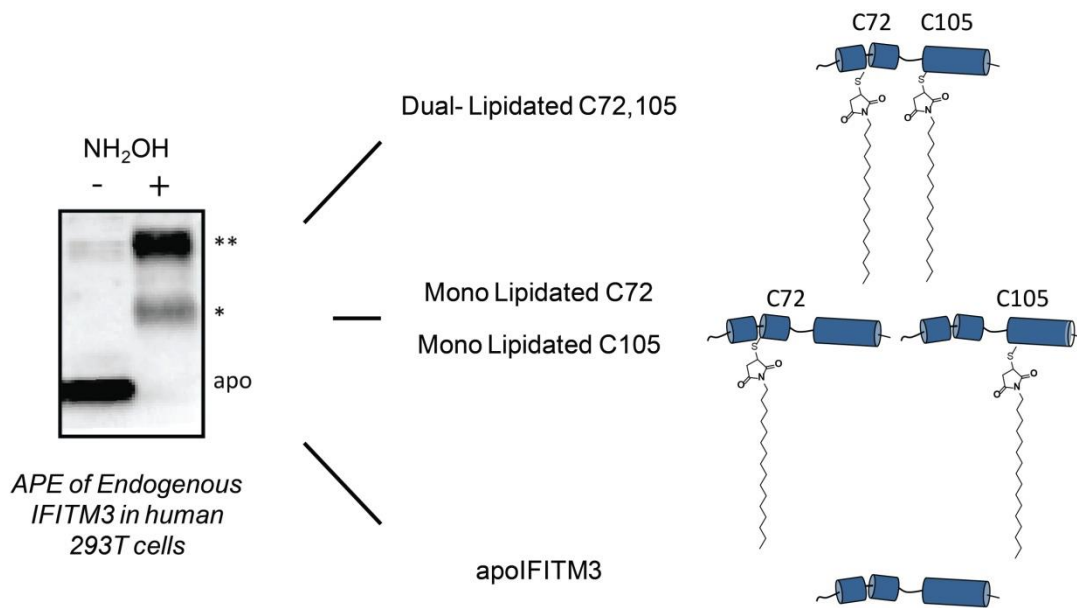


Figure 20. Mal-palm labeling of rIFITM3 S-fatty acylation isoforms. APE of A549 cells reveal that the majority of endogenous IFITM3 is dually lipidated (**). To generate the relevant isoforms, mono-lipidated Cys 72, and 105 (*), and dual lipidated Cys 72,105 were reacted with mal-palm.

To optimize labeling of rIFITM3 with mal-palm for the additional rIFITM3 constructs, incubation times and concentrations were varied, and compared by SDS-PAGE (Fig. 21A,B). The constructs were then labeled and purified under optimal labeling conditions and confirmed by MALDI-TOF mass spectrometry (Fig. 21C,D).

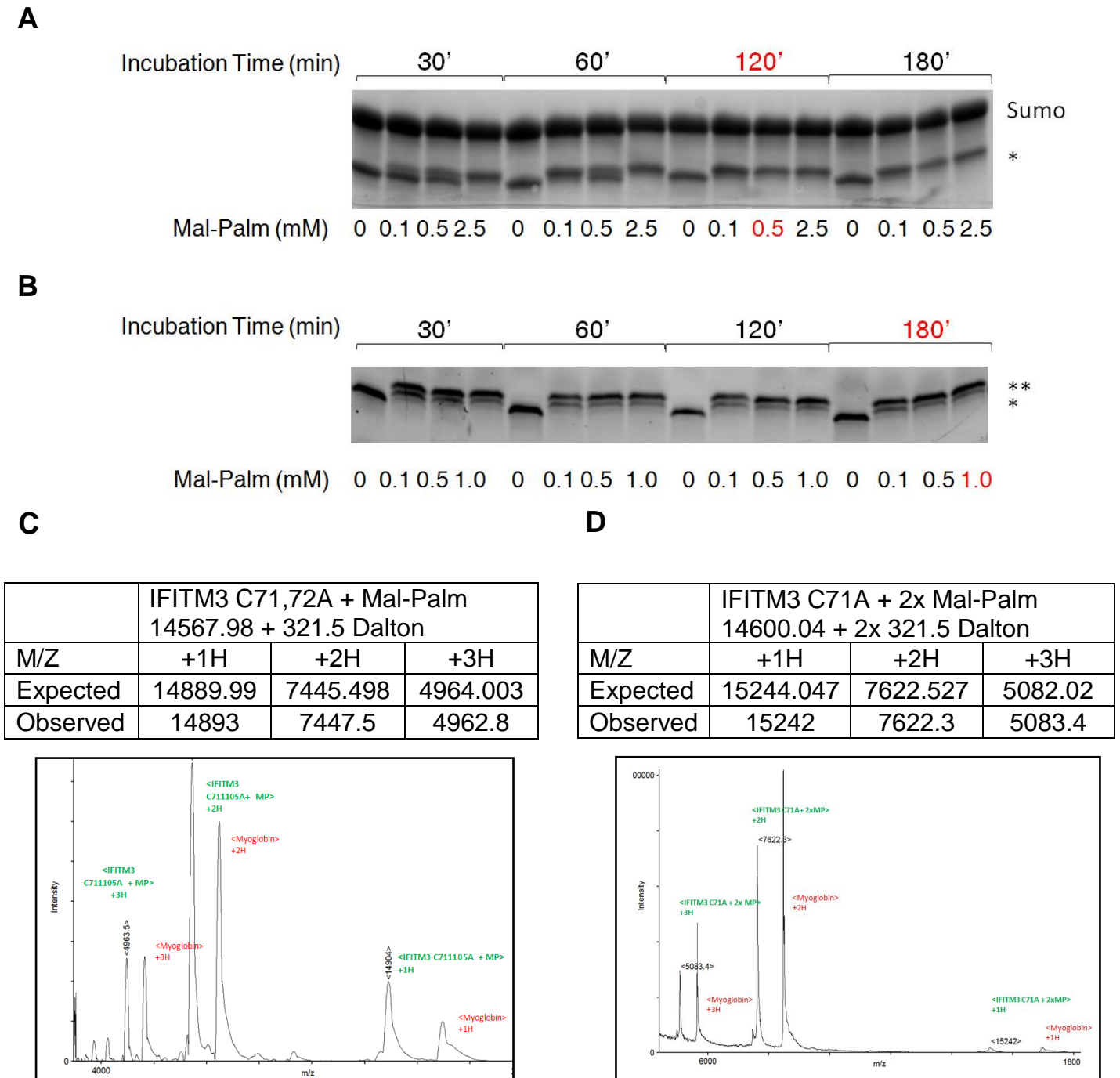


Figure 21. Mal-palm labeling optimization and mass-spec confirmation. (A) rIFITM3-Cys 105 was incubated with 1.0 mM TCEP and up to 2.5 mM Mal-Palm (controls were incubated with 5% DMSO). A single mass shift (*) was observed. Chosen conditions for future purifications are highlighted in red. (B) rIFITM3-Cys 72,105 was incubated with 1.0 mM TCEP and up to 1.0 mM mal-palm. Two discernible mass shifts (*, **), though the majority of the protein signal was observed with the double shift. Chosen conditions for future purification are labeled in red. MALDI-TOF mass spectrometry confirmed single labeling of IFITM3 C71,105A (C), and double labeling of IFITM3 C71A (D).

Chapter 4 Methods:

Generation of Recombinant IFITM3:

To improve purification human IFITM3, the sequence was optimized for bacterial expression:

```
ATGAACCACACGGTCCAGACGTTTTTCTCGCCGGTCAACTCGGGCCAGCCGCCGA  
ACTACGAAATGCTGAAGGAAGAACACGAAGTGGCCGTGCTGGGTGCACCGCATA  
ACCCGGCACC GCCGACCTCAACGGTTATTCATATCCGTAGCGAAACCTCTGTCC  
CGGATCACGTGGTTTTGTCGCTGTTTAACACGCTGTTTCATGAATCCGTGCTGT  
CTGGGCTTTATTGCGTTCGCCTATAGTGTTAAATCCCGTGATCGCAAGATGGT  
CGGCGACGTGACCGGTGCACAGGCTTACGCGTCTACGGCTAAATGCCTGAATA  
TTTGGGCACTGATCCTGGGTATTCTGATGACGATTCTGCTGATTGTGATTCC  
GGTCCTGATTTTTCAAGCGTATGGCTAA
```

Plasmid Construct Design:

Sequence optimized IFITM3 was cloned by Gibson assembly into a PET 28c plasmid immediately 3' to a HIS-Sumo sequence, designed by Christopher D. Lima⁷⁹. For Cys mutant constructs, QuikChange Lightning, and QuikChange Multi Site-Directed Mutagenesis kits (Agilent) were used to mutate the needed number of cysteines to alanines.

Induction and Enrichment of IFITM3

The Sumo-IFITM3 construct was transformed into the BL-21 LOBSTR cell line⁸⁰ containing the RIL plasmid (BL21-CodonPlus-RIL strain, Agilent) for increased copies of tRNA *argU* (AGA, AGG), *ileY* (AUA), *leuW* (CUA). Single colonies were grown overnight in LB media containing kanomycin (50 µg / mL) and chloramphenicol (25 µg / mL). The

following day, overnight cultures were diluted 1:30 in 1 L LB with kanomycin, and incubated at 37 °C to an O.D. of 0.6 the culture was then transferred to 18 °C, induced with 0.5 μM IPTG, and incubated overnight for 16 – 20 h. The following day, aliquots of 500 mL of cultures were spun down at 4,000 g for 15 min, and the bacterial pellet snap frozen in liquid nitrogen for future use. On the day of purification, a 500 mL bacterial pellet was thawed on ice, and resuspended in 40 mL **Buffer A** (25 mM HEPES, 100 mM KCl, pH 7) with 2% w/v Triton-X 100, and 1x protease inhibitor mixture (Roche). If the purified protein contained any cysteines, 1 mM β-mercaptoethanol (Sigma) was added. The resuspended pellet was incubated at room temperature (RT) with 10 mg lysozyme, then sonicated (Sonic Dismembrator Model 500, Fisher Scientific) for one minute (30% power, 1 second on, 1 second off). The sample was inverted several times to ensure mixture of lysate. Sonication was repeated twice more to ensure complete lysis. After sonication, the sample was diluted 2.5 fold in Buffer A without Triton-X 100 (final volume 100 mL, 0.8% Triton-X 100), and spun down at 40,000 g for 45 min (Beckman Coulter Optima XL-100K Ultracentrifuge).

During centrifugation, 12 mL of resuspended cobalt beads ('Talon metal affinity resin' Clontech) were washed 1x with water, and 2x with Buffer A. Post spin, the supernatant was collected and the cobalt beads added for two hours with nutation at 4 °C. The beads were then collected in an XK16/20 Column (Akta), and eluted using an AKTAFPLC chromatography system. It is during this stage that the detergent is switched from Triton-X-100 to 1% octyl glucoside (Anatrace). Using a two pump protocol, the beads were treated stepwise with varying ratios of two different buffers: **Buffer B** (25 mM HEPES, 100 mM KCl, 1% octyl glucoside, pH 7), and **Buffer B-imid**,

identical to Buffer B but containing 400 mM imidazole. If a construct with a cysteine was present, both buffers contained 1 mM neutralized TCEP (Thermo). BME contains a thiol, which interferes with the future step of coupling the palmitate. The beads were washed with 20 mL buffer B, then 20 mL of 90% Buffer B, 10% Buffer B-imid. Finally, the protein was eluted with 20 mL Buffer B-imid, and collected in two mL fractions. After the elution, fractions corresponding with the peak of the protein were incubated overnight with nutation and ULP1 (1 mM TCEP was added if apoIFITM3 was being purified), and analyzed the following day by SDS-PAGE. After cleavage of the SUMO domain was confirmed, the appropriate fractions were collected and mixed, and 2 mL fractions snap frozen in a dry-ice ethanol bath. *Note: Reducing agents such as TCEP or DTT are necessary for ULP1 activity.* If the sample did not require alkylation with maleimide-palmitate (i.e. apoIFITM3), then the SUMO domain was separated from the native IFITM3 by size exclusion chromatography (SEC) in Buffer B (10/300 GL, AKTA). In our hands, the SUMO domain consistently elutes after the IFITM3, making size exclusion a useful method to both remove background proteins as well as the enrichment tag.

Maleimide-Palmitate Synthesis

Synthesis by Rafal Wiewiora. Protocol from J. Med. Chem., 2009, 52, 7410-7420.

A round bottom flask was charged with 0.68 g of triphenylphosphine (2.57mmol, 0.9 eq.) and 17.5 ml of tetrahydrofuran. The flask was placed under argon and cooled to -78 °C. 1.18 ml of the 40% solution of diethyl azodicarboxylate in toluene (2.57 mmol, 0.9 eq.) were added over a period of 3 minutes. The resulting mixture was stirred for 5 minutes, after which a solution of 0.7 g of hexadecan-1-ol (2.87 mmol, 1 eq.) in a

minimal amount of THF (prepared in an argon purged vial) was added over a period of 1 minute. The resulting solution was stirred for 5 minutes. The flask's septum was then removed under the protection of an argon curtain and 0.125 g of neopentyl alcohol (1.43 mmol, 0.5 eq.) and 0.25 g of maleimide (2.57 mmol, 0.9 eq.) were added as solids. The flask was closed again under argon and the reaction mixture was stirred for 5 minutes, after which the cooling bath was removed and the reaction stirred at room temperature for 16 hours, then at 40 °C for 2 hours. After full conversion was indicated by TLC, the solvent was evaporated in vacuo. The resulting solid was purified by silica flash chromatography (loading and elution in dichloromethane). N-1-hexadecylmaleimide was obtained after high vacuum drying (0.481 g, 52%). ¹H NMR (400 MHz, CDCl₃) δ ppm 0.88 (t, J=6.59 Hz, 3 H) 1.25 (br. s., 26 H) 1.53 - 1.60 (m, 2 H) 3.51 (t, J=7.23 Hz, 2 H) 6.68 (s, 2 H). ¹³C NMR (100 MHz, CDCl₃): δ ppm 14.09, 22.67, 26.73, 28.52, 29.11, 29.34, 29.46, 29.53, 29.64, 31.90, 37.93, 134.00, 170.87. Reference: J. Med. Chem., 2009, 52, 7410-7420.

Maleimide-Palmitate Labeling of IFITM3

Labeling was completed after cleavage of the His-SUMO-IFITM3 construct with ULP1 protease. By doing so before the size exclusion, excess mal-palm is removed in addition to the SUMO domain and background proteins. Cleaved rIFITM3 is incubated with 1 mM TCEP (neutralized) and 0.5 mM Maleimide-Palmitate (stock solution- 10 mM in DMSO) for 2 hours at 15 °C with shaking. Temperature control is either by incubation in a bacterial incubation shaker while shaking at 100 rpm, or in a cold room on an Eppendorf Thermomixer heated to 15 °C. After labeling, the sample is spun down for 10 min at 20,000 x g and separated by size exclusion chromatography.

Confirmation of rIFITM3 maleimide palmitate labeling through MALDI-TOF.

MALDI –TOF mass spectrometry was of rIFITM3 constructs with generous help of the laboratory of Dr. Brian Chait at Rockefeller University. IFITM3 was prepared for MALDI-TOF analysis using the ultra thin layer method⁸¹. Briefly, first a MALDI sample plate was prepared with a thin layer of saturated 4-HCCA (Sigma) prior to use (4-HCCA plates will last over a year when stored properly). In preparation for sample analysis, (1) Eppendorf tubes were washed by vortexing with acetonitrile for several seconds and thoroughly dried. (2) A saturated solution of 4-HCCA was prepared by resuspending a dried sample of recrystallized 4-HCCA in a solution of formic acid, water, isopropanol (FWI) at ratios of 3:1:2 : the dried sample was resuspended in 100 μ L isopropanol, and rigorously vortexed for 2 minutes. 150 μ L formic acid was then added, and the solution vortexed rigorously again. Finally, 50 μ L water was added, and vortexed a final time. The solution was then centrifuged for 6 min at 14,000 rpm, and the soluble fraction carefully decanted with a pipette.

Samples of rIFITM3 were diluted 1/10 in 4-HCCA solution in an acetonitrile cleaned tube. The sample was then spotted onto the MALDI sample plate, and vacuumed off once a precipitate was seen to form. The spotted sample was then washed 2x with chilled 0.1% TFA in water, and loaded within half an hour into the mass spectrometer (Spiral TOF JMS-S3000, JEOL). Samples were analyzed at a late pulse rate of 500 Hz, at 31-33 % intensity, with a 750 ns lag time between laser pulse and sample capture.

Chapter 5: Production and anti-viral activity of IFITM3 proteoliposomes.

To explore the function of IFITM3 during viral fusion, it is necessary to use an appropriate lipid environment. Membrane proteins are purified using a variety of amphipathic detergents that enable solubilization by micelles containing hydrophobic interiors⁸². In contrast, viral fusion occurs at phospholipid bilayers, which vary considerably from detergents in structure, heterogeneity⁸³, and stabilizing properties⁸⁴. To incorporate rIFITM3 into the phospholipid bilayer, it is necessary to (1) generate the lipid bilayer, (2) incorporate the protein, and (3) remove the detergent that could alter the membrane properties in future experiments.

1) Lipid-bilayer formation through liposomes.

A well-established model for investigating membrane proteins in lipid bilayers is the liposome. A soluble, single-lamellar spherical bilayer, liposomes can be generated from a wide range of lipid compositions and sizes (Table 2). Protein containing liposomes (proteoliposomes) have been used extensively to characterize membrane proteins⁸⁵ and protein mediated membrane fusion⁸⁶, and provide an excellent model for viral-fusion inhibition through bulk fusion assays.

Table 2. Sizes and formation techniques for unilamellar liposomes.

PC: Phosphatidylcholine. PS: Phosphatidylserine. PE: phosphatidylethanolamine.

Class of Liposome	Diameter (nm)	Formation Technique	Example Lipid Compositions
Small Unilamellar Vesicle (SUV)	20 - 100	Sonication	PC/PS/PE ⁸⁷
Large Unilamellar Vesicle (LUV)	100 – 1000	Extrusion, Rapid Dilution ⁸⁵	PC/PS ⁸⁸ , PC/PE ⁸⁹ , PC/Chol ⁹⁰
Giant Unilamellar Vesicle (GUV)	1000 +	Electro swelling, Spontaneous swelling ⁸⁸	PC, PC/Chol ⁹¹

For liposome generation in the range of 100 – 1000 nm (large unilamellar vesicle - LUV), there are two commonly used techniques – extrusion, and rapid dilution⁸⁵. For extrusion, multi-lamellar liposomes are formed by freeze thawing a detergent free lipid solution, and then passed through a filter membrane of defined size until unilamellar vesicles are formed. While membranes with pore sizes up to 400 nm diameter can be used⁹², LUV preformation complicates protein incorporation into the lumen. We therefore used rapid dilution, which relies on the resuspension of lipids in detergent containing buffer (1% w/v octyl glucoside (OG)) then diluting below the critical micelle concentration⁸⁵ (CMC). The CMC is the concentration below which the detergent is no longer stable in a micellar structure, leading to its disassembly and inability to solubilize hydrophilic domains of lipids or proteins (Fig. 22A). The result of this rapid dilution is the spontaneous formation of unilamellar lipid vesicles.

Proper formation of LUV can be rapidly affirmed through dynamic light scattering (DLS), which determines the particle diameter via fluctuations in light scattering and the subsequent autocorrelation curve⁹³ (Fig. 22B). Under our formation conditions and lipid composition, we consistently observe an average diameter of 80 nm (Fig. 22C). To measure the efficiency of liposome formation, a total-phosphate assay⁹⁴ is used to determine phospholipid concentrations after dialysis. We observe similar values for all conditions, in the range of 0.5 mM, indicating a lipid retention of ~60% (data not shown).

2) Incorporation of IFITM3 into the proteoliposomes

In contrast to the extrusion method, a key advantage to liposome formation through rapid dilution is the ability to introduce proteins during the formation of the liposome itself⁸⁶. Rapid dilution disrupts the detergent micelle suspension of the both

the lipid and recombinant protein, leading liposome formation and protein incorporation into the lipid bilayer, with an equal likelihood of incorporation into the lumen of the LUV. This is critical for investigating potential IFITM3-virus interactions, the physiological topology of which is IFITM3 is on one side the membrane, and the viral particle on the other^{17,26}.

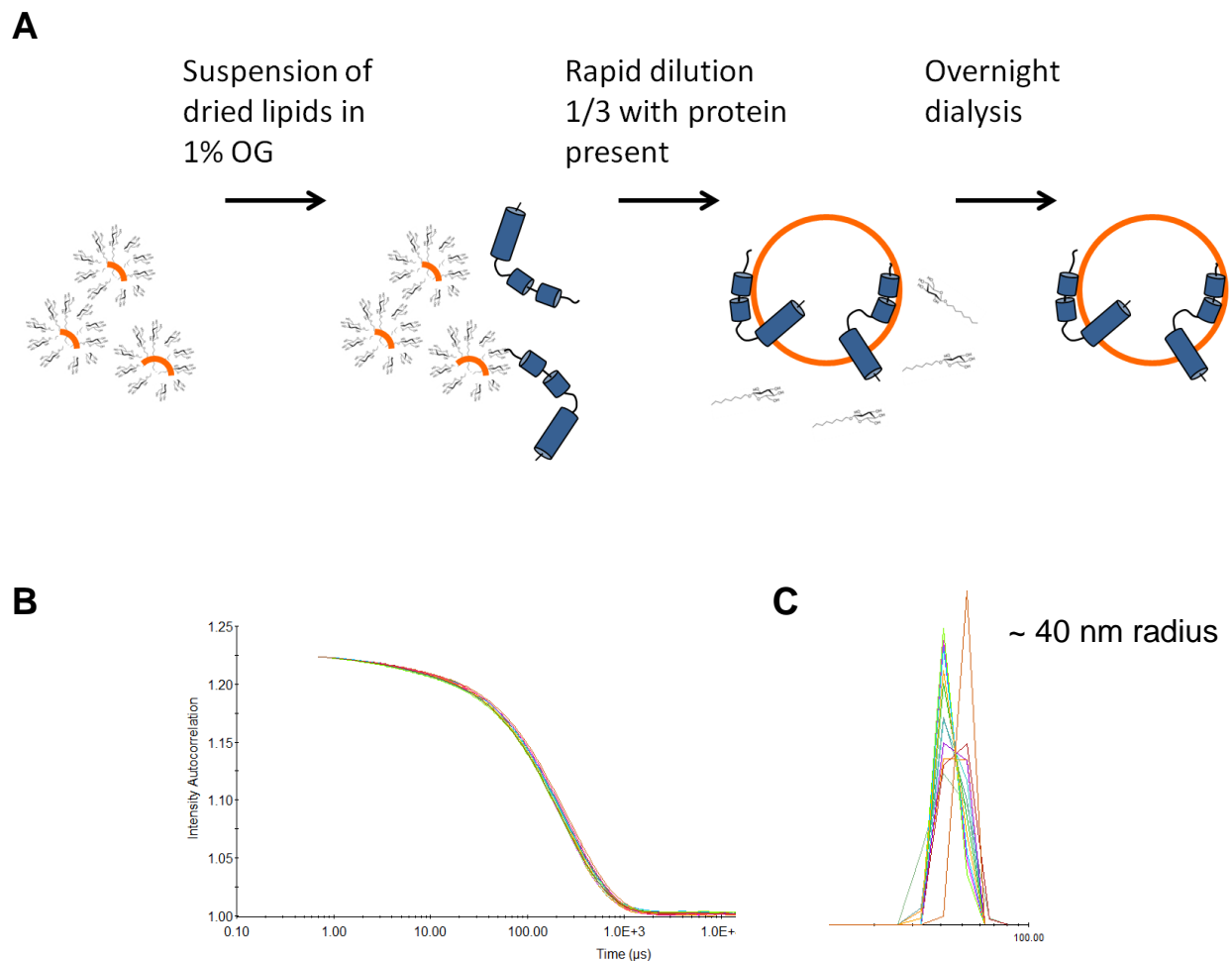


Figure 22. Rapid dilution of detergent solubilized lipid-protein leads to formation of unilamellar proteoliposomes. (A) The rapid dilution below the CMC of octyl glucoside drives disassembly of the detergent micelle, leading to formation of unilamellar LUVs. (B) DLS autocorrelation curves of empty LUVs, proteoliposomes with rIFITM3 or VAMP2 show similar trends. (C) Derivatization of LUV diameter from autocorrelation curves shows a consistent LUV radius of 40 nm.

3) Dialysis of detergent

With the rapid dilution method, the detergent is diluted to a concentration below the CMC (for OG it is approximately 0.6% w/v⁸⁶) and is no longer in micellar form. While the detergent no longer solubilizes rIFITM3 (forcing it into the lipid bilayer), it is possible that detergent molecules will intercalate into the membrane, potentially altering the biophysical properties of the lipid environment. The final proteoliposomes solution is therefore dialyzed overnight in Buffer A without any detergent. After dialysis, the liposomes were analyzed for size, and total phospholipid content.

To confirm the incorporation of the protein into the proteoliposomes, samples were centrifuged in a Histodenz density gradient (an alternative to sucrose)⁹⁵, and fractions collected and analyzed by SDS-PAGE. For all protein constructs we observe that the majority of the protein distributes to the top fraction of the gradient, reflecting its association with the less dense liposome (Fig 23A,B). To enhance detection, the top fraction was further concentrated by acetone precipitation. SDS-PAGE shows similar signal intensity, further confirming similar levels of incorporation (Fig. 23C).

As we observed the majority of the rIFITM3 is associated with the proteoliposome, we sought to estimate how many proteins are present in each membrane leaflet. Values were calculated based off of reported volumes of cholesterol⁹⁶ and PC⁹⁷, as well as depth of lipid bilayers⁹⁸. Both starting concentration and measured phospholipid concentration (0.5 mM) were determined (calculation in methods section). We estimate a final number of 600-1000 IFITM3 molecules per liposome (Fig. 24).

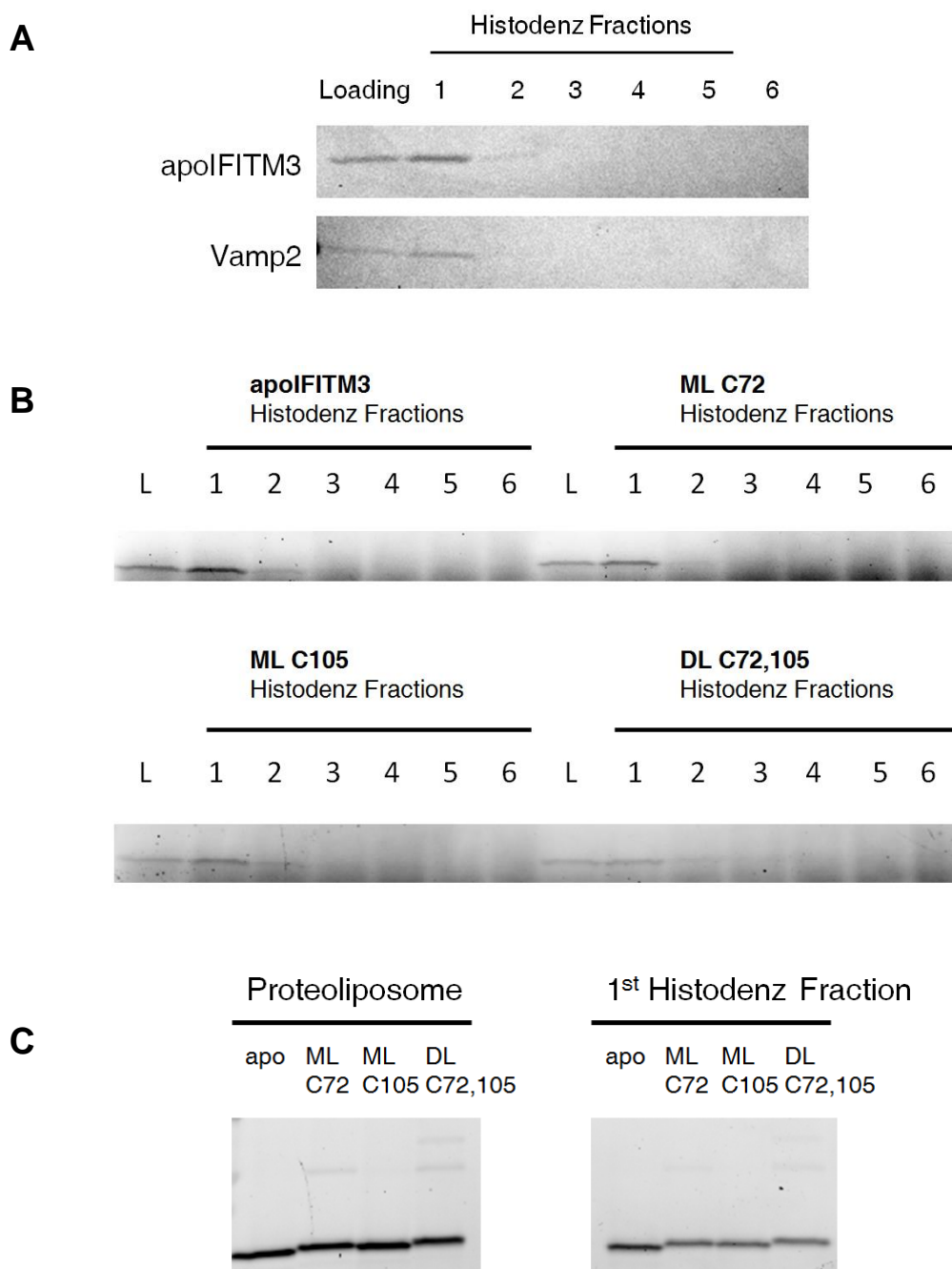
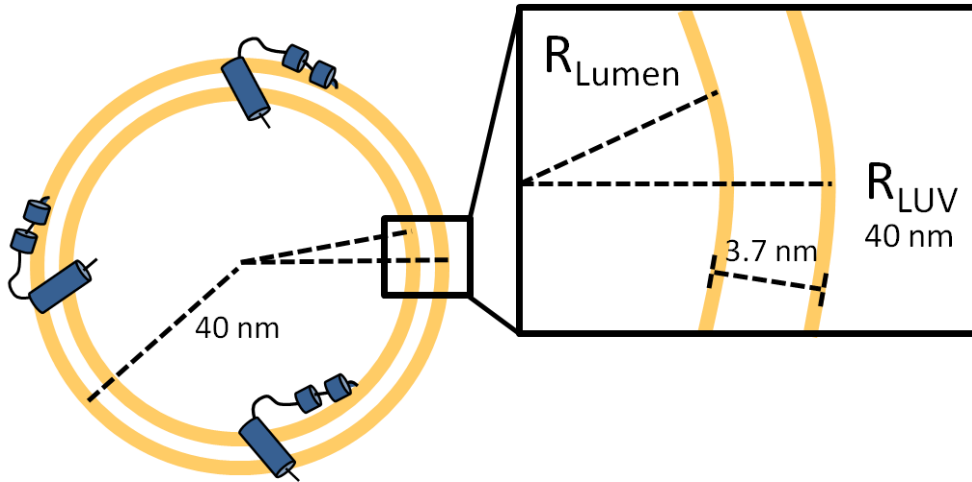


Figure 23. Protein incorporation into the proteoliposome. (A) Histodenz density gradient (0, 30%, 40%, w/v) was spun down at 50,000 rpm with proteoliposome containing apoIFITM3 or VAMP2 (protein: lipid 1:1000) and analyzed by SDS PAGE. (B) Similar gradient analysis was done on all IFITM3 constructs. (C) Improved signal was obtained by acetone precipitation of 250 μ L proteoliposomes, and 150 μ L first fraction of histodenz gradient. Lipid induced mass shift is observed for ML and DL constructs.

A**B**

IFITM3 Concentration (Protein: lipid ratio)	IFITM3 Per LUV at starting concentration	IFITM3 Per Bilayer Leaflet	IFITM3 Per LUV at final concentration (0.62 mM)	IFITM3 Per Bilayer Leaflet
1 μ M (1:1000)	600	300	1000	500
0.2 μ M (1:5000)	125	60	200	100

Figure 24. Calculation of IFITM3 concentration per LUV and lipid bilayer leaflet.

(A) Schematic of LUV radius and membrane thickness. Total number of LUV obtained by dividing total membrane volume (at 1 mM) by bilayer volume (see methods). (B) Histodenz gradients (Fig. 23) suggest the majority of the protein is incorporated into LUVs. Dividing the total number of IFITM3 proteins by the number of LUVs yields the concentration of IFITM3 / LUV.

Bulk Viral Fusion Assay

The formation of the proteoliposomes is a critical step towards viral fusion assays, either in bulk solubilized form, or as an intermediate step towards supported lipid bilayers⁹⁹. To detect the interaction of the virus and the liposome, previous work in the literature utilizes self-quenching fluorophores incorporated into the viral envelope^{27,100,101}. Catalyzed by the acidification of the buffer solution, hemi-fusion, or fusion of the viral envelope with endosome or liposome membrane (reflecting outer-leaflet mixing, or fusion pore formation, respectively) leads to diffusion of the fluorophore, dequenching and increased fluorescent signal (Fig 25).

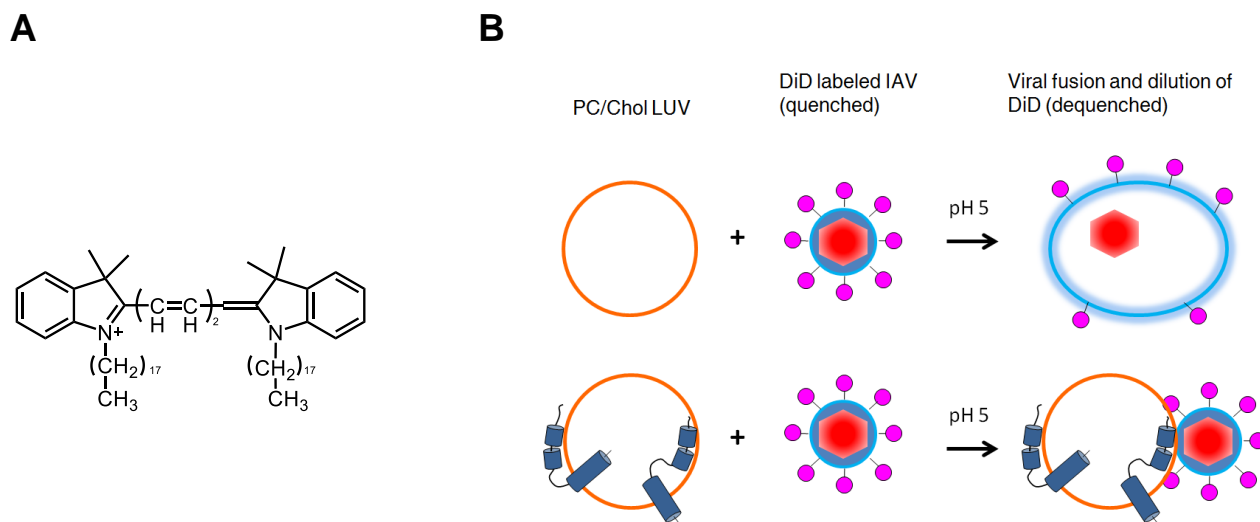


Figure 25. DiD labeled IAV enables detection of envelope lipid mixing.

(A) Structure of DiD, a self quenching fluorophores with high affinity for membranes. (B) Schematic for viral fusion assay. *Top*: Self quenching DiD increases in fluorescent intensity upon diffusion into larger membrane area, indicating viral fusion (or hemifusion, not shown) has occurred. *Bottom*: bulk fusion assays provide a first step towards testing whether IFITM3 can independently interfere with the ability of viruses to fuse with target membranes.

To support the comparison of our results to previous work in the literature, LUVs of similar lipid composition^{102,103} were used, with molar ratios of 8:2:0.1 phosphatidylcholine (PC), cholesterol (Chol), hemagglutinin receptor ligand disialo-ganglioside (GD1a), respectively. As expected, we observed an increase in signal of DiD dequenching with GD1a (Fig. 26B). Though previous work has indicated that the presence of cholesterol improves viral fusion⁹⁰, under our conditions similar levels were observed when compared with PC and GD1a alone. In contrast, replacing Chol with phosphatidylethanolamine (PE), a phospholipid of conical shape¹⁰⁴ results in a higher DiD signal, confirming that the virus-liposome fusion properties are influenced by our choice in lipid composition.

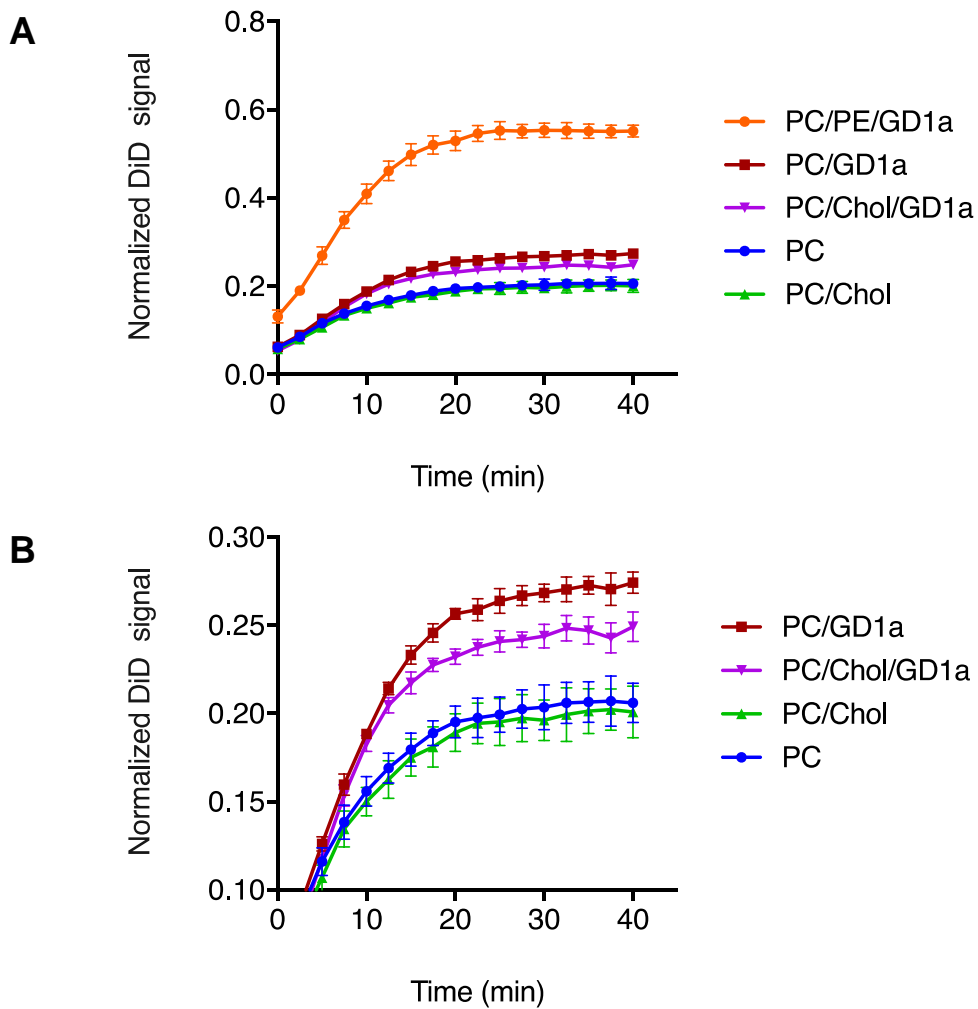


Figure 26. Fusion comparison of LUV lipid compositions. Fusion assays were conducted at 37 °C, and normalized to the max signal of DiD obtained after the addition of 1% Triton X-100. (A) LUVs were prepared from a combination of PC, Chol, PE, and GD1a, at identical total concentrations of 1 mM. (B) Same data as A, with PC/PE fusion data removed for improved resolution.

Since the temperature might also affect viral fusion and DiD dequenching, similar fusion conditions were compared at 25 °C and 37 °C (Fig. 27). LUV containing VAMP2, a SNARE membrane protein¹⁰⁵ of similar size to IFITM3 is used as a control for the impact of background proteins on viral fusion. While trends between the different liposome conditions were conserved, at 37 °C a stronger signal was observed that plateaued as early as 15 min into the reaction. In contrast, at 25 °C, DiD dequenching was continuous, and did not reach a max value even after 90 min. As 37 °C not only results in faster results that go to completion, but also reflects the physiologically relevant temperature, all further experiments were conducted under similar conditions.

To show that DiD dequenching was not an artifact of the model, we tested the functional conditions of the DiD labeled IAV (Fig. 28). IAV fuses with the lipid bilayer of the late endosome at a pH below 5.5¹⁰⁶, leading to fusion pore formation and content release. Fusion should therefore only occur in the presence of an *intact* viral particle, LUV, and acidic buffer conditions (pH 5). When comparing IAV alone at pH 5, or IAV with LUV at pH 7, neither show a significant increase in signal in comparison to IAV with LUV, at pH 5. This indicates that minimal DiD dequenching occurs due to acidification of the buffer or spontaneous transfer of DiD from the viral membrane to the LUV. Previous work by Carr et al.¹⁰⁷ showed that IAV fusion can be disrupted by premature unfolding of the hemagglutinin (HA), caused by either heating at 62 °C for 30 min or premature acidification at pH 5. Indeed, both conditions disrupted viral fusion in our assay, supporting our model that DiD dequenching is mediated by HA catalyzed lipid mixing (fusion/hemifusion).

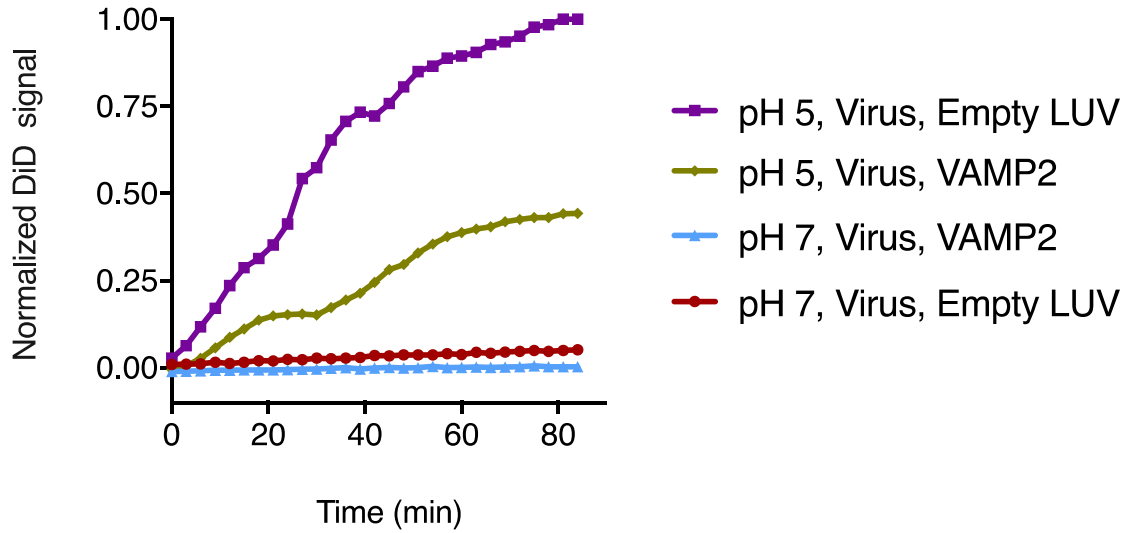
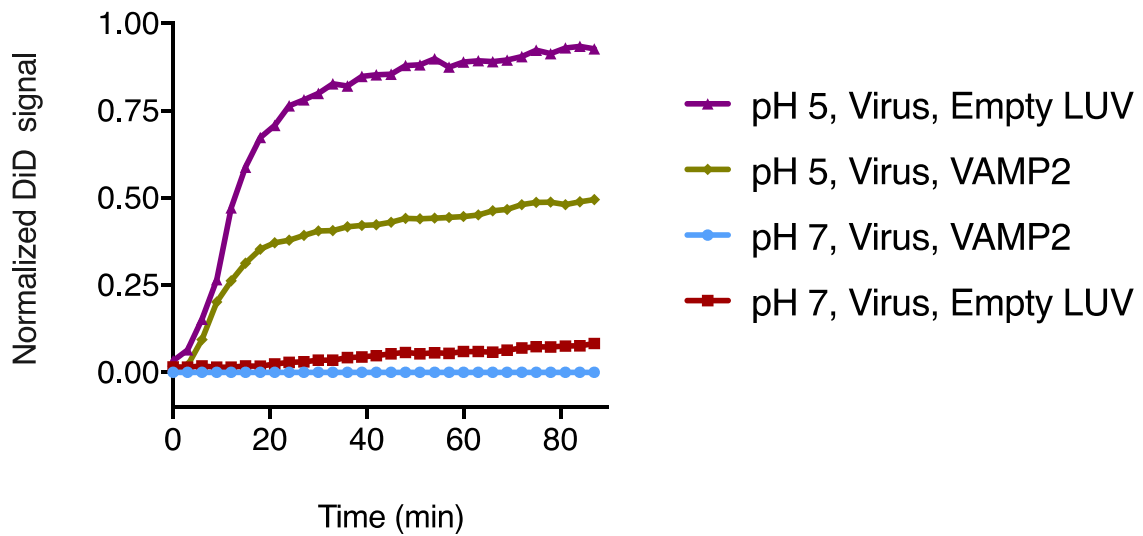
A**B**

Figure 27. Temperature of IAV fusion affects rate, and signal saturation. LUV and VAMP2 proteoliposomes were incubated with DiD labeled virus at pH 5, at 25 °C (A) and 37°C (B). Protein:lipid ratios for all constructs were 1:1000.

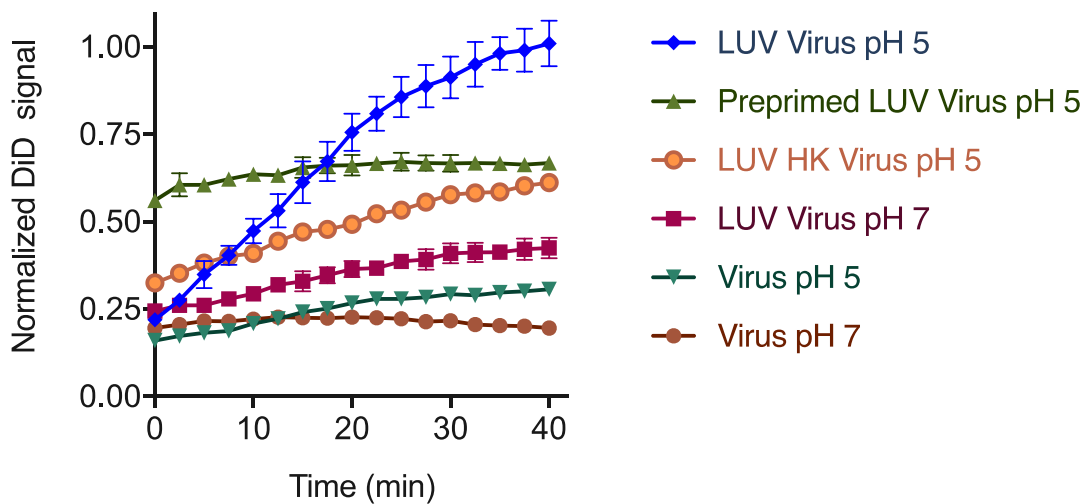


Figure 28. Viral fusion with LUV is pH, HA dependent. . Minimal signal was observed under similar conditions at pH 7, or in the absence of LUV. To confirm that HA integrity was required for fusion, IAV was incubated either at 62 °C for 30 min (HK), or incubated at pH 5 at 37 °C (preprimed). Both conditions compromise fusion, and DiD dequenching.

Having characterized the LUV and viral parameters of our model, we proceeded to fusion assays with LUVs containing rIFITM3. Starting with protein concentrations similar to other LUV fusion models we titrated the amount of VAMP2 (Fig. 29A) and apoIFITM3 (Fig. 29B) to determine the dynamic range and saturating concentrations. Both exhibited a decreasing DiD fluorescence signal at lower protein concentrations, indicating non-saturating conditions in the protein:lipid range of 1:1000-1:4,000.

We first compared viral fusion with proteoliposomes of VAMP2 and apoIFITM3 at protein:lipid ratios of 1:1000 to facilitate detection and maximize signal (Fig. 30). Though our data indicates apoIFITM3 is a non-physiologically occurring phenotype (Fig. 17C) it provides a first step towards understanding whether S-fatty acylation is critical for IFITM3 function (in contrast to trafficking or turnover). It also provides a critical control

for modified lipidated constructs. Viral fusion with LUV containing VAMP2 exhibited DiD dequenching equivalent to roughly 80% of the empty LUV. Due to high concentrations of LUV and virus, we hypothesize this is due to background lipid mixing mitigated by VAMP2 steric hindrance. ApoIFITM3 showed a greater inhibition of DiD dequenching with max levels reaching approximately 65%, providing first evidence of a direct interference with viral fusion. Though promising, a helpful control is the loss of function through the mutation of additional sites. Earlier work by John et al.¹⁰ demonstrated several point mutations that disrupt the anti-viral activity of IFITM3. Two of these (R85A, T99A) do not disrupt the addition of PTMs, but rather interfere with the native amino-acid backbone. We therefore generated apoIFITM3-R85A as a control mutant. Unexpectedly we found it showed similar levels of inhibition to that of the apo-WT. As this mutation might be non-disruptive under the conditions of the fusion model, we are continuing our efforts towards functional mutants, with additional point mutants as well as larger, more disruptive modifications.

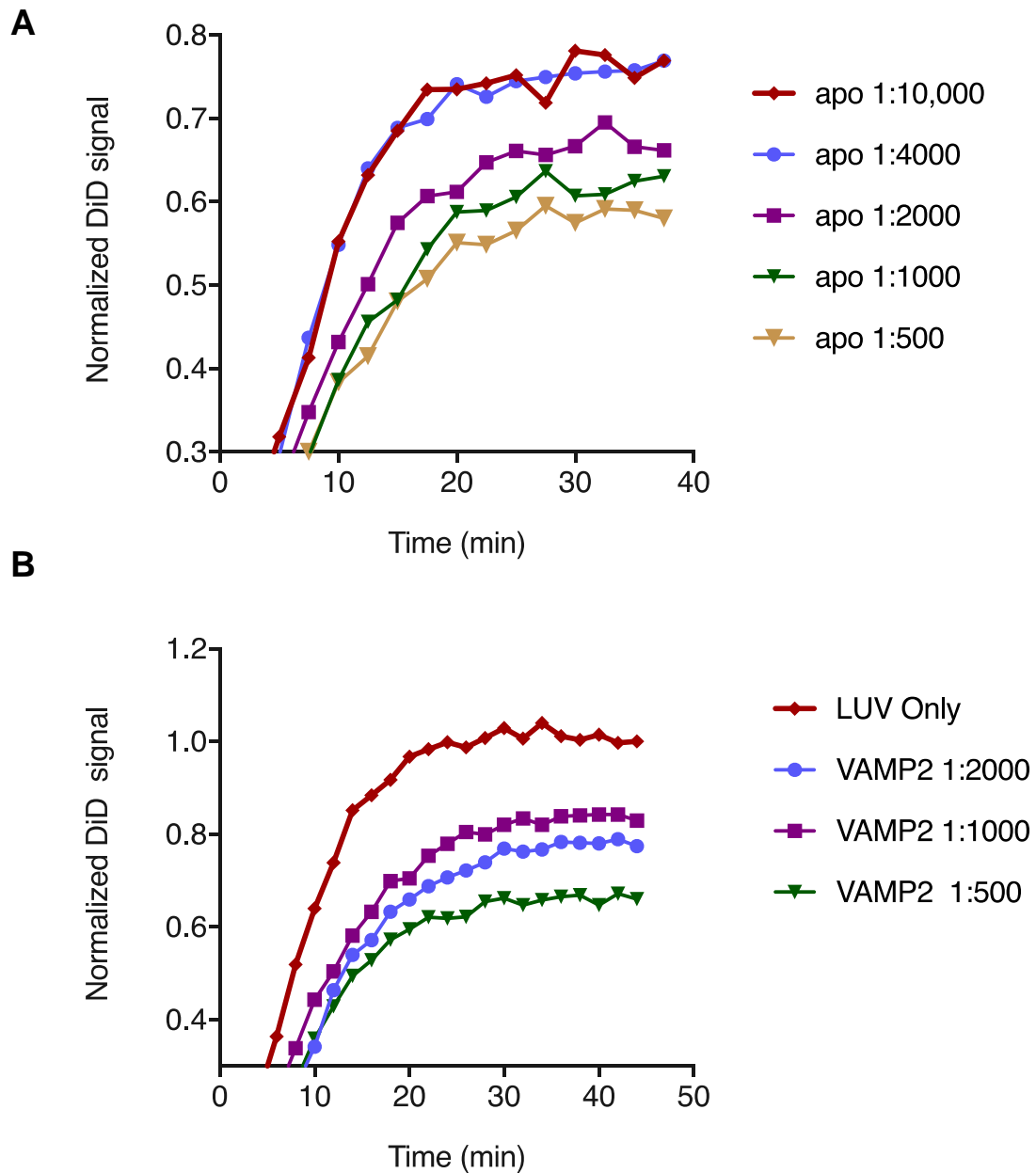


Figure 29. Titration of VAMP2 and apoIFITM3 confirms dynamic range of proteoliposome fusion assay. Both VAMP2 (A) and apoIFITM3 (B) were titrated into proteoliposomes at the reported ratios, and the DiD signal normalized to the max DiD value for empty LUV value.

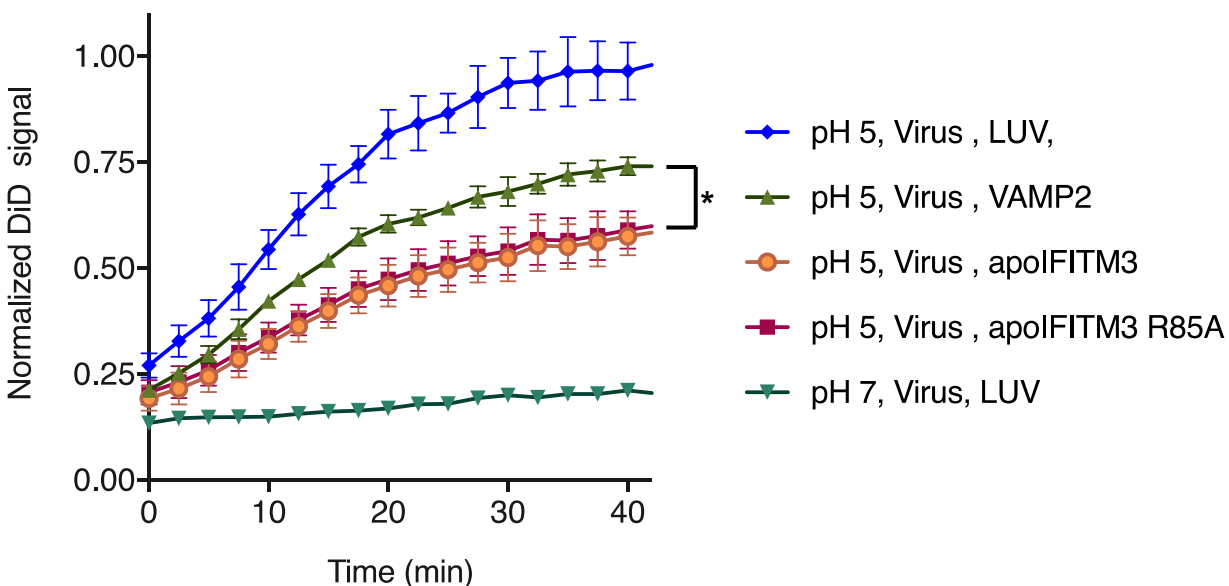


Figure 30. ApoFITM3 inhibits viral lipid mixing to a greater degree than VAMP2. Proteoliposomes at a protein:lipid ratio of 1:1000 were incubated with DiD labeled virus at pH 5, and normalized to the max DiD value of empty LUVs. ApoFITM3 (yellow) and R85A (red) show similar levels of activity. Representative of duplicate experiments. Error bar represents SD.

Having observed a decrease in DiD dequenching with apoFITM3 proteoliposomes, we proceeded to compare IAV fusion with proteoliposomes containing the various lipidated constructs described in chapter 4 (Fig. 20). To test whether the constructs showed similar activity levels, we titrated the mono-lipidated constructs over a protein:lipid range of 1:1000–1:20,000 (Fig. 31). All constructs showed a concentration dependent increase in inhibition of DiD dequenching, while C105A appeared to inhibit DiD more effectively than apoFITM3 (Fig. 31A). To facilitate experimental design, and inclusion of the double-labeled C72,105 construct (protein instability resulted in very low protein purification), a protein:lipid ratios of 1:5000 was chosen for subsequent experiments.

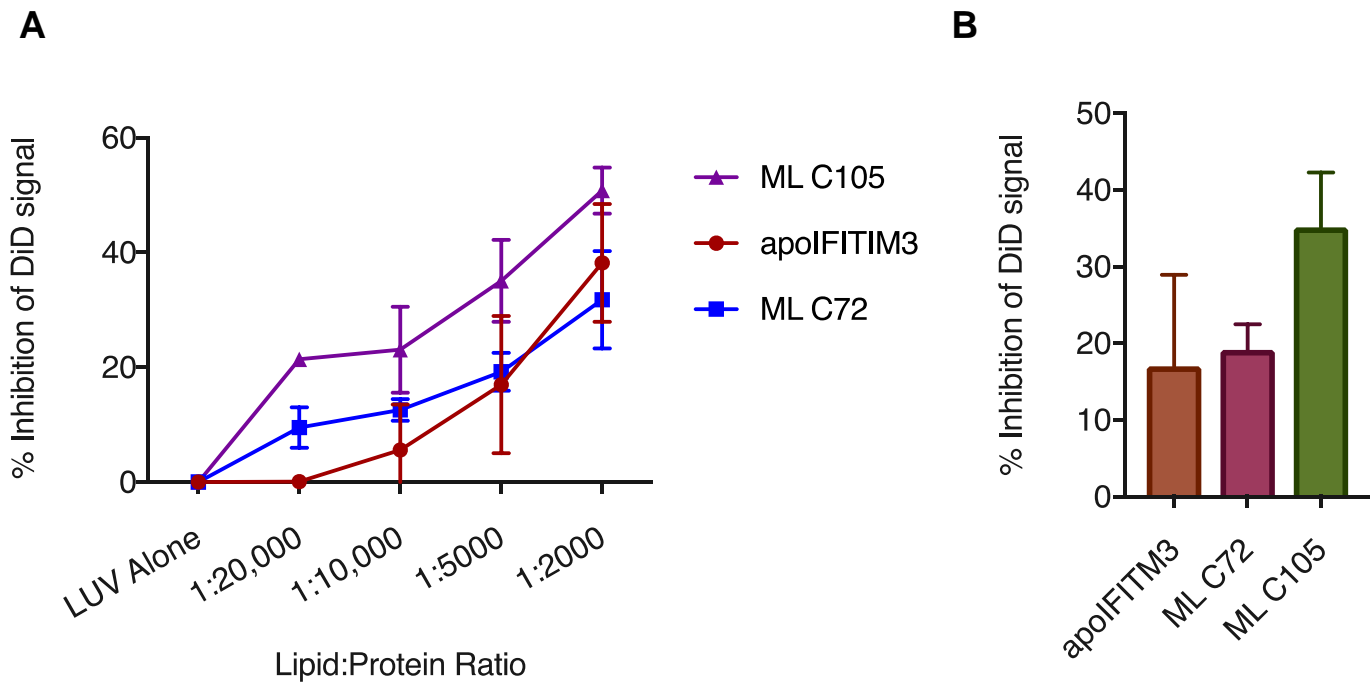


Figure 31. All constructs of rIFITM3 inhibit viral lipid mixing. (A) Decreasing ratios of protein:lipid (higher protein concentration) increase efficacy of inhibition of mono-lipidated constructs (ML Cys 72, ML Cys 105). Representative of duplicate experiments. Error bars represent SD. (B) % DiD inhibition (1-max fusion value) at protein:lipid ratio of 1:5000.

Biological replicates indicate that the apoIFITM3 proteoliposome inhibits DiD dequenching in comparison to VAMP2 or empty LUVs (Fig. 32). ML-C72 does not alter IFITM3 inhibition activity, while ML-C105 shows a significant increase of 50% (+/- 29% SD). Surprisingly the double lipidated construct shows a smaller improvement, inhibiting DiD dequenching by 30% (+/- 22%- SD). This data indicates that rIFITM3 independently alters some aspect of the fusion environment that interferes with hemifusion/fusion and DiD dequenching. Furthermore, lipidated isoforms have Cys-specific effects on rIFITM3 mediated inhibition, with ML-C105 increasing rIFITM3 activity the most. One interpretation is that the S-fatty acylation of C72, previously shown to be critical for

IFITM3 anti-viral activity (Fig. 17) plays a role in IFITM3 trafficking and regulation, while S-fatty acylated C105 augments IFITM3 function. While this model holds promise, more work is required to correlate the data with *in vitro* work, such as introduction of rIFITM3 isoforms to tissue culture, or better mimics of the late endosome membrane.

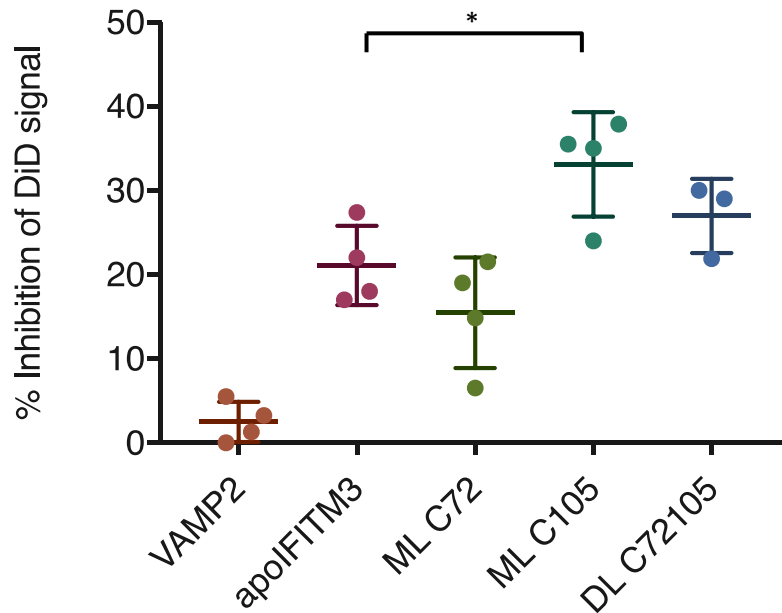


Figure 32. Cys specific lipidation of rIFITM3 alters inhibition of DiD dequenching. Pooled data of four separate fusion assays comparing apoIFITM3 with mono and dual-lipidated rIFITM3 constructs. Protein:lipid ratio for all experiments 1:5000. Error represents SD. $P < 0.05$ for unpaired, two-tailed t-test.

To test that the difference in inhibition between apoIFITM3 and ML-105 proteoliposomes is not due to residual mal-palm from the labeling and purification process, apoIFITM3 was purified a similar manner to ML-105. Comparison of apoIFITM3 with and without mal-Palm showed identical levels of inhibition of viral fusion (Fig. 33A). A drawback of the reconstituted bulk fusion assay is the stochastic incorporation of rIFITM3 into both sides of the liposome membrane. While this insures

the incorporation of rIFITM3 into the LUV lumen, it also results in virus-facing rIFITM3, which does not occur under physiological conditions (Fig. 4). To remove outer-leaflet rIFITM3, we incubated the proteoliposomes for 1 hour with chymotrypsin(Fig. 33B).

While we observed proteolysis of all constructs (Fig. 33C), we did not observe a change between the extent of inhibition between cleaved and non-cleaved samples. There are several possible interpretations: (1) the outer leaflet rIFITM3 does not play a role in viral fusion, with all anti-viral activity exerted by the luminal facing fraction. (2) The transmembrane domain of the outer-leaflet rIFITM3 contributes to anti-viral activity, and is retained after chymotrypsin treatment. (3) The cleaved rIFITM3 still adheres to the LUV membrane and exerts some activity during viral fusion. While this problem can be better addressed by generating a single-orientation topology, we are unaware of any techniques that can encapsulate a protein in a liposome, or supported bilayer, without relying on further proteolysis. Future options for fusion models are discussed in Chapter 6.

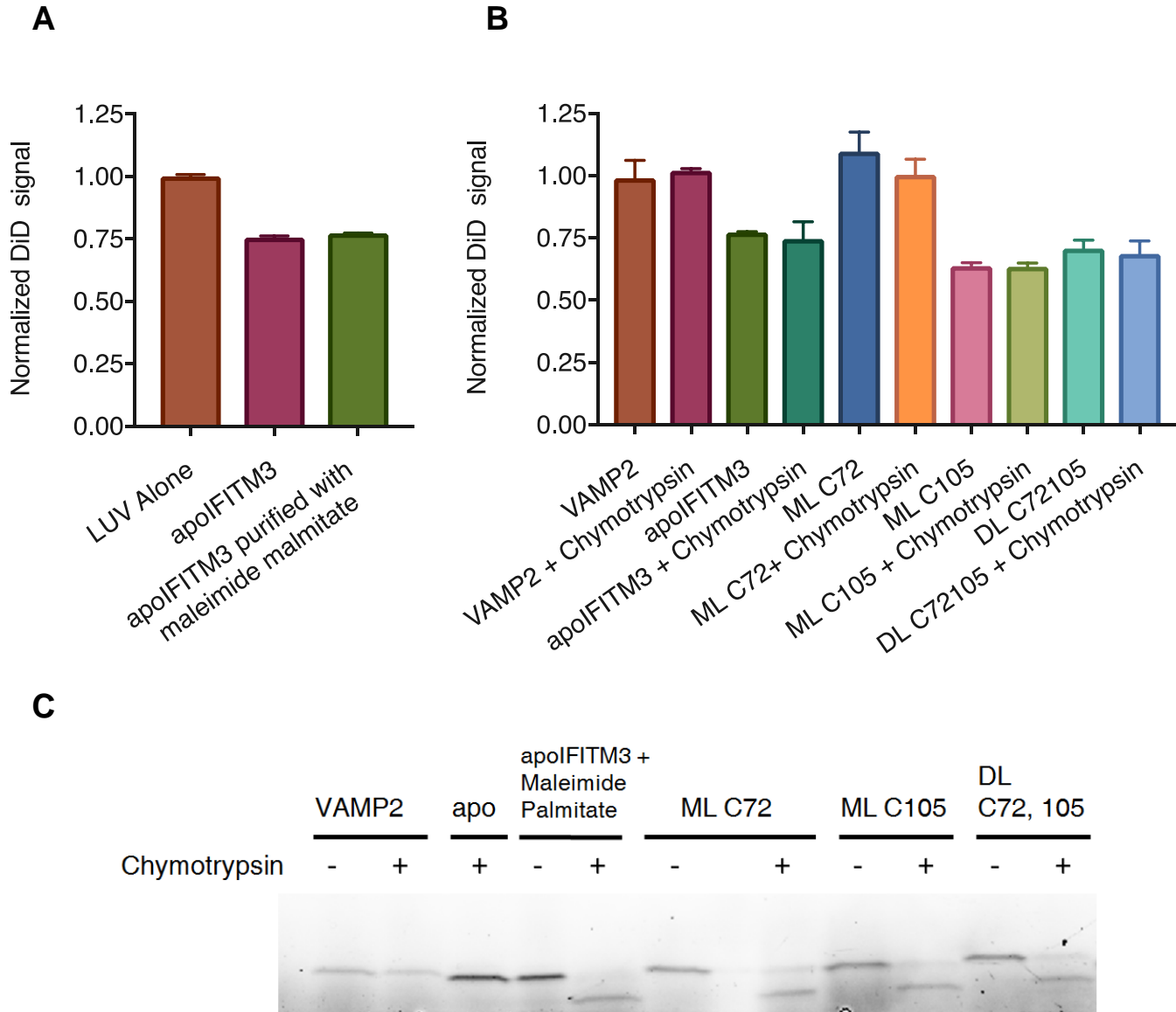


Figure 33. Residual mal-palm, chymotrypsin treatment does not alter proteoliposome fusion properties. (A) Purification of apoFITM3 under similar mal-palm labeling conditions as ML-C72/105 does not alter the % inhibition of DiD dequenching in viral-proteoliposome fusion assays. Protein:lipid 1:5000, (B) Proteoliposomes with or without chymotrypsin were incubated for 1 hr at 37 °C. After viral fusion assays, the max DiD value for each condition was normalized to the max value of LUV alone. (C) SDS-PAGE of proteoliposomes treated with chymotrypsin. Lower molecular weight bands are observed for degraded products.

Methods for Chapter 5:

Generation of proteoliposome through the rapid dilution method:

Modified from Weber et al. ⁸⁶. All chloroform solutions were stored in appropriate borosilicate glass with PTFE lined caps (VWR). Phosphatidylcholine and phosphatidylethanolamine, suspended in chloroform were purchased from Avanti lipids. 10 mg cholesterol (Sigma) was resuspended in 1 mL HPLC grade chloroform (Sigma), for a final concentration of 25.88 mM. GD1a (Sigma) was resuspended in a 1:2 methanol:chloroform solution, for a final concentration of 0.544 mM (mw 1882).

For a final total concentration of 1 mM lipid (cholesterol included), appropriate volumes of each lipid were added to a 13 x 100 mM glass vial, and dried under a gentle argon stream (a clear residue is observable from at the bottom of the vial). The sample was then placed under vacuum for at least 2 hours. The dried lipid was resuspended in 1/4 the final total volume by adding Buffer A containing 1% OG, followed by horizontal shaking (gentle agitation can also be used). Higher resuspension concentrations will result in an opaque solution. The resuspended lipid was then aliquoted to other glass vials according to the number of conditions planned. After the addition of protein (the volume of protein + lipid cannot exceed 1/3 final volume), the lipid-protein solutions were left at RT for several minutes, then rapidly diluted: on a table top vortex machine turned to a high setting, the glass vial was pressed down with one hand, while the other hand added 2-3x the volume of the solution, of buffer A *without* detergent (depending on starting volume). This dilutes the OG below the CMC of 0.5% (final 0.25 – 0.3 %), driving the formation of liposomes.

To dialyze out the remainder detergent, the entire liposome solution was added to pre-primed Slide-A-Lyzer MINI Dialysis wells (Thermo, 10k MWCO). Different sized wells were used depending on the volume of the solution (0.5 mL wells for 4-500 μ L volumes, 3 mL wells for 1-2 mL volumes). The wells were then shaken horizontally at RT for 1 hr, followed by a buffer exchange and dialysis with horizontal shaking for 6 hr at 4 °C. Finally, an additional buffer exchange was done, and incubated overnight at 4 °C with horizontal shaking. The next day, the samples were transferred to Eppendorf tubes with a pipette, and used for the described assays. Samples were kept for a maximum 1 week at 4 °C.

DiD labeling of IAV

For DiD labeling of IAV, the protocol reported by Desai et al.²⁷ was used with minor modifications: 200 mg virus (Charles River, catalogue# 10100374, 2 mg/mL, thawed once and snap frozen in 50 μ L aliquots, in liquid nitrogen) was diluted in 300 μ L 50 mM sodium bicarbonate buffer (pH 9.0), and incubated with 13.2 μ L DiD (Thermo) for 90 min shaking at RT. During this period, a disposable sephadex column (PD MiniTrap G-25, GE) was washed 3x with buffer A. To remove excess DiD, the sample was then added to the column, followed by 100 μ L buffer A. The column was then transferred to a new 15 mL Falcon tub, and eluted with 1 mL of buffer A. The eluted virus was kept away from light and on ice until use.

For a higher concentration of viral particles, it is possible to pass them through the G-25 column while centrifuging at 300 x g (see product manual). Though this removes excess DiD, it does not switch to a more neutral buffer. Care should be given

to adjusting acidification volumes during fusion experiments. DiD labeled IAV was usually prepared fresh the day of a fusion experiment, and surplus kept at most 48 hrs for additional use.

Dynamic Light Scattering (DLS) for measuring proteoliposome diameter.

Proteoliposome size was confirmed using a Wyatt DynaPro DLS Detector II. DLS is particularly sensitive to background contaminants, so extra care should be given during sample preparation, such as using Eppendorf tubes with minimal air exposure. Buffer A prepared with LCMS water (Spectrum Chemical) was filtered with a 0.02 μm filter (Whatman). Online protocols recommend 0.1 – 0.2 μm filters, though background signal was observed with our reagents. In 1.5 mL Eppendorf tubes, 200 μL of filtered buffer A was aliquoted. 2 μL of the sample (1/100) was added to the tube, and inverted several times to mix. All samples were then centrifuged for 5 min at 20,000 x g at RT, and three, 60 μL aliquots made in a 384 flat well plate (Greiner). Each sample was measured 10 times, 10 seconds per measurement.

Phospholipid Quantification.

To determine the total lipid concentration, a total phosphate assay was generously provided by the Menon Lab at Weill Cornell⁹⁴. In 13 x 100 mm glass tubes, a standard was prepared from a 40 mM Na_2HPO_4 stock solution, of 0, 2, 5, 10, 20, 50, 80 nmol phosphate (Pi), with a final volume of 50 μL . 10 μL of each lipid samples were then added to additional tubes with 40 μL H_2O . 300 μL perchloric acid (HClO_4 , Sigma) was added to all conditions, and heated for 1 h at 145 °C. (marbles on the tubes prevent evaporation). The tubes were then removed from the heating block, 1 mL H_2O was

added, and the solution vortexed briefly to mix. Samples were then left to cool while preparing 12mg/mL molybdate tetrahydrate (6 mL Sigma) and 50 mg /mL ascorbic acid (6 mL, MP Biomedicals). 400 μ L of each was then added to each tube, and vortexed to mix. The tubes were then heated at 100 °C for 10 minutes (make sure the tubes are on the same heating block, as heating variation will skew results), and cooled again to RT. 200 μ L of the standards and samples were then aliquoted in duplicate to a 96 well plate, and their absorbance measured at 797 nm (minimal color variation will appear in the lower Pi concentrations and sample).

Theoretical Calculation of rIFITM3 particles / liposome.

For calculating the theoretical number of IFITM3 proteins per LUV, the membrane thickness was assumed to be 3.7 nm⁹⁸., and the volumes of cholesterol⁹⁶, and PC⁹⁷ to be 0.622 nm³ and 1.256 nm³ respectively. Assuming an equal lipid concentration on each leaflet of the bilayer:

$$1) \text{ Volume of lipid bilayer per LUV} = \frac{4}{3} \pi (R_{LUV}^3 - R_{Lumen}^3) = \frac{4}{3} \pi (40\text{nm}^3 - (40(47)\text{nm}^3)) = 67,723 \text{ nm}^3$$

$$2) \text{ Total number of LUV} = \text{Total volume of lipids} / \text{volume of lipid bilayer}$$

$$\text{Total volume of 1 mmole lipids} = 10^{-3} * 6.022 * 10^{23} (0.8 * 1.256 \text{ nm}^3 + 0.2 * 0.622 \text{ nm}^3) = 6.8 * 10^{20} \text{ nm}^3$$

$$\text{Total number of LUVs} = 6.8 * 10^{20} \text{ nm}^3 / 67,723 \text{ nm}^3 = 1.005 * 10^{16} = 1.667 \text{ nmole} \rightarrow 1.667 \text{ nM for 1 mM solution of lipids.}$$

$$3) \text{ Number of IFITM3 proteins / LUV} = [\text{IFITM3}] / [\text{Concentration LUV}]$$

$$\text{e.g. } 0.2 \mu\text{M IFITM3} / 1.667 \text{ nM LUV} = 120 \text{ IFITM3 proteins / LUV}$$

Fusion assay to measure DiD dequenching

For all fusion assays, a digital multi-pipettor was used to enable simultaneous acidification of multiple conditions. 40 μ L of LUV were added in triplicate to a 384 flat well plate (Greiner) with 20 μ L virus. After 5 minute incubation, the solution was acidified with 4 μ L of 50 mM, pH 4 sodium acetate (1/15 of starting volume, final pH 5.0). Conditions kept at pH 7 were adjusted with 4 μ L buffer A. Immediately after acidification, the plate was measured on a pre-heated BioTek Synergy Neo at 37 °C. Measurements were taken every 2:30 min, over a period of 40 min, at excitation/emission of 640/670. After each run, 2 μ L of 20% Triton-X 100 was added to all wells to completely solubilize the DiD and obtain a max signal for reference and normalization.

Data analysis of fusion data.

For data analysis, each time point was normalized to the max DiD signal in the well obtained after addition of Triton-X-100. Technical replicates were then averaged, and divided by the max value obtained for LUV alone. This results in a normalized DiD dequenching curve in reference to LUV max fusion.

Chymotrypsin proteolysis of outer leaflet rIFITM3

Buffer A (negative control) or chymotrypsin (Promega, 25 μ g resuspended in 50 μ L 50 mM NH_4CO_3 pH 8) was added to LUV samples at a rIFITM3:chymotrypsin ratio of 10:1, for 1hr at 37 °C. 20 μ L was then aliquoted for analysis by SDS-PAGE, and 80 μ L used for the fusion assay.

Chapter 6: Future directions for rIFITM3 assays

Our proteoliposome-viral fusion assay with rIFITM3 presents the first evidence that a potential mechanism of IFITM3 viral inhibition is by independently altering the fusion environment. To investigate the viral fusion mechanism further the current model needs to be improved, having been originally built off a variety of assays previously used in the literature (proteoliposome formation⁸⁶, lipid composition¹⁰³, viral labeling²⁷). This setup was initially to our advantage as it allowed us to compare our results to previous work, and provided a framework to build upon. To determine *how* IFITM3 might be altering the membrane environment though, we require new assays to detect content mixing and fusion pore formation, and a better mimic of the late endosome environment.

Content Mixing Assays:

A facile modification of viral envelopes, the self-quenching properties of DiD labeling provides a valuable tool for measuring viral fusion. But while DiD can indicate the initiation point of lipid mixing, it cannot be used to distinguish between hemi-fusion (the mixing between the *outer* leaflets of the opposing membranes) and formation of the complete fusion pore. This is critical in understanding the mechanism of IFITM3, which has been suggested to interfere with viral fusion and content delivery at the stage of hemi-fusion²⁷. To be able to distinguish between the two possible stages, future work will focus on improving our model to detect full fusion pore formation, and pursuant viral content delivery.

Measuring content delivery between two populations of liposomes has been previously reported, using fluorescent dequenching¹⁰⁸, or FRET^{109,110}. These assays are based on encapsulation of two reacting moieties, which is incompatible with our viral-LUV model. However, they provide an experimental framework and possible tools for future use. For viral content labeling, one reported method relies on passive diffusion across the viral membrane with self-quenching Sulforhodamine B¹⁰³. While the method has been used in single particle measurements, we have not been able to replicate these results in our bulk fusion assay due to background signal. An additional assay is the incorporation of fluorescent proteins and probes into the viral nucleocapsid^{27,111}. Though useful for microscopy-based tracking of content delivery, this approach is hindered by lacking a gain, or loss of signal.

To address these technical limitations, our future work will focus on exploring two possible mechanisms for content labeling of viral particles. Both rely on a change in fluorescent activity (loss or gain), but vary in our incorporation methodology.

1) *Incorporation of unnatural amino acid through amber suppression technology.*

Amber-codon suppression has proven an invaluable tool for incorporating unnaturally occurring (synthetic) amino acids (UAA) with functionalized moieties¹¹². This technique has been used extensively to introduce novel functionalities into proteins, including photo-activated capture based screens^{113,114}, and post-translational labeling of IFITM3¹¹⁵. Previous work by other labs has successfully incorporated synthetic amino acids into viral capsid^{116,117} and envelope¹¹⁸ proteins, suggesting UAA incorporation provides a powerful tool for the modification of the influenza nucleocapsid.

Our first step would be to optimize the incorporation of an unnatural UAA into the most abundant nucleocapsid protein M1 (which not exposed to the buffer solution). This UAA could contain either a trans-cyclooctene (TCO) that reacts with several tetrazine containing fluorophores¹¹⁵, a fluorescent molecule incorporated during viral particle assembly to be further quenched during exposure to the LUV lumen, or a nucleotide sequence disrupting FRET based signal as previously reported in the literature¹¹⁰.

2) Labeling of viral lumen through membrane permeable probes.

An appealing alternative to incorporating the chemical probe during particle assembly (requiring purification) is the labeling of intact viral particles. This is both more time effective, and simultaneously applicable to multiple viral samples, enabling strain, species, and clinical sample comparisons.

A technical difficulty of this model is the necessity of choosing a chemical probe that can (1) selectively permeate across the viral envelope, and (2) be retained within the interior. To address this we can utilize a membrane permeable trans-cyclooctene (TCO) or cyclooctyne derivative (BCN)¹¹⁹, coupled to an amine reactive NHS-Ester¹²⁰ or photo-coupled diazirine¹¹⁴ for retention within the viral capsid (Fig. 34A). Preliminary data indicates that a BCN-NHS-Ester can successfully label both envelope proteins as well as M1 (Fig. 34D). This provides first evidence that the TCO moiety can successfully transverse the viral membrane, and label capsid proteins.

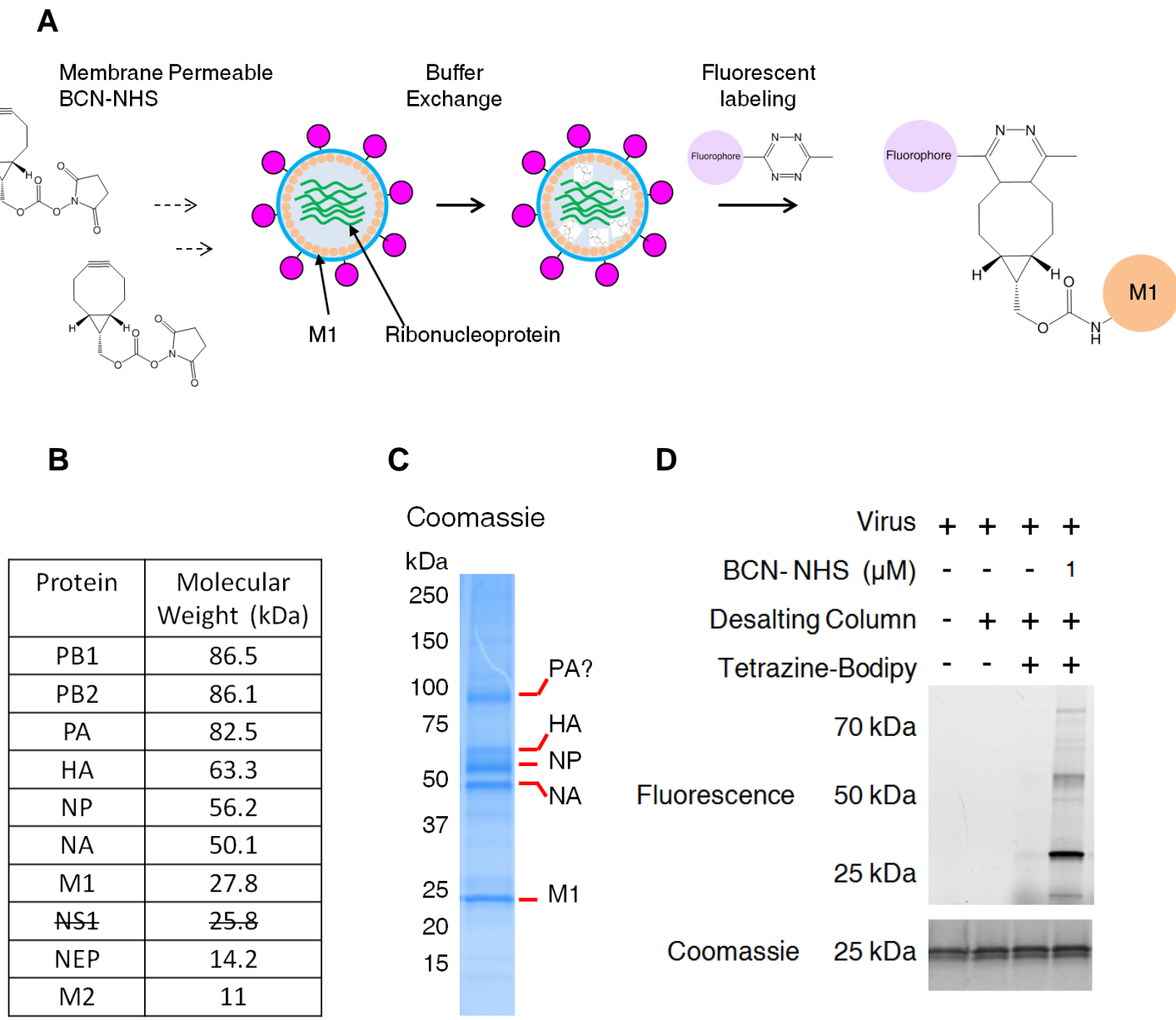


Figure 34. Labeling of IAV with BCN-NHS-Ester enables fluorescent detection of IAV capsid proteins by SDS-PAGE. (A) Membrane permeable BCN-NHS probes can label M1 protein in intact viral particles, and is later labeled with TCO-tagged fluorophores. (B) List of IAV proteins and their corresponding molecular weight. NS1 is not present in the viral capsid. (C) Identification of IAV proteins separated by SDS-PAGE and stained with coomassie blue (D) Labeling of IAV with BCN-NHS-Ester. Virus was diluted 1/4 in pH 9 buffer and labeled for 1 hr at RT before excess BCN was removed by a desalting column, and incubated with 1 mM tetrazine-BODIPY for 15 min. The sample was then separated by SDS-PAGE and imaged with fluorescence gel scanning.

Mimicking Late Endosome Lipid Composition.


Due to the relatively small size of IFITM3, its unknown mechanism, and broad-spectrum anti-viral activity (Table 1), it is believed IFITM3 inhibits viral fusion by the alteration of the fusion environment, in particular the biophysical/mechanical properties of the endosomal membrane. Therefore, the impact of lipid composition choices in our fusion model must be considered, regardless if done via bulk fusion or supported lipid bilayer. While nearly all membranes are comprised of approximately 70% phosphatidylcholine, the remaining lipid composition of lipid species and cholesterol varies significantly by organelle¹⁰⁴. In the literature of bulk liposome fusion assays, a large fraction of the work is focused on protein-catalyzed membrane fusion with LUVs mimicking the plasma membrane¹²¹ and synaptic vesicles¹²². For late endosome lipid composition, there is a paucity of information, the most detailed analysis currently available having been determined with hamster kidney cells¹²³ (Fig. 35). And while our understanding of cholesterol trafficking is making strides the field has only a qualitative understanding that little cholesterol is retained within the limiting membrane during endosome maturation^{40,124}. Nonetheless, to better emulate late endosome lipid composition. Our future work will transition away from the literature used ratios of 80% PC, 20% Chol¹⁰³. To simplify the complexity of the late endosome, a 3 component membrane will be used that accounts for main sources of charged lipids, and steric interactions (Fig. 35B).

A

Lipid	³² p	¹⁴ C
Phosphatidylcholine	48.1	50.6
Phosphatidylethanolamine	19.7	12.4
Sphingomyelin	9.2	5.6
Phosphatidylserine	2.4	5.1
Cardiolipin	0	0.1
Phosphatidylinositol	4.1	8.6
Lysobisphosphatidic acid	15.7	14.8

B

Shape



↓

Lipid	Percent total (molar)
Phosphatidylcholine	80
Phosphatidylethanolamine	20
Phosphatidylserine	5

Charge

0

0

-1

Figure 35. Lipid composition of the late endosome, and proposed mimic.

(A) Kobayashi et al.¹²³, isolated late endosomes from baby hamster kidney (BHK) cells and determined their composition by TLC and autoradiography. (B) To emulate the late endosome environment, and reduce the complexity from 7 to 3 different lipids, we propose using PC, PE, and PS to mimic contributing factors of shape and charge.

Single particle and supported bilayer:

The analysis of viral fusion through bulk assays provides a straightforward approach to understanding the change in the average total fluorescent signal. But even should we be able to successfully detect the occurrence of content mixing as described earlier in the chapter, limitations to the model obscure critical information, such as what fraction undergoes hemifusion and what fraction complete fusion? Are there changes in the fusion rates? In the fusion pore size? Furthermore, the smaller size of LUV (80 nm diameter) results in a surface area of significantly higher membrane curvature in comparison to that encountered in late endosomes (with a diameter in the range of 300 – 800 nm¹²⁵).

To better characterize the fusion event, we intend to conduct single particle measurements on a supported lipid bilayer, using total internal reflection fluorescence (TIRF) microscopy¹²⁶. This model utilizes a single, planer lipid-bilayer assembled from preformed liposomes, and can be supported by a PEG^{127,128} or dextran¹²⁹ cushion, enabling lipid mobility and space for protein activity. The use of TIRF, with a depth of field of 60-200 nm¹²⁶ excludes background signal of viral particles not present at the lipid membrane, enabling single particle resolution. This technique has been used extensively to investigate vesicle¹³⁰, and viral fusion¹³¹, and has can resolve the spatial and temporal progression of single fusion events^{132,133}, providing crucial information as to the dynamics of lipid mixing, and fusion pore formation (Fig 36).

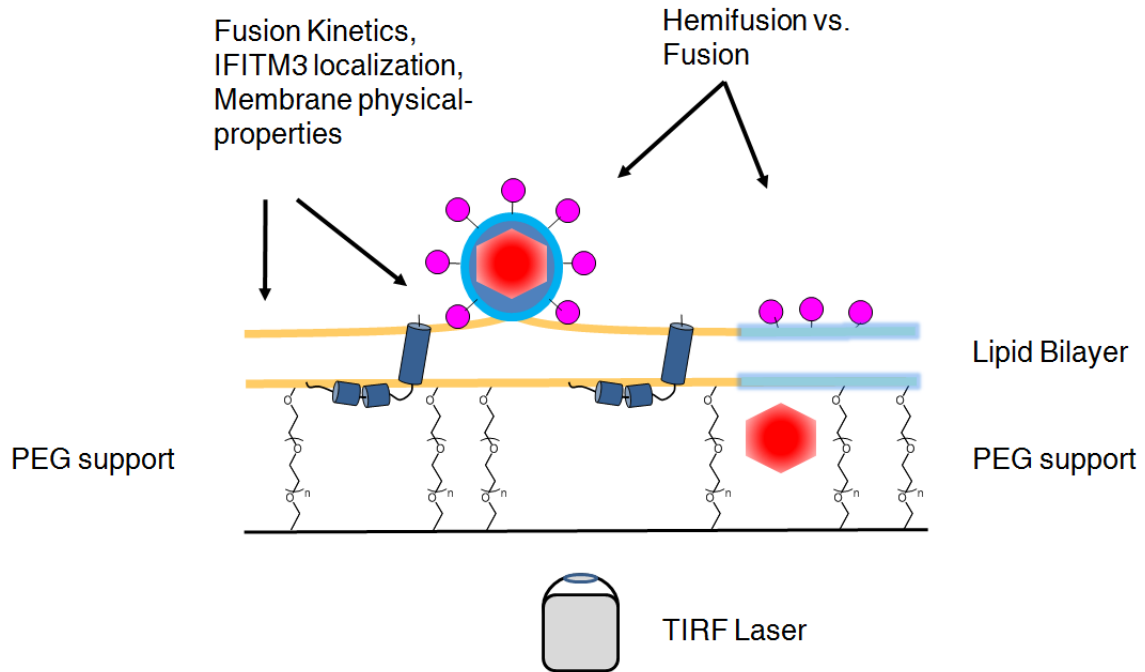


Figure 36. Single particle measurements for improved characterization of viral fusion. Supported lipid bilayers can provide a useful tool for investigating IFITM3 restriction of viral fusion, distinguishing between hemifusion and fusion, as well as measuring other parameters such as fusion kinetics, IFITM3 colocalization (with proper labeling), and membrane fluidity.

Discussion:

Extensive research conducted over the past nine years provides considerable support to the idea that IFITM3, as well as other members of the IFITM family, plays a significant role in the first line of defense against most clinically relevant viral pathogens encountered in the past century. Despite several reports of inflammatory regulation^{20,42}, the literature indicates that the point of interference occurs prior to viral fusion and content delivery^{27,38,134,135}.

As such IFITM3 receives a unique classification: it is part of a group of innate immunity mechanisms that occurs prior to a viruses' ability to introduce their varied methods of virulence or immune evasion¹³⁶. This distinction increases the importance of elucidating its mechanism, in particular due to emerging evidence for mutations in human and avian IAV that can bypass IFITM3 inhibition^{18,137}, as well as recent reports that both IFITM2 and IFITM3 play an role in inhibiting HIV infection^{30,31} (Fig. 37).

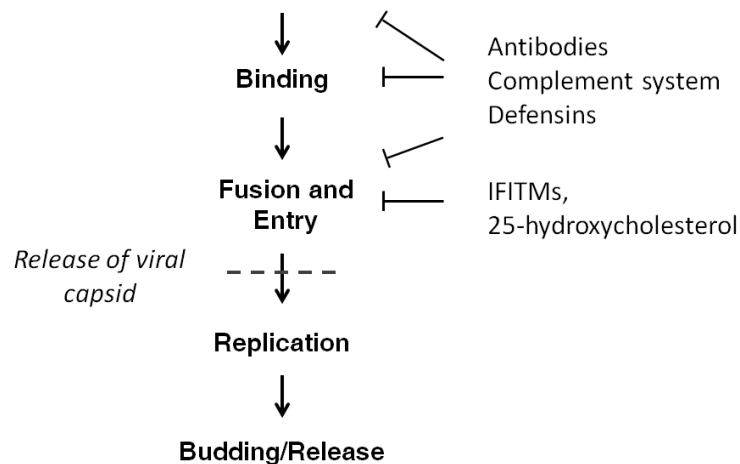


Figure 37. IFITMs' interference with viral fusion and entry is a unique antiviral mechanism. IFITMs belong to a small group of innate immunity proteins that disrupt infection prior to entry and the release of viral evasion mechanisms, such as antibodies¹³⁸, complement system proteins¹³⁹, and defensins¹⁴⁰. Even more uncommon is its inhibition at the point of fusion, which we understand to be the only known protein to directly do so. Viral entry is also inhibited by the upregulation of 25-hydroxycholesterol¹⁴¹.

Earlier work has provided first indicators of possible antiviral mechanisms, with no definitive results^{27,34,39}. The complexity of the cellular environment prompted us to approach the question through the use of a recombinant fusion model. We asked whether we could recapitulate the inhibition of viral fusion in a model system containing a lipid bilayer with IFITM3. This model system would provide first evidence that perhaps one of the mechanisms of IFITM3 is by a direct interaction with the fusion environment.

These efforts were enhanced by our development of the mass-shift based Acyl Peg Exchange (APE) assay, that enables the simultaneous detection of multiple S-fatty acylation levels of endogenous proteins⁷¹. This method addresses a significant limitation to the field of S-fatty acylation, which until now could only assess total changes in protein S-fatty acylation, and could not validate the existence the simultaneous S-fatty acylation events. APE makes it possible to detect physiological S-fatty acylation levels, as well as compare different tissues, time points, inflammatory conditions etc. The analysis of endogenous IFITM3 by APE provided several key findings critical to our future work with recombinant IFITM3; both mouse and human endogenous IFITM3 showed no detectable levels of non-modified (apo) protein (Fig. 16,17), indicating that all IFITM3 is S-acylated at least once. Furthermore, mouse and human cell lines showed differing S-fatty acylation levels. While mIFITM3 appeared to have equal levels of all three S-acylation states, hIFITM3 exhibited only two, with the majority of the protein being dually-S-acylated (Fig. 17).

Our improved understanding of IFITM3 S-acylation proved critical in generating recombinant protein, and emulating specific S-acylation states by mal-palm labeling (Fig. 20). Our purification protocol enables the generation of several mg of protein, does

not introduce denaturing conditions during enrichment^{17,142}, is purified from widely accessible bacterial culture, and contains confirmed, non-reversible covalent modifications mimicking S-fatty acylation.

Finally, the successful preparation and characterization of IFITM3 proteoliposomes paved the way for our first steps towards measuring IFITM3 impact on the viral fusion. Our observation that in the presence of IFITM3, DiD dequenching is impaired suggests an IFITM3 mediated decrease in efficiency of viral hemifusion/fusion. This provides first, preliminary evidence is that IFITM3 can independently exert its anti-viral activity, and that the mechanism is either by interacting with the virus directly or through altering the membrane environment. Broad antiviral activity, and reports in the literature that hemagglutinin mediated cell-cell fusion can be inhibited by IFITM3^{26,34} provides further support in favor of an alteration to the membrane environs.

With respect to the specific effect IFITM3 is exerting on the membrane environs, we have yet to apply the necessary assays capable of testing current hypotheses. It is possible IFITM3 alters the physical properties of the membrane, such as membrane fluidity, rigidity, or lipid spatial distribution. Alternatively, IFITM3 might directly exert a steric/entropic inhibition at the site of fusion itself, either in the form of the hemifused stalk, diaphragm¹⁴³.

We believe our results justify further work, though the bulk fusion model has several limitations that would be overcome by an improved experimental setup. Future experiments will explore single particle tracking - a model that can better mimic the lipid curvature and composition of the physiological viral-fusion environment, as well as work to detect content mixing and IFITM3 organization around the fusion locus.

We believe this data is a promising first step towards understanding the mechanism of IFITM3. The use of a recombinant system holds promise as a tool that can rigorously control and monitor the various parameters that will enable us to elucidate the molecular basis of IFITM3 inhibition in the membrane environment. Combining this with future structural and *in vitro* assays, we look forward to expanding our knowledge of this critical protein.

References:

- 1 Mogensen, T. H. Pathogen recognition and inflammatory signaling in innate immune defenses. *Clin Microbiol Rev* **22**, 240-273, Table of Contents, doi:10.1128/CMR.00046-08 (2009).
- 2 Newton, K. & Dixit, V. M. Signaling in innate immunity and inflammation. *Cold Spring Harb Perspect Biol* **4**, doi:10.1101/cshperspect.a006049 (2012).
- 3 Iwasaki, A. & Medzhitov, R. Control of adaptive immunity by the innate immune system. *Nature immunology* **16**, 343-353, doi:10.1038/ni.3123 (2015).
- 4 McNab, F., Mayer-Barber, K., Sher, A., Wack, A. & O'Garra, A. Type I interferons in infectious disease. *Nat Rev Immunol* **15**, 87-103, doi:10.1038/nri3787 (2015).
- 5 Raftery, N. & Stevenson, N. J. Advances in anti-viral immune defence: revealing the importance of the IFN JAK/STAT pathway. *Cell Mol Life Sci* **74**, 2525-2535, doi:10.1007/s00018-017-2520-2 (2017).
- 6 Green, D. S., Young, H. A. & Valencia, J. C. Current prospects of type II interferon gamma signaling and autoimmunity. *The Journal of biological chemistry* **292**, 13925-13933, doi:10.1074/jbc.R116.774745 (2017).
- 7 Kotenko, S. V. & Durbin, J. E. Contribution of type III interferons to antiviral immunity: location, location, location. *The Journal of biological chemistry* **292**, 7295-7303, doi:10.1074/jbc.R117.777102 (2017).
- 8 Brass, A. L. *et al.* The IFITM proteins mediate cellular resistance to influenza A H1N1 virus, West Nile virus, and dengue virus. *Cell* **139**, 1243-1254, doi:10.1016/j.cell.2009.12.017 (2009).
- 9 Smith, S., Weston, S., Kellam, P. & Marsh, M. IFITM proteins-cellular inhibitors of viral entry. *Curr Opin Virol* **4**, 71-77, doi:10.1016/j.coviro.2013.11.004 (2014).
- 10 John, S. P. *et al.* The CD225 domain of IFITM3 is required for both IFITM protein association and inhibition of influenza A virus and dengue virus replication. *Journal of virology* **87**, 7837-7852, doi:10.1128/JVI.00481-13 (2013).
- 11 Zhang, Z., Liu, J., Li, M., Yang, H. & Zhang, C. Evolutionary dynamics of the interferon-induced transmembrane gene family in vertebrates. *PloS one* **7**, e49265, doi:10.1371/journal.pone.0049265 (2012).
- 12 Compton, A. A. *et al.* Natural mutations in IFITM3 modulate post-translational regulation and toggle antiviral specificity. *EMBO Rep* **17**, 1657-1671, doi:10.15252/embr.201642771 (2016).
- 13 Yount, J. S., Karssemeijer, R. A. & Hang, H. C. S-palmitoylation and ubiquitination differentially regulate interferon-induced transmembrane protein 3 (IFITM3)-mediated resistance to influenza virus. *The Journal of biological chemistry* **287**, 19631-19641, doi:10.1074/jbc.M112.362095 (2012).
- 14 Jia, R. *et al.* Identification of an endocytic signal essential for the antiviral action of IFITM3. *Cell Microbiol* **16**, 1080-1093, doi:10.1111/cmi.12262 (2014).
- 15 Yount, J. S. *et al.* Palmitoylome profiling reveals S-palmitoylation-dependent antiviral activity of IFITM3. *Nature chemical biology* **6**, 610-614, doi:10.1038/nchembio.405 (2010).
- 16 Bailey, C. C., Kondur, H. R., Huang, I. C. & Farzan, M. Interferon-induced transmembrane protein 3 is a type II transmembrane protein. *The Journal of biological chemistry* **288**, 32184-32193, doi:10.1074/jbc.M113.514356 (2013).
- 17 Ling, S. *et al.* Combined approaches of EPR and NMR illustrate only one transmembrane helix in the human IFITM3. *Sci Rep* **6**, 24029, doi:10.1038/srep24029 (2016).

- 18 Sun, X. *et al.* Constitutively Expressed IFITM3 Protein in Human Endothelial Cells Poses an Early Infection Block to Human Influenza Viruses. *Journal of virology* **90**, 11157-11167, doi:10.1128/JVI.01254-16 (2016).
- 19 Narayana, S. K. *et al.* The Interferon-induced Transmembrane Proteins, IFITM1, IFITM2, and IFITM3 Inhibit Hepatitis C Virus Entry. *The Journal of biological chemistry* **290**, 25946-25959, doi:10.1074/jbc.M115.657346 (2015).
- 20 Stacey, M. A. *et al.* The antiviral restriction factor IFN-induced transmembrane protein 3 prevents cytokine-driven CMV pathogenesis. *J Clin Invest* **127**, 1463-1474, doi:10.1172/JCI84889 (2017).
- 21 Gorman, M. J., Poddar, S., Farzan, M. & Diamond, M. S. The Interferon-Stimulated Gene Ifitm3 Restricts West Nile Virus Infection and Pathogenesis. *Journal of virology* **90**, 8212-8225, doi:10.1128/JVI.00581-16 (2016).
- 22 Infusini, G. *et al.* Respiratory DC Use IFITM3 to Avoid Direct Viral Infection and Safeguard Virus-Specific CD8+ T Cell Priming. *PloS one* **10**, e0143539, doi:10.1371/journal.pone.0143539 (2015).
- 23 Wakim, L. M., Gupta, N., Mintern, J. D. & Villadangos, J. A. Enhanced survival of lung tissue-resident memory CD8(+) T cells during infection with influenza virus due to selective expression of IFITM3. *Nature immunology* **14**, 238-245, doi:10.1038/ni.2525 (2013).
- 24 Savidis, G. *et al.* The IFITMs Inhibit Zika Virus Replication. *Cell reports* **15**, 2323-2330, doi:10.1016/j.celrep.2016.05.074 (2016).
- 25 Wilkins, C. *et al.* IFITM1 is a tight junction protein that inhibits hepatitis C virus entry. *Hepatology* **57**, 461-469, doi:10.1002/hep.26066 (2013).
- 26 Chesarino, N. M. *et al.* IFITM3 requires an amphipathic helix for antiviral activity. *EMBO Rep*, doi:10.15252/embr.201744100 (2017).
- 27 Desai, T. M. *et al.* IFITM3 restricts influenza A virus entry by blocking the formation of fusion pores following virus-endosome hemifusion. *PLoS pathogens* **10**, e1004048, doi:10.1371/journal.ppat.1004048 (2014).
- 28 Huang, I. C. *et al.* Distinct patterns of IFITM-mediated restriction of filoviruses, SARS coronavirus, and influenza A virus. *PLoS pathogens* **7**, e1001258, doi:10.1371/journal.ppat.1001258 (2011).
- 29 Zhao, X. *et al.* Interferon induction of IFITM proteins promotes infection by human coronavirus OC43. *Proceedings of the National Academy of Sciences of the United States of America* **111**, 6756-6761, doi:10.1073/pnas.1320856111 (2014).
- 30 Wu, W. L. *et al.* Delta20 IFITM2 differentially restricts X4 and R5 HIV-1. *Proceedings of the National Academy of Sciences of the United States of America* **114**, 7112-7117, doi:10.1073/pnas.1619640114 (2017).
- 31 Foster, T. L. *et al.* Resistance of Transmitted Founder HIV-1 to IFITM-Mediated Restriction. *Cell host & microbe* **20**, 429-442, doi:10.1016/j.chom.2016.08.006 (2016).
- 32 Compton, A. A. *et al.* IFITM proteins incorporated into HIV-1 virions impair viral fusion and spread. *Cell host & microbe* **16**, 736-747, doi:10.1016/j.chom.2014.11.001 (2014).
- 33 Lu, J. *et al.* The IFITM proteins inhibit HIV-1 infection. *Journal of virology* **85**, 2126-2137, doi:10.1128/JVI.01531-10 (2011).
- 34 Li, K. *et al.* IFITM proteins restrict viral membrane hemifusion. *PLoS pathogens* **9**, e1003124, doi:10.1371/journal.ppat.1003124 (2013).
- 35 Diamond, M. S. & Farzan, M. The broad-spectrum antiviral functions of IFIT and IFITM proteins. *Nat Rev Immunol* **13**, 46-57, doi:10.1038/nri3344 (2013).
- 36 Mudhasani, R. *et al.* IFITM-2 and IFITM-3 but not IFITM-1 restrict Rift Valley fever virus. *Journal of virology* **87**, 8451-8464, doi:10.1128/JVI.03382-12 (2013).

- 37 Anafu, A. A., Bowen, C. H., Chin, C. R., Brass, A. L. & Holm, G. H. Interferon-inducible transmembrane protein 3 (IFITM3) restricts reovirus cell entry. *The Journal of biological chemistry* **288**, 17261-17271, doi:10.1074/jbc.M112.438515 (2013).
- 38 Feeley, E. M. *et al.* IFITM3 inhibits influenza A virus infection by preventing cytosolic entry. *PLoS pathogens* **7**, e1002337, doi:10.1371/journal.ppat.1002337 (2011).
- 39 Amini-Bavil-Olyaei, S. *et al.* The antiviral effector IFITM3 disrupts intracellular cholesterol homeostasis to block viral entry. *Cell host & microbe* **13**, 452-464, doi:10.1016/j.chom.2013.03.006 (2013).
- 40 Zhao, K. & Ridgway, N. D. Oxysterol-Binding Protein-Related Protein 1L Regulates Cholesterol Egress from the Endo-Lysosomal System. *Cell reports* **19**, 1807-1818, doi:10.1016/j.celrep.2017.05.028 (2017).
- 41 Tartour, K. *et al.* Interference with the production of infectious viral particles and bimodal inhibition of replication are broadly conserved antiviral properties of IFITMs. *PLoS pathogens* **13**, e1006610, doi:10.1371/journal.ppat.1006610 (2017).
- 42 Jiang, L. Q. *et al.* IFITM3 inhibits virus-triggered induction of type I interferon by mediating autophagosome-dependent degradation of IRF3. *Cell Mol Immunol*, doi:10.1038/cmi.2017.15 (2017).
- 43 Jia, R. *et al.* The N-terminal region of IFITM3 modulates its antiviral activity by regulating IFITM3 cellular localization. *Journal of virology* **86**, 13697-13707, doi:10.1128/JVI.01828-12 (2012).
- 44 Chesarino, N. M., McMichael, T. M., Hach, J. C. & Yount, J. S. Phosphorylation of the antiviral protein interferon-inducible transmembrane protein 3 (IFITM3) dually regulates its endocytosis and ubiquitination. *The Journal of biological chemistry* **289**, 11986-11992, doi:10.1074/jbc.M114.557694 (2014).
- 45 Shan, Z. *et al.* Negative regulation of interferon-induced transmembrane protein 3 by SET7-mediated lysine monomethylation. *The Journal of biological chemistry* **288**, 35093-35103, doi:10.1074/jbc.M113.511949 (2013).
- 46 Resh, M. D. Targeting protein lipidation in disease. *Trends Mol Med* **18**, 206-214, doi:10.1016/j.molmed.2012.01.007 (2012).
- 47 Chamberlain, L. H. & Shipston, M. J. The physiology of protein S-acylation. *Physiol Rev* **95**, 341-376, doi:10.1152/physrev.00032.2014 (2015).
- 48 Laszlo Muszbek, G. H., Joanne E. Cluette-Brown, Elizabeth M. Van Cott, and Michael Laposata. The Pool of Fatty Acids Covalently Bound to Platelet Proteins by Thioester Linkages Can Be Altered by Exogenously Supplied Fatty Acids. *Lipids* **34**, S331-337 (1999).
- 49 Gottlieb, C. D. & Linder, M. E. Structure and function of DHHC protein S-acyltransferases. *Biochemical Society transactions* **45**, 923-928, doi:10.1042/BST20160304 (2017).
- 50 Hirano, T. *et al.* Thioesterase activity and subcellular localization of acylprotein thioesterase 1/lysophospholipase 1. *Biochimica et biophysica acta* **1791**, 797-805, doi:10.1016/j.bbailip.2009.05.001 (2009).
- 51 Haltia, J. S. J. T. M. M. Palmitoyl-protein thioesterase, an enzyme implicated in neurodegeneration, is localized in neurons and is developmentally regulated in rat brain. *Neuroscience Letters* **265**, 53-56 (1999).
- 52 Lin, D. T. & Conibear, E. ABHD17 proteins are novel protein depalmitoylases that regulate N-Ras palmitate turnover and subcellular localization. *Elife* **4**, e11306, doi:10.7554/eLife.11306 (2015).
- 53 Pott, J. & Stockinger, S. Type I and III Interferon in the Gut: Tight Balance between Host Protection and Immunopathology. *Front Immunol* **8**, 258, doi:10.3389/fimmu.2017.00258 (2017).

- 54 Makris, S., Paulsen, M. & Johansson, C. Type I Interferons as Regulators of Lung Inflammation. *Front Immunol* **8**, 259, doi:10.3389/fimmu.2017.00259 (2017).
- 55 Teng, Y. B. *et al.* Efficient demyristoylase activity of SIRT2 revealed by kinetic and structural studies. *Sci Rep* **5**, 8529, doi:10.1038/srep08529 (2015).
- 56 Lanyon-Hogg, T., Faronato, M., Serwa, R. A. & Tate, E. W. Dynamic Protein Acylation: New Substrates, Mechanisms, and Drug Targets. *Trends Biochem Sci* **42**, 566-581, doi:10.1016/j.tibs.2017.04.004 (2017).
- 57 Charron, G. *et al.* Robust fluorescent detection of protein fatty-acylation with chemical reporters. *Journal of the American Chemical Society* **131**, 4967-4975, doi:10.1021/ja810122f (2009).
- 58 Hang, H. C., Wilson, J. P. & Charron, G. Bioorthogonal chemical reporters for analyzing protein lipidation and lipid trafficking. *Acc Chem Res* **44**, 699-708, doi:10.1021/ar200063v (2011).
- 59 Thinon, E., Percher, A. & Hang, H. C. Bioorthogonal Chemical Reporters for Monitoring Unsaturated Fatty-Acylated Proteins. *Chembiochem* **17**, 1800-1803, doi:10.1002/cbic.201600213 (2016).
- 60 Wan, J., Roth, A. F., Bailey, A. O. & Davis, N. G. Palmitoylated proteins: purification and identification. *Nature protocols* **2**, 1573-1584, doi:10.1038/nprot.2007.225 (2007).
- 61 Forrester, M. T. *et al.* Site-specific analysis of protein S-acylation by resin-assisted capture. *Journal of lipid research* **52**, 393-398, doi:10.1194/jlr.D011106 (2011).
- 62 Percher, A., Thinon, E. & Hang, H. Mass-Tag Labeling Using Acyl-PEG Exchange for the Determination of Endogenous Protein S-Fatty Acylation. *Curr Protoc Protein Sci* **89**, 14 17 11-14 17 11, doi:10.1002/cpps.36 (2017).
- 63 Chesarino, N. M. *et al.* Chemoproteomics reveals Toll-like receptor fatty acylation. *BMC Biol* **12**, 91, doi:10.1186/s12915-014-0091-3 (2014).
- 64 Caballero, M. C. *et al.* Identification of new palmitoylated proteins in *Toxoplasma gondii*. *Biochimica et biophysica acta* **1864**, 400-408, doi:10.1016/j.bbapap.2016.01.010 (2016).
- 65 Ivaldi, C. *et al.* Proteomic analysis of S-acylated proteins in human B cells reveals palmitoylation of the immune regulators CD20 and CD23. *PloS one* **7**, e37187, doi:10.1371/journal.pone.0037187 (2012).
- 66 Morrison, E. *et al.* Quantitative analysis of the human T cell palmitome. *Sci Rep* **5**, 11598, doi:10.1038/srep11598 (2015).
- 67 Kang, R. *et al.* Neural palmitoyl-proteomics reveals dynamic synaptic palmitoylation. *Nature* **456**, 904-909, doi:10.1038/nature07605 (2008).
- 68 Srivastava, V., Weber, J. R., Malm, E., Fouke, B. W. & Bulone, V. Proteomic Analysis of a Poplar Cell Suspension Culture Suggests a Major Role of Protein S-Acylation in Diverse Cellular Processes. *Front Plant Sci* **7**, 477, doi:10.3389/fpls.2016.00477 (2016).
- 69 Antinone, S. E., Ghadge, G. D., Ostrow, L. W., Roos, R. P. & Green, W. N. S-acylation of SOD1, CCS, and a stable SOD1-CCS heterodimer in human spinal cords from ALS and non-ALS subjects. *Sci Rep* **7**, 41141, doi:10.1038/srep41141 (2017).
- 70 Collins, M. O., Woodley, K. T. & Choudhary, J. S. Global, site-specific analysis of neuronal protein S-acylation. *Sci Rep* **7**, 4683, doi:10.1038/s41598-017-04580-1 (2017).
- 71 Percher, A. *et al.* Mass-tag labeling reveals site-specific and endogenous levels of protein S-fatty acylation. *Proceedings of the National Academy of Sciences of the United States of America* **113**, 4302-4307, doi:10.1073/pnas.1602244113 (2016).
- 72 Rocks, O. *et al.* An acylation cycle regulates localization and activity of palmitoylated Ras isoforms. *Science* **307**, 1746-1752, doi:10.1126/science.1105654 (2005).
- 73 Lakkaraju, A. K. *et al.* Palmitoylated calnexin is a key component of the ribosome-translocon complex. *The EMBO journal* **31**, 1823-1835, doi:10.1038/emboj.2012.15 (2012).

- 74 Sharma, C., Yang, X. H. & Hemler, M. E. DHHC2 affects palmitoylation, stability, and functions of tetraspanins CD9 and CD151. *Mol Biol Cell* **19**, 3415-3425, doi:10.1091/mbc.E07-11-1164 (2008).
- 75 Everitt, A. R. *et al.* IFITM3 restricts the morbidity and mortality associated with influenza. *Nature* **484**, 519-523, doi:10.1038/nature10921 (2012).
- 76 Mao, P. *et al.* Human alveolar epithelial type II cells in primary culture. *Physiol Rep* **3**, doi:10.14814/phy2.12288 (2015).
- 77 Malakhov, M. P. *et al.* SUMO fusions and SUMO-specific protease for efficient expression and purification of proteins. *J Struct Funct Genomics* **5**, 75-86, doi:10.1023/B:JSFG.0000029237.70316.52 (2004).
- 78 Al, I. Exocytosis and Endocytosis *Methods in molecular biology* (2008).
- 79 Christopher D. Lima, E. M. Rapidly cleavable sumo fusion protein expression system for difficult to express proteins. US patent (2005).
- 80 Andersen, K. R., Leksa, N. C. & Schwartz, T. U. Optimized E. coli expression strain LOBSTR eliminates common contaminants from His-tag purification. *Proteins* **81**, 1857-1861, doi:10.1002/prot.24364 (2013).
- 81 Fenyo, D. *et al.* MALDI sample preparation: the ultra thin layer method. *Journal of visualized experiments : JoVE*, 192, doi:10.3791/192 (2007).
- 82 Seddon, A. M., Curnow, P. & Booth, P. J. Membrane proteins, lipids and detergents: not just a soap opera. *Biochimica et biophysica acta* **1666**, 105-117, doi:10.1016/j.bbamem.2004.04.011 (2004).
- 83 Hullin-Matsuda, F., Taguchi, T., Greimel, P. & Kobayashi, T. Lipid compartmentalization in the endosome system. *Semin Cell Dev Biol* **31**, 48-56, doi:10.1016/j.semcdb.2014.04.010 (2014).
- 84 Gupta, K. *et al.* The role of interfacial lipids in stabilizing membrane protein oligomers. *Nature* **541**, 421-424, doi:10.1038/nature20820 (2017).
- 85 Rigaud JL, L. D. Reconstitution of membrane proteins into liposomes. *Methods in Enzymology* **372**, 65-86, doi:doi.org/10.1016/S0076-6879(03)72004-7 (2003).
- 86 Weber, T. *et al.* SNAREpins: minimal machinery for membrane fusion. *Cell* **92**, 759-772 (1998).
- 87 Snead, D., Wragg, R. T., Dittman, J. S. & Eliezer, D. Membrane curvature sensing by the C-terminal domain of complexin. *Nature communications* **5**, 4955, doi:10.1038/ncomms5955 (2014).
- 88 Dimova, R. *et al.* A practical guide to giant vesicles. Probing the membrane nanoregime via optical microscopy. *J Phys Condens Matter* **18**, S1151-1176, doi:10.1088/0953-8984/18/28/S04 (2006).
- 89 Chen, X. *et al.* SNARE-mediated lipid mixing depends on the physical state of the vesicles. *Biophys J* **90**, 2062-2074, doi:10.1529/biophysj.105.071415 (2006).
- 90 Gui, L., Ebner, J. L., Mileant, A., Williams, J. A. & Lee, K. K. Visualization and Sequencing of Membrane Remodeling Leading to Influenza Virus Fusion. *Journal of virology* **90**, 6948-6962, doi:10.1128/JVI.00240-16 (2016).
- 91 Dimova, R. Recent developments in the field of bending rigidity measurements on membranes. *Adv Colloid Interface Sci* **208**, 225-234, doi:10.1016/j.cis.2014.03.003 (2014).
- 92 M.J. HOPE , M. B. B., L.D. MAYER , A.S. JANOFF and P.R. CULLIS Generation of Multilamellar and Unilamellar Phospholipid Vesicles. *Chemistry and Physics of Lipids* **40**, 89-107, doi:10.1016/0009-3084(86)90065-4 (1986).
- 93 Stetefeld, J., McKenna, S. A. & Patel, T. R. Dynamic light scattering: a practical guide and applications in biomedical sciences. *Biophys Rev* **8**, 409-427, doi:10.1007/s12551-016-0218-6 (2016).

- 94 George Rouser, S. F., Akira Yamamoto. Two Dimensional Thin Layer Chromatographic Separation of Polar Lipids and Determination of Phospholipids by Phosphorus Analysis of Spots. *Lipids* (1969).
- 95 Mima, J. & Wickner, W. Complex lipid requirements for SNARE- and SNARE chaperone-dependent membrane fusion. *The Journal of biological chemistry* **284**, 27114-27122, doi:10.1074/jbc.M109.010223 (2009).
- 96 J. Gallová, D. U., A. Islamov, A. Kuklin and P. Balgavý. Effect of cholesterol on the bilayer thickness in unilamellar extruded DLPC and DOPC liposomes: SANS contrast variation study. *Gen. Physiol. Biophys.* **23**, 263 (2004).
- 97 Kucerka, N., Tristram-Nagle, S. & Nagle, J. F. Structure of fully hydrated fluid phase lipid bilayers with monounsaturated chains. *J Membr Biol* **208**, 193-202, doi:10.1007/s00232-005-7006-8 (2005).
- 98 Mitra, K., Ubarretxena-Belandia, I., Taguchi, T., Warren, G. & Engelman, D. M. Modulation of the bilayer thickness of exocytic pathway membranes by membrane proteins rather than cholesterol. *Proceedings of the National Academy of Sciences of the United States of America* **101**, 4083-4088, doi:10.1073/pnas.0307332101 (2004).
- 99 Andersson, J. & Koper, I. Tethered and Polymer Supported Bilayer Lipid Membranes: Structure and Function. *Membranes (Basel)* **6**, doi:10.3390/membranes6020030 (2016).
- 100 Zaitseva, E., Yang, S. T., Melikov, K., Pourmal, S. & Chernomordik, L. V. Dengue virus ensures its fusion in late endosomes using compartment-specific lipids. *PLoS pathogens* **6**, e1001131, doi:10.1371/journal.ppat.1001131 (2010).
- 101 Lakadamyali, M., Rust, M. J., Babcock, H. P. & Zhuang, X. Visualizing infection of individual influenza viruses. *Proceedings of the National Academy of Sciences of the United States of America* **100**, 9280-9285, doi:10.1073/pnas.0832269100 (2003).
- 102 Hsu, H. L., Millet, J. K., Costello, D. A., Whittaker, G. R. & Daniel, S. Viral fusion efficacy of specific H3N2 influenza virus reassortant combinations at single-particle level. *Sci Rep* **6**, 35537, doi:10.1038/srep35537 (2016).
- 103 Floyd, D. L., Ragains, J. R., Skehel, J. J., Harrison, S. C. & van Oijen, A. M. Single-particle kinetics of influenza virus membrane fusion. *Proceedings of the National Academy of Sciences of the United States of America* **105**, 15382-15387, doi:10.1073/pnas.0807771105 (2008).
- 104 van Meer, G., Voelker, D. R. & Feigenson, G. W. Membrane lipids: where they are and how they behave. *Nature reviews. Molecular cell biology* **9**, 112-124, doi:10.1038/nrm2330 (2008).
- 105 Jahn, R. & Scheller, R. H. SNAREs--engines for membrane fusion. *Nature reviews. Molecular cell biology* **7**, 631-643, doi:10.1038/nrm2002 (2006).
- 106 Li, S. *et al.* pH-Controlled two-step uncoating of influenza virus. *Biophys J* **106**, 1447-1456, doi:10.1016/j.bpj.2014.02.018 (2014).
- 107 Chavela M. Carr, C. C., and Peter S. Kim. Influenza hemagglutinin is spring-loaded by a metastable native conformation. *Proceedings of the National Academy of Sciences of the United States of America* **94** (1997).
- 108 Daleke, D. L., Hong, K. & Papahadjopoulos, D. Endocytosis of liposomes by macrophages: binding, acidification and leakage of liposomes monitored by a new fluorescence assay. *Biochimica et biophysica acta* **1024**, 352-366 (1990).
- 109 Zucchi, P. C. & Zick, M. Membrane fusion catalyzed by a Rab, SNAREs, and SNARE chaperones is accompanied by enhanced permeability to small molecules and by lysis. *Mol Biol Cell* **22**, 4635-4646, doi:10.1091/mbc.E11-08-0680 (2011).
- 110 Diao, J. *et al.* A single vesicle-vesicle fusion assay for in vitro studies of SNAREs and accessory proteins. *Nature protocols* **7**, 921-934 (2012).

- 111 Campbell, E. M., Perez, O., Melar, M. & Hope, T. J. Labeling HIV-1 virions with two fluorescent proteins allows identification of virions that have productively entered the target cell. *Virology* **360**, 286-293, doi:10.1016/j.virol.2006.10.025 (2007).
- 112 Kim, C. H., Axup, J. Y. & Schultz, P. G. Protein conjugation with genetically encoded unnatural amino acids. *Current opinion in chemical biology* **17**, 412-419, doi:10.1016/j.cbpa.2013.04.017 (2013).
- 113 Yang, Y. *et al.* Genetically encoded releasable photo-cross-linking strategies for studying protein-protein interactions in living cells. *Nature protocols* **12**, 2147-2168, doi:10.1038/nprot.2017.090 (2017).
- 114 Peng, T. & Hang, H. C. Bifunctional fatty acid chemical reporter for analyzing S-palmitoylated membrane protein-protein interactions in mammalian cells. *Journal of the American Chemical Society* **137**, 556-559, doi:10.1021/ja502109n (2015).
- 115 Peng, T. & Hang, H. C. Site-Specific Bioorthogonal Labeling for Fluorescence Imaging of Intracellular Proteins in Living Cells. *Journal of the American Chemical Society* **138**, 14423-14433, doi:10.1021/jacs.6b08733 (2016).
- 116 Kelemen, R. E. *et al.* A Precise Chemical Strategy To Alter the Receptor Specificity of the Adeno-Associated Virus. *Angewandte Chemie* **55**, 10645-10649, doi:10.1002/anie.201604067 (2016).
- 117 Carrico, Z. M., Romanini, D. W., Mehl, R. A. & Francis, M. B. Oxidative coupling of peptides to a virus capsid containing unnatural amino acids. *Chemical communications*, 1205-1207, doi:10.1039/b717826c (2008).
- 118 Yu, X. *et al.* Probing of CD4 binding pocket of HIV-1 gp120 glycoprotein using unnatural phenylalanine analogues. *Bioorg Med Chem Lett* **24**, 5699-5703, doi:10.1016/j.bmcl.2014.10.058 (2014).
- 119 Lang, K. *et al.* Genetic Encoding of bicyclononynes and trans-cyclooctenes for site-specific protein labeling in vitro and in live mammalian cells via rapid fluorogenic Diels-Alder reactions. *Journal of the American Chemical Society* **134**, 10317-10320, doi:10.1021/ja302832g (2012).
- 120 Nanda, J. S. & Lorsch, J. R. Labeling a protein with fluorophores using NHS ester derivitization. *Methods Enzymol* **536**, 87-94, doi:10.1016/B978-0-12-420070-8.00008-8 (2014).
- 121 Breckenridge, W. C., Gombos, G. & Morgan, I. G. The lipid composition of adult rat brain synaptosomal plasma membranes. *Biochimica et biophysica acta* **266**, 695-707 (1972).
- 122 Breckenridge, W. C., Morgan, I. G., Zanetta, J. P. & Vincendon, G. Adult rat brain synaptic vesicles. II. Lipid composition. *Biochimica et biophysica acta* **320**, 681-686 (1973).
- 123 Kobayashi, T. *et al.* Separation and characterization of late endosomal membrane domains. *The Journal of biological chemistry* **277**, 32157-32164, doi:10.1074/jbc.M202838200 (2002).
- 124 Mobius, W. *et al.* Recycling compartments and the internal vesicles of multivesicular bodies harbor most of the cholesterol found in the endocytic pathway. *Traffic* **4**, 222-231 (2003).
- 125 Sobo, K. *et al.* Late endosomal cholesterol accumulation leads to impaired intra-endosomal trafficking. *PloS one* **2**, e851, doi:10.1371/journal.pone.0000851 (2007).
- 126 Martin-Fernandez, M. L., Tynan, C. J. & Webb, S. E. A 'pocket guide' to total internal reflection fluorescence. *J Microsc* **252**, 16-22, doi:10.1111/jmi.12070 (2013).
- 127 Karatekin, E. & Rothman, J. E. Fusion of single proteoliposomes with planar, cushioned bilayers in microfluidic flow cells. *Nature protocols* **7**, 903-920, doi:10.1038/nprot.2012.019 (2012).

- 128 Diaz, A. J., Albertorio, F., Daniel, S. & Cremer, P. S. Double cushions preserve transmembrane protein mobility in supported bilayer systems. *Langmuir* **24**, 6820-6826, doi:10.1021/la800018d (2008).
- 129 Elender, G., Kuhner, M. & Sackmann, E. Functionalisation of Si/SiO₂ and glass surfaces with ultrathin dextran films and deposition of lipid bilayers. *Biosens Bioelectron* **11**, 565-577 (1996).
- 130 Fix, M. *et al.* Imaging single membrane fusion events mediated by SNARE proteins. *Proceedings of the National Academy of Sciences of the United States of America* **101**, 7311-7316, doi:10.1073/pnas.0401779101 (2004).
- 131 Costello, D. A., Millet, J. K., Hsia, C. Y., Whittaker, G. R. & Daniel, S. Single particle assay of coronavirus membrane fusion with proteinaceous receptor-embedded supported bilayers. *Biomaterials* **34**, 7895-7904, doi:10.1016/j.biomaterials.2013.06.034 (2013).
- 132 Floyd, D. L., Harrison, S. C. & van Oijen, A. M. Method for measurement of viral fusion kinetics at the single particle level. *Journal of visualized experiments : JoVE*, doi:10.3791/1484 (2009).
- 133 Kim, I. S. *et al.* Mechanism of membrane fusion induced by vesicular stomatitis virus G protein. *Proceedings of the National Academy of Sciences of the United States of America* **114**, E28-E36, doi:10.1073/pnas.1618883114 (2017).
- 134 Weston, S. *et al.* Alphavirus Restriction by IFITM Proteins. *Traffic* **17**, 997-1013, doi:10.1111/tra.12416 (2016).
- 135 Desai, T. M., Marin, M., Mason, C. & Melikyan, G. B. pH regulation in early endosomes and interferon-inducible transmembrane proteins control avian retrovirus fusion. *The Journal of biological chemistry* **292**, 7817-7827, doi:10.1074/jbc.M117.783878 (2017).
- 136 Schulz, K. S. & Mossman, K. L. Viral Evasion Strategies in Type I IFN Signaling - A Summary of Recent Developments. *Front Immunol* **7**, 498, doi:10.3389/fimmu.2016.00498 (2016).
- 137 Gerlach, T. *et al.* pH Optimum of Hemagglutinin-Mediated Membrane Fusion Determines Sensitivity of Influenza A Viruses to the Interferon-Induced Antiviral State and IFITMs. *Journal of virology* **91**, doi:10.1128/JVI.00246-17 (2017).
- 138 Crowe, J. E., Jr. Principles of Broad and Potent Antiviral Human Antibodies: Insights for Vaccine Design. *Cell host & microbe* **22**, 193-206, doi:10.1016/j.chom.2017.07.013 (2017).
- 139 Agrawal, P., Nawadkar, R., Ojha, H., Kumar, J. & Sahu, A. Complement Evasion Strategies of Viruses: An Overview. *Front Microbiol* **8**, 1117, doi:10.3389/fmicb.2017.01117 (2017).
- 140 Holly, M. K., Diaz, K. & Smith, J. G. Defensins in Viral Infection and Pathogenesis. *Annu Rev Virol* **4**, 369-391, doi:10.1146/annurev-virology-101416-041734 (2017).
- 141 Liu, S. Y. *et al.* Interferon-inducible cholesterol-25-hydroxylase broadly inhibits viral entry by production of 25-hydroxycholesterol. *Immunity* **38**, 92-105, doi:10.1016/j.immuni.2012.11.005 (2013).
- 142 Harmand, T. J., Pattabiraman, V. R. & Bode, J. W. Chemical Synthesis of the Highly Hydrophobic Antiviral Membrane-Associated Protein IFITM3 and Modified Variants. *Angewandte Chemie* **56**, 12639-12643, doi:10.1002/anie.201707554 (2017).
- 143 Chernomordik, L. V. & Kozlov, M. M. Mechanics of membrane fusion. *Nat Struct Mol Biol* **15**, 675-683, doi:10.1038/nsmb.1455 (2008).